

M. Phys. Sergey Maltsev

**Structural elucidation  
of nanocrystalline biomaterials**

Die vorliegende Arbeit entstand an der Bundesanstalt für Materialforschung und -prüfung (BAM).

Impressum

**Structural elucidation  
of nanocrystalline biomaterials**

2008

Herausgeber:

Bundesanstalt für Materialforschung und -prüfung (BAM)

Unter den Eichen 87

12205 Berlin

Telefon: +49 30 8104-0

Telefax: +49 30 8112029

E-Mail: [info@bam.de](mailto:info@bam.de)

Internet: [www.bam.de](http://www.bam.de)

Copyright © 2008 by Bundesanstalt für  
Materialforschung und -prüfung (BAM)

Layout: BAM-Arbeitsgruppe Z.64

ISSN 1613-4249

ISBN 978-3-9812072-4-8

# Structural elucidation of nanocrystalline biomaterials

Von der Fakultät für Physik und Geowissenschaften

der Universität Leipzig

genehmigte

DISSERTATION

zur Erlangung des akademischen Grades

doctor rerum naturalium

(Dr. rer. nat.)

vorgelegt

von M. Phys. Sergey Maltsev

geboren am 02. November 1981 in Leningrad, Russland

Gutachter: Prof. Dr. Dieter Freude

Prof. Dr. Christian Jäger

Prof. Dr. Helmut Cölfen

Tag der Verleihung: 21. Januar 2008



Bibliographische Beschreibung:

Maltsev Sergey

Structural elucidation of nanocrystalline biomaterials

Universität Leipzig, Dissertation

137 S., 128 Lit., 57 Abb.

**Referat:**

Bone diseases, such as osteoporosis and osteoarthritis, are the second most prevalent health problem worldwide. In Germany approximately 5 millions people are affected by arthritis. Investigating biomineralization processes and bone molecular structure is of key importance for developing new drugs for preventing and healing bone diseases. Nuclear magnetic resonance (NMR) [2] was the primary technique used due to its advantages in characterising poorly ordered and disordered materials [3]. Compared to all the diffraction techniques that widely applied in structural investigations, the usefulness of NMR is independent of long range molecular order. This makes NMR an outstanding technique for studies of complex/amorphous materials. Conventional NMR experiments (single pulse, spin-echo, cross polarization (CP) [4], etc.) as well as their modifications and high-end techniques (2D HETCOR [5], REDOR [6], etc.) were used in this work. Combining the contributions from different techniques enhances the information content of the investigations and can increase the precision of the overall conclusions. Also XRD, TEM and FTIR were applied to different extent in order to get a general idea of nanocrystalline hydroxyapatite crystallite structure.

Results:

- A new approach named "*Solid-state NMR spectroscopy using the lost I spin magnetization in polarization transfer experiments*" [7] has been developed for measuring the transferred I spin magnetization from abundant nuclei, which is normally lost when detecting the S spin magnetization.
- A detailed investigation of nanocrystalline hydroxyapatite core was made to prove that proton environment of the phosphates units and phosphorus environment of hydroxyl units are the same as in highly crystalline hydroxyapatite sample.
- Using XRD it was found that the surface of the hydroxyapatite nanocrystals is not completely disordered, as it was suggested before, but resembles the hydroxyapatite structure with  $\text{HPO}_4^{2-}$  (and some  $\text{CO}_3^{2-}$ ) groups instead of  $\text{PO}_4^{3-}$  groups and water instead of  $\text{OH}^-$  groups.
- The *organic-mineral interface of bone* was studied in order to clarify which organic molecules are in the closest spatial proximity to the bone mineral phase and to investigate the influence of the organic matrix on the mineral formation. It was found that most probably these molecules are glycosaminoglycan rather than a protein.



*I dedicate this dissertation to my family.  
There is no doubt in my mind that I would not be  
where I am today without their fullest support.*





## Acknowledgements

I would like to take this opportunity to express my sincere gratitude to all who helped and encouraged me!

Firstly I would like to thank my supervisor Prof. Dr. Christian Jäger for the opportunity to make this work here, at the Federal Institute for Materials Research and Testing (BAM, Berlin), for his help in numerous theoretical and experimental problems, for the useful discussions that brought me to a higher level of understanding, and for the very friendly atmosphere in the working group as well as for the tastiest “Thüringer Bratwurstchen”.

Also I would like to thank Prof. Dr. Dieter Freude from the University of Leipzig who took care about all organization problems that usually arise, especially if one studies as an external and works in another city. I appreciate his help very much!

Special thank goes to all my colleagues in FG I.3 for their help with scientific and organization questions. Especially I would like to thank Mario Fichera who always lends a helping hand to me in all kinds of questions and problems. Andrea Karrasch helped me to understand the best way to write my articles, posters and dissertation such that anyone could understand it. I thank Alf Pawlik for his support in all questions concerning modern software and hardware. I would like to thank Dr. Frank Malz for the stability of the spectrometers and for the helpful discussions about NMR basics in the beginning of my PhD as well as for help in organization problems.

Dr. Burkhard Peplinski provided numerous insights into crystallography and X-ray diffraction, carried out the XRD measurements as well as helped me much in preparation of my thesis and for that I am very grateful.

No measurements can be carried out without a sample! I am very grateful to Dr. Melinda Duer and her scientific group for the bone samples provided and for the fruitful collaboration.

My kind regards I address to Dr. Dave Reid for the very helpful and interesting discussions we had about wonderful world of chemistry as well as for his inestimable help in correcting of my thesis. Many thanks to Erica Wise for the pleasant teamwork.

Great thanks to Dr. Helmut Cölfen from Max Planck Institute in Golm for the discussions about XRD and the opportunity to use the XRD pattern fitting software.

Many thanks to Dr. Dietmar Pfeifer for scientific discussions.

Special thanks go to Chem.-Ing. Wolfgang Altenburg for his assistance in preparing the experiments and maintaining the spectrometers.

Also, I am very thankful to Dr. Michael Menzel for his kind support and assistance in all questions and problems.

Financial support from ARC/DAAD and DFG is gratefully acknowledged.

And last, but not least I would like to thank my dear mother Natalia, my father Yuri, my sister Alexandra and, of course, my dear wife Yunona for the inspiration and kindest support!

# Contents

1. Introduction.....	1
2. Biomineralization .....	4
2.1. General principles of biomineralization.....	5
<i>Biomineralization steps</i> .....	6
<i>Organic matrix mediated biomineralization</i> .....	7
2.2. Biomineral calcium phosphates .....	8
2.3. The structure of bone .....	11
2.4. Collagen structure .....	13
2.5. Noncollagenous proteins and other organics of the collagen matrix.....	18
2.6. Bone mineral phase.....	18
2.7. Organic-inorganic interface in bone.....	19
2.8. Previous structural studies of bone and related materials .....	20
2.9. Conventional structural studies.....	23
3. Nuclear Magnetic Resonance for studying nanocrystalline biomaterials .....	26
3.1. Introduction to NMR spectroscopy of spin-1/2 nuclei.....	27
3.2. Essential SSNMR interactions and Magic Angle sample Spinning.....	30
3.3. Essential techniques for solid-state NMR .....	35
3.4. Additional Solid-State NMR techniques.....	44
4. Direct detection of the indirect dimension of a standard 2D HETCOR.....	47
4.1. Materials and methods .....	48
4.2. Results and Discussion .....	49
4.3. Conclusions.....	55
5. Nanocrystalline hydroxyapatite: NMR and XRD structural investigations .....	57
5.1. Stoichiometry of the crystalline core .....	61
5.2. Why does the surface layer not contribute to the XRD lines?.....	65
5.3. Conclusions.....	73

6. Mineral phase of bone characterization .....	75
6.1. NMR experiments on the bone samples.....	77
6.2. Results and discussion.....	89
6.3. Conclusions .....	93
7. Organic-mineral interface in bone.....	95
7.1. Experiments and discussion .....	95
7.2. Conclusions .....	102
8. Conclusions and outlook.....	103
9. Appendix.....	106
9.1. Abbreviation list .....	106
9.2. Experimental parameters.....	107
10. Literature .....	116

# 1. Introduction

Bone consists of inorganic and organic components. Hydroxyapatite, a crystalline mineral salt of calcium, represents the main fraction (43% by volume of wet cortical bone) [8] of the mineral phase [1]. The organic part of bone comprises 25% by volume of water and 32% by volume of organic matrix [8], mainly Type I collagen [1]. Bone growth control involves a great variety of factors, including glycosaminoglycans, osteocalcin, osteonectin, bone sialoprotein, and the cell attachment factor. Bone diseases, such as osteoporosis and osteoarthritis, are the second most prevalent health problem worldwide. In Germany approximately 5 million people are affected by arthritis [www.medizinfo.de].

**Arthritis** (from Greek *arthro-*, joint + *-itis*, inflammation) describes a group of conditions involving damage to the joints of the body. It is the leading cause of disability in the percentage of the population over the age of 65. Osteoarthritis, the most common form of arthritis, occurs following a trauma to or an infection of the joint or simply as a result of aging. Osteoporosis is a disease involving reduction of bone mineral density, disruption of bone microarchitecture, and alteration of the amount and variety of non-collagenous bone proteins and other macromolecules. It affects all ages and predisposes to bone brittleness, fractures, and pain.

**Osteoporosis** is defined by the World Health Organization (WHO) in terms of either a bone mineral density 2.5 standard deviations below peak bone mass (20-year-old sex-matched healthy person average), or the occurrence of any fragility fracture. While treatment modalities, such as drug therapy using bisphosphonates, are improving, prevention is still considered the most effective way to reduce fracture. More women, particularly after menopause, suffer from osteoporosis than men, due to its hormonal component. Other risk factors are various hormonal conditions, smoking and some medications, especially glucocorticoid steroids.

Nuclear magnetic resonance (NMR) [2] was the primary technique used due to its advantages in characterising poorly ordered and disordered materials [3]. Compared to all the diffraction techniques that widely applied in structural investigations, the usefulness of NMR is independent of long range molecular order. This makes NMR an outstanding technique for studies of complex/amorphous materials. Moreover, analysis of homo- and heteronuclear dipolar couplings and relaxation phenomena significantly extends the information available from NMR. For example, dipolar coupling effects can provide interatomic distance information; in amorphous or disordered materials these can give interatomic distance distribution, and are of key importance for organic-mineral interface studies.

Conventional NMR experiments (single pulse, spin-echo, cross polarization (CP) [4], etc.) as well as their modifications and high-end techniques (2D HETCOR [5], REDOR [6], etc.) were used in this work. Combining the contributions from different techniques enhances the information content of the investigations and can increase the precision of the overall conclusions. For instance application of a spin-echo sequence at the beginning of a REDOR experiment filters out most of the organic proton signals overlapping over the mineral OH<sup>-</sup> signal. This simplifies and enhances the experimental data dramatically. Similarly a short CP step after a REDOR sequence limits polarization to the closest atom pairs (e.g. <sup>1</sup>H-<sup>31</sup>P) which thus contribute preferentially to the REDOR dephasing curve. Comparing this curve to the original REDOR dephasing curve gives additional information about interatomic distance distribution. An effective use of refinements like these should elucidate the molecular structure of such a complex material as bone in unprecedented detail.

Also XRD, TEM and FTIR were applied to different extent in order to get a general idea of nanocrystalline hydroxyapatite crystallite structure.

---

The objectives of the present work are:

- elucidation of structural diversity in the core and at the surface of nanocrystalline hydroxyapatite,
- characterization of bone mineral,
- development of a technique for characterization of the bone organic-mineral interface.

This should provide new information leading to deeper understanding of mineralization processes in healthy, and diseased, bone.

## 2. Biomineralization

*Biomineralization* refers to the formation, structure and properties of inorganic solids deposited in biological systems [1]. Consequences of biomineralization can be found wherever organic life meets the inorganic environment, such as algal sediments, shells and corals, bones and teeth and many other hard or amorphous deposits. Due to the special physical properties of biominerals, they mostly play defensive or structural roles. From a material science perspective, organic molecules are soft, compliant and fracture resistant while inorganic crystals are hard and brittle. Biomineral composites combine the best of these properties and minimize the weaknesses: they are both hard and fracture resistant (tough) [9]. This is due to several factors: structure, nano size and chemical composition. The variety of biominerals encompasses approximately 60 mineral types, and a wide range of proteins, glycoproteins and polysaccharides. The former are comprised of different inorganic salts, mostly calcium carbonates and phosphates or silicates, and can be crystalline or amorphous.

From the healthcare point of view, understanding the principles of biomineralization is of major importance: there is huge global expenditure on bone-disease research and care for sufferers. There is a considerable need for new drugs to effectively control bone resorption and destruction, and cartilage mineralization; rational design of such medicines is only possible with a good knowledge of the organic and mineral structures of bones and joints, and the processes occurring during tissue formation and solidification.

The mechanisms of biomineral formation are only understood [10] at a basic level; each system has its own distinct molecular templating, influences on crystal composition, growth characteristics, and resultant shape and size.

Although biominerals are of interest in their own right because of their special properties, they may also provide inspiration for new materials, avenues for novel drug design, and insights into the genetic control of biological structure.



## 2.1. General principles of biomineralization

Although little is known about biochemical processes governing mineral precipitation in live tissues, some general rules underlying common principles can be established. Lowenstam [11] introduced the distinction between biologically induced mineralization, and biologically controlled (or organic matrix mediated) mineralization. The difference is obvious: in the first case, precipitation occurs from supersaturated solution and requires a living system to induce nucleation, and due to the stochastic character of mineral deposition there is no order in the sediments. Shape, composition and structure are usually poorly defined and irregular.

In the second case, a living system is required both for nucleation to start and for controlling the mineralization processes. An important generalization with respect to biologically-controlled mineralization is that the mineralization takes place within defined and restricted compartments or spaces [1]. This means that initial compartmentalization is essential, and mechanisms to transfer ions and organic molecules into and through the space must exist.

Four main sites for biomineralization can be distinguished in living tissue: on the cell wall (*epicellular*), in the spaces between closely packed cells (*intercellular*), inside enclosed compartments within the cell (*intracellular*) and outside the cell, within or on an insoluble macromolecular framework (*extracellular*) [12]. This work primarily deals with *extracellular* organic matrix mediated biomineralization, as exemplified by bone.

Although a high degree of mineralization control persists during all mineralization steps, crystalline as well as amorphous or poorly ordered sediments can be deposited.

## Biom mineralization steps

### **Supersaturation and nucleation**

Before a solid can precipitate from solution, a certain degree of supersaturation has to be attained. For crystallization to proceed, ionic clusters (nuclei) of a certain critical size, which are resistant to rapid dissolution, have to be formed. The critical nuclear size depends on the degree of supersaturation of the solution. Nuclei above this size continue to grow, while those below it redissolve. Two forms of nucleation are possible: homogeneous (the solution contains only the ions that form mineral) and heterogeneous (the solution contains foreign particles, surfaces, etc.) [13].

### **Crystal growth**

Crystal growth proceeds by incorporation of new structural elements on the surface of nuclei. The most favourable places for crystallization are structural imperfections such as kinks and dislocations, and sites where the crystal lattice is distorted or foreign particles are present. The crystal modification and morphology is determined by kinetic and thermodynamic parameters as well as by the presence of other substances [13]. For example,  $Mg^{2+}$  ions force supersaturated solutions of  $CO_3^{2-}$  and  $Ca^{2+}$  to mineralize to aragonite rather than calcite [14].

### **Termination of crystal growth**

The main reasons for growth cessation are: the concentration of dissolved ions falls below supersaturation levels, and the appearance or increase in concentration of inhibitor molecules or substances fills up the delineated space. The form and morphology of the crystalline product are governed by the specific sites and stages of growth termination, and the overall shape of the space available to the growing mineral.

Living organisms are able to control the mineralization process at some, or all, of the stages, and so determine the structure, morphology and size of the mineral deposit. The main ways to manage the crystal's growth behaviour are: chemical, spatial, structural, morphological and constructional. Ion transport through the cell wall, as well as molecular transport of inhibitors and catalysts, controls the

supersaturation state, thus crystal nucleation and growth, directly. Spatial control is exerted by the size and shape of the room available for crystallization. Mostly these are preconstructed organic borders of a compartment. Specific crystal phases can grow up preferentially due to the structural control which is exerted by spatial organization of charged organic units on the walls of a compartment. The changes between crystal phases are controlled by additional molecules which are able to catalyse or inhibit phase transitions, which is a type of morphological control. The overall shape of a deposit is governed by organic boundaries, giving rise to a vast array of different shapes such as, for example, in seashells.

## Organic matrix mediated biomineralization

Although the mechanisms that govern the biological control of mineralization vary enormously between different systems, there are four basic requirements associated with mineralization sites such as vesicles and macromolecular frameworks: spatial delineation, diffusion-limited ion flow, chemical regulation, and organic surfaces [12]. Macromolecular frameworks are extracted into sealed-off spaces as insoluble proteins and polysaccharides. After establishing an organic matrix the mineral deposition starts inside the spaces.

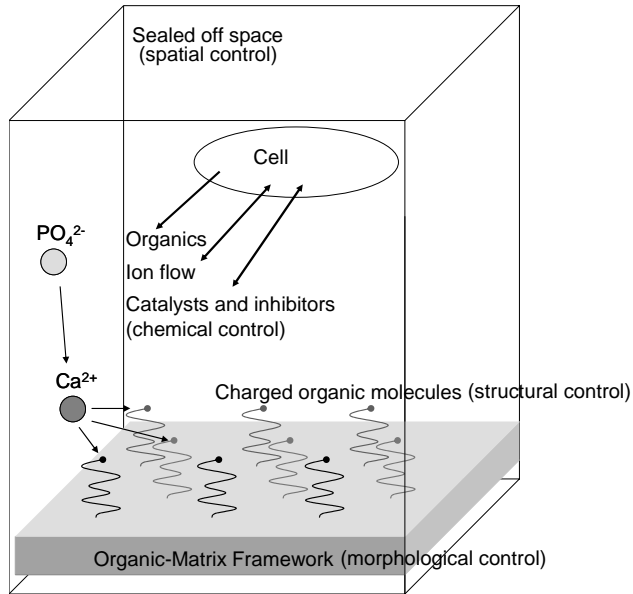


Fig. 2.1 Schematic view of matrix-mediated biomineralization.  $\text{Ca}^{2+}$  ions are attracted from the solution to the charged organic molecules. After this, positively charged Ca ions attract  $\text{PO}_4^{3-}$  units thus providing suitable conditions for crystallization. Structural which grow preferentially. The cell controls the molecular and ion content of the supersaturated solution.

Mostly the framework is built in a way to fulfil two tasks: insoluble proteins form the backbone and charged molecules attract ions from the supersaturated solution thus controlling the mineralization processes spatially and structurally. Fig. 2.1 summarizes the total view of organic matrix mediated biomineralization schematically.

## 2.2. Biomineral calcium phosphates

Several calcium phosphate compositions are mineralized by living organisms. Among the most common are hydroxyapatite, octacalcium phosphate and amorphous calcium phosphate (ACP). These occur in bones, teeth, milk, saliva, etc. Due to ACP's lack of a well defined crystalline form its composition is best defined as being close to  $\text{Ca}_3(\text{PO}_4)_{1.87}(\text{HPO}_4)_{0.2}$  [15] at moderate pH values.

Laboratory synthesized ACP mostly assumes a sphere-like shape with a diameter dependent on the preparation conditions. In contrast, hydroxyapatite presents a needle-like crystal shape with a well defined crystal structure and with chemical formula  $\text{Ca}_{10}(\text{PO}_4)_6(\text{OH})_2$  (Fig. 2.2). Since crystallization of every mineral phase has its own free energy threshold, the crystal growth in solution can occur via a sequential process that involves both structural and compositional modifications of precursor and intermediate phases. It is more likely that precipitation precedes via the following phases: an amorphous phase solidifies first, than it is modified to an intermediate crystalline phase (octacalcium phosphate, dicalcium phosphate dihydrate) and finishes in the final crystalline phase - hydroxyapatite.

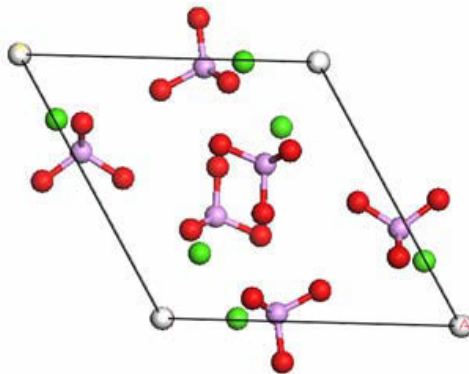
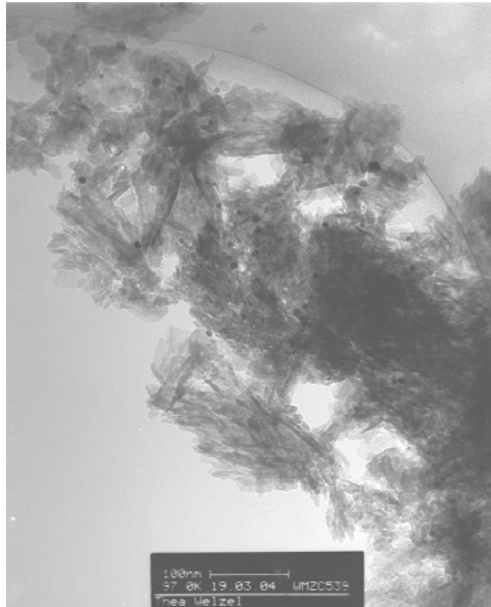


Fig. 2.2 Hydroxyapatite (viewed along the crystal *c*-axis). Green represents calcium ions, red – oxygen, white – hydrogen, magenta – phosphorus.

Such a process is energetically more favourable than direct crystallization of hydroxyapatite from solution since the energy threshold for the direct crystallization is greater than for step-by-step crystallization [12].



*Fig. 2.3* TEM image of the nanocrystalline hydroxyapatite sample.  
*Adapted from Jäger et al. [16]*

Mineralized by a living organism as a part of the bone or tooth, calcium phosphates present nanocrystals separated by organic matrix framework. In contrast to geologically mineralized crystals, nanocrystals have much higher surface/volume ratio and surface effects, such as strain, lattice defects and incorporations, and substitutions, begin to play a crucial role in chemical properties of the substance. This is clearly seen for nanocrystalline hydroxyapatite, the remarkable properties of which are used in attempts to heal osteoporosis, in drug delivery, and in tissue engineering and bone- and tooth-repair applications.

Prepared by chemical precipitation [17] a nanocrystalline hydroxyapatite sample presents a cigar-like shape with mean dimensions 10x10x40 nm (Fig. 2.3) [16]. Since the unit cell dimensions for hydroxyapatite are 9.424x9.424x6.879 Å there are only few cells in each dimension and this leads to enormous line broadening in all diffraction methods. Therefore the methods are of limited use for characterizing the internal structure of the crystallites. TEM, chemical analysis and NMR are utilized for structural investigations of such small and complex materials.

Typical dimensions of biomineralized calcium phosphate in bones are even smaller – about  $40 \times 20 \times 3$  nm [12]– and therefore surface effects play an even greater role and should not be ignored in structural investigations. Due to the complicated structure of bone it is hard to analyse hydroxyapatite crystals directly. Hence, *in vitro* nanocrystalline samples are studied as an intermediate phase between highly crystalline samples and bone nanocrystals. This allows investigation of the crystalline phase independently from the organic matrix and establishing experimental approaches to structural and composition characterization procedures which can be utilized for bone investigations.

## 2.3. The structure of bone

Bones are the rigid organs that form the endoskeleton of vertebrates. Bones have several functions: they provide the frame for the body's shape and movements, protect internal organs, serve as a mineral storage, and undertake blood production. There are several types of bones: long, short, flat, irregular and sesamoid bones. The regional and internal structures of a long bone are presented in Fig. 2.4.

Several tissues are involved in bone formation: highly mineralized osseous tissue or bone tissue which is the main tissue of all bones, marrow, periosteum (a thin layer of dense, irregular connective tissue that covers the outer surface of a bone in all places except at joints), nerves, blood vessels and cartilage.

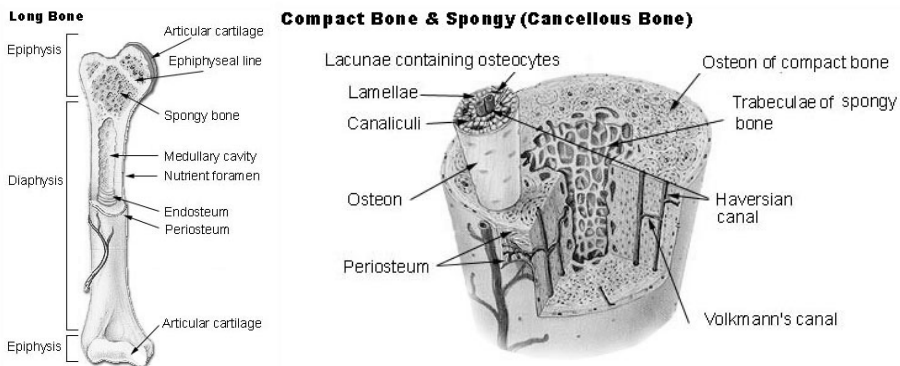


Fig. 2.4 Bone subunits on different scales. The pictures are taken from wikipedia.com.

Looking deeper into the bone tissue, several remarkable structural features can be noticed. Going from molecular structure up the length scale, these are mineralized tropocollagen, which is bundled in fibrils; the fibrils are then organized in layers and form osteons – cylindrical structures with a canal in the centre with blood vessels and nerves (Fig. 2.5). Further osteons form bone micro- and macrostructure. Collagen forming and destroying cells – osteoblasts and osteoclasts - are between the collagen layers and connected among themselves with a net of channels to provide nutrition and waste removal. In humans, cortical bone is composed mainly of densely packed Haversian systems (osteons). In the infant, primary osteons are formed by ingrowth of periosteal blood vessels that follow the osteoclastic “cutting cone” which tunnels through the existing cortex. Osteoblasts occupying the vessel-filled tunnel deposit concentric layers of bone matrix. The typical osteon is a cylinder measuring approximately 200–250  $\mu\text{m}$  in diameter with the most recently deposited mineral at its center. Another cell type is the osteocytes, which originate from osteoblasts, but do not produce new bone tissue. Their main tasks are calcium homeostasis and matrix maintenance. They also probably serve as mechano-sensors. Bone lining cells are inactive osteoblasts. The activity ratio of osteoclasts and osteoblasts determines whether the bone mass increases or decreases. Osteoporosis is often associated with malfunction of osteoblasts while osteoclasts still continue to destroy the tissue.

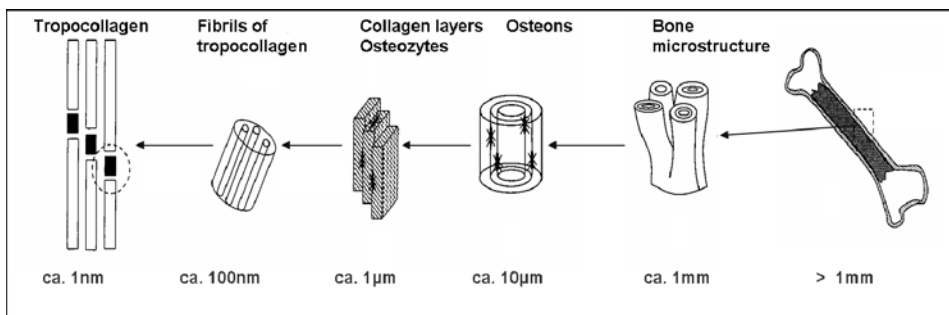


Fig. 2.5 Bone structure on different length scales.



## 2.4. Collagen structure

Bone collagen is essentially built from type I collagen [1]. The key feature defining a collagen is the presence of continuous or interrupted sequences in the individual polypeptide chains of repeated  $(GXY)_n$  amino acid sequence domains, where G is Glycine and X and Y may be any amino acid. These domains on one polypeptide chain interact with similar domains on two additional chains to form compound triple-helical units with characteristic folding, the “collagen-fold”. In the vertebrate collagens, X is frequently Proline and Y is either Proline or Hydroxyproline. The 40 different chains can assemble into triple-helical structures, with the requirement that the lengths of the  $(GXY)_n$  domains on each chain must match the length on the partner chains so that stable triple-helical segments can be formed [1] (Table 2.4-1).

*Table 2.4-1 Relative content and characteristic peaks positions of the most frequent amino acids in organic matrix of bone [18].*

Amino acid name	% in bone matrix	Site	Chemical shift, ppm
Glycine	31.0	C'	174.0
		$\alpha$	45.4
Proline	11.1	C'	176.7
		$\alpha$	63.3
		$\beta$	32.0
		$\gamma$	27.4
		$\delta$	50.4
Alanine	10.4	C'	177.8
		$\alpha$	53.2
		$\beta$	19.04

Glutamic acid	7.6	C'	176.9
		$\alpha$	57.5
		$\beta$	30.2
		$\gamma$	36.2
		$\delta$	182.3
Glutamine		C'	176.4
		$\alpha$	56.6
		$\beta$	29.3
		$\gamma$	33.8
		$\delta$	179.1
Hydroxyproline	6.9	C'	175
		$\alpha$	61
		$\beta$	39
		$\gamma$	71
		$\delta$	54
Aspartic acid	5.8	C'	176.5
		$\alpha$	54.6
		$\beta$	41.0
		$\gamma$	177.0
Asparagine		C'	175.2
		$\alpha$	53.4
		$\beta$	38.9
		$\gamma$	176.6
Arginine	4.7	C'	176.5
		$\alpha$	56.9
		$\beta$	30.87
		$\gamma$	27.42
		$\delta$	43.21
		$\epsilon$	158.98
Serine	4.7	C'	174.6
		$\alpha$	58.6
		$\beta$	63.9

Valine	3.3	C'	175.8
		$\alpha$	62.6
		$\beta$	32.8
		$\gamma_1$	21.6
		$\gamma_2$	21.4
Theonine	2.7	C'	174.6
		$\alpha$	62.2
		$\beta$	69.6
Lysine	2.6	$\gamma$	21.7
		C'	176.5
		$\alpha$	56.9
		$\beta$	33.0
		$\gamma$	25.2
Isoleucine	2.2	$\delta$	29.0
		$\epsilon$	42.0
		C'	175.9
		$\alpha$	61.6
		$\beta$	38.8
		$\gamma_1$	28.0
Phenylalanine	1.8	$\gamma_2$	17.7
		$\delta$	13.8
		C'	175.5
		$\alpha$	58.1
		$\beta$	40.2
		$\gamma$	138.2
		$\delta_1$	130.8
		$\delta_2$	130.7
		$\epsilon_1$	129.4
$\epsilon_2$	129.4		
$\zeta$	128.2		

After molecular synthesis in osteoblasts procollagen molecules are secreted into the extracellular space, where they are trimmed, and assemble into fibrils. The fibrils consist of five-stranded microfibrils packed as shown in the Fig. 2.6 and Fig. 2.7 [19]. The microfibrils have the following structural features:

- full length is 5 times the D-period (234 residues or 67 nm) with a total length of about 300 nm and diameter of 1.5 nm
- gap (lacunar) regions between microfibrils are about 0.5 D (30-40 nm) in length and organized in a way to form approx. 25x3 nm channels
- cross-link zones are at the boundaries of the gap regions

Such a structure provides enough space for mineralization to occur in gap zones, between the fibrils and microfibrils. Adult wet bovine cortical bone is estimated to be 25% by volume water, 32% organic matrix and 43% mineral. Of the mineral 28% by volume is in the gap zone, 58% is radially intrafibrillar (in the pores) and 14% is radially extrafibrillar [1].

Many studies have shown that a collagen matrix by itself does not have the capacity to induce mineralization from a solution of calcium and phosphate ions at the appropriate pH, degree of saturation and temperature [20; 21]. Other ways of studying mineralization, such as Liquid-Phase Mineral Precursor [22] or phosphate precipitation in the presence of glucoseaminoglycans [23; 24] have been applied to investigate the possible mechanisms and features of organic controlled mineral deposition.

The organic matrix mediated models of mineral induction place the focus of mineral nucleation squarely on the organic matrix and, in particular, on the presence of proteins or polysaccharides with the ability to interact with and localize on the structural matrix, and, when bound, induce nucleation of the mineral deposition [11].

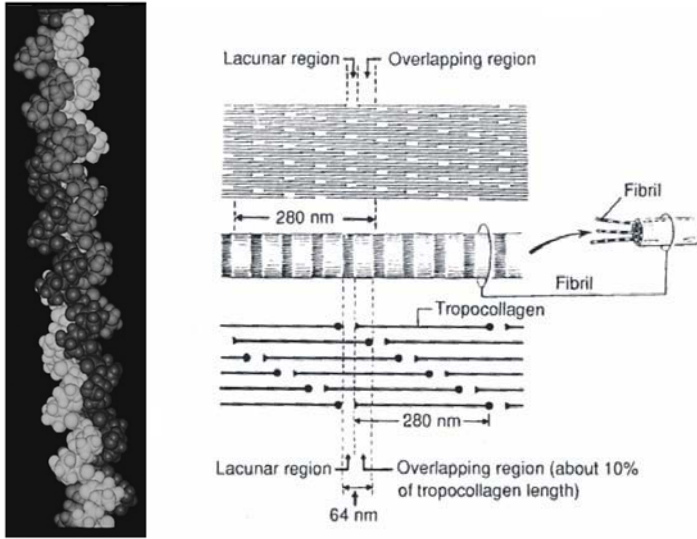


Fig. 2.6 Packing of collagen molecules into a collagen triple-helix (left), and microfibril organization (right).

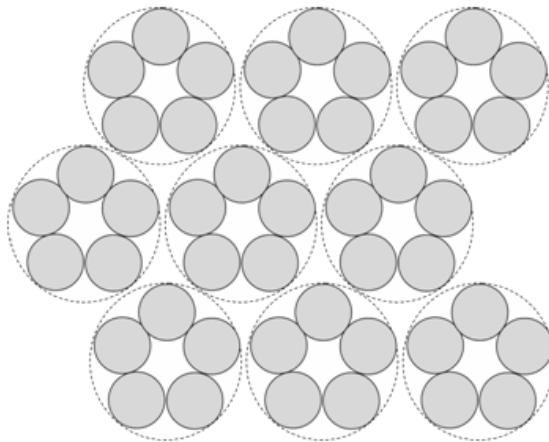


Fig. 2.7 Idealized model of collagen fibril packing. Inter- and intrafibrillar spaces are available for mineral deposition.

## 2.5. Noncollagenous proteins and other organics of the collagen matrix

Besides the collagen proteins there are about 200 other noncollagenous matrix proteins (NCPs), glycoproteins and glycosaminoglycans in the structure of fibrils. Some help to mineralize hydroxyapatite while some others inhibit or delay nucleation and growth processes.

The first acidic phosphoproteins of a mineralized matrix to be identified were in dentin. The major phosphoprotein was subsequently named “phosphophoryn” or phosphate-carrying protein, because it was more than 50 residue % serine of which 85-90% was phosphorylated [1].

*In vitro* studies of the mineral nucleating ability of osteocalcin, osteopontin, bone sialoprotein (BSP) and phosphophoryn (PP) suggested that BSP and PP could be nucleating agents, whereas osteopontin might function as an inhibitor of hydroxyapatite formation [25].

## 2.6. Bone mineral phase

In contrast to geologically generated apatites, crystals grown from a supersaturated solution or via biological processes are of nanoscopic size, nonstoichiometric, and lacking long-range order. With general chemical formula  $\text{Ca}_{10}(\text{PO}_4)_6(\text{OH})_2$  they may be  $\text{Ca}^+$ ,  $\text{OH}^-$  and  $\text{PO}_4^{2-}$  deficient and may be substituted by  $\text{F}^-$ ,  $\text{CO}_3^{2-}$ ,  $\text{HPO}_4^{2-}$ ,  $\text{Na}^+$ ,  $\text{Mg}^{2+}$ , etc. Early electron microscope investigations showed that the hydroxyapatite crystals in bone are plate or needle-like with the c-axis along the fibrils [12].

Although bone mineralization starts in the gap zones [26], there is not enough space to contain all the bone mineral phase in the gaps. The platy crystals that develop *in vivo* are larger than the gap zone space [27], thus mineralization penetrates further into the fibrils and interfibrillar space giving strength and stiffness to the bone. The processes are visually presented in Fig. 2.8.

## 2.7. Organic-inorganic interface in bone

All biomineralization processes are strictly governed by the internal organization and structural properties of the organic matrix. Due to the great number and variety of interacting of the interacting units and the complexity of the interactions, the processes are very hard to analyse, describe and model. A great deal of effort has been devoted to investigating the precipitation of bone-like apatites in the presence of different types of organic molecules in attempts to understand the motifs of organic matrix mediated mineral deposition.

The two main approaches are being simultaneously developed at present: protein mediated biomineralization, where such proteins as BSP [28] (bone sialoprotein) or osteocalcin [29] play a significant role in controlling the mineral deposition processes, and glycosaminoglycan [30] mediated biomineralization with chondroitin sulphate as the main representative. Historically it was assumed that proteins play the most active role in guiding the mineral phase solidification, but over recent years new evidence has emerged that glycosaminoglycans are in closer spatial proximity to the mineral phase than any protein. In both cases the concentration of highly acidic macromolecules, which also occur in high concentrations at mineralizing foci in distantly related organisms [31] such as molluscs and vertebrates, plays an attractive role for positively charged  $\text{Ca}^{2+}$  ions.

## 2.8. Previous structural studies of bone and related materials

Due to its remarkable mechanical, structural and biological properties bone as a material has always attracted a great deal of attention from the scientific community. Due to its poor sensitivity NMR was generally not useful, so histology, and microscopic and diffraction methods have been applied to clarify the structure on different length scales. However, the introduction of high-field superconducting magnets, significant progress in electronics as well as data processing and handling have pushed NMR to the forefront.

The first NMR studies of bones were devoted to characterization of the mineral phase using  $^{31}\text{P}$  and  $^1\text{H}$  NMR. They used synthetic hydroxyapatite and its nonstoichiometric forms, brushite, monetite, carbonatoapatites, octacalcium phosphate, etc. [32-34] to compare with bone, mineralised cartilage and dental enamel and to discriminate amorphous and crystalline phases in bone mineral. Carbonate ions, which replace phosphates and hydroxide ions in bone and synthetic apatites, were studied by  $^1\text{H}$  and  $^{13}\text{C}$  solid-state NMR [35] using heating and dipolar suppression to assign the spectral lines. Two types of substitutions were recognized by differences in heating behaviour and in chemical shift.



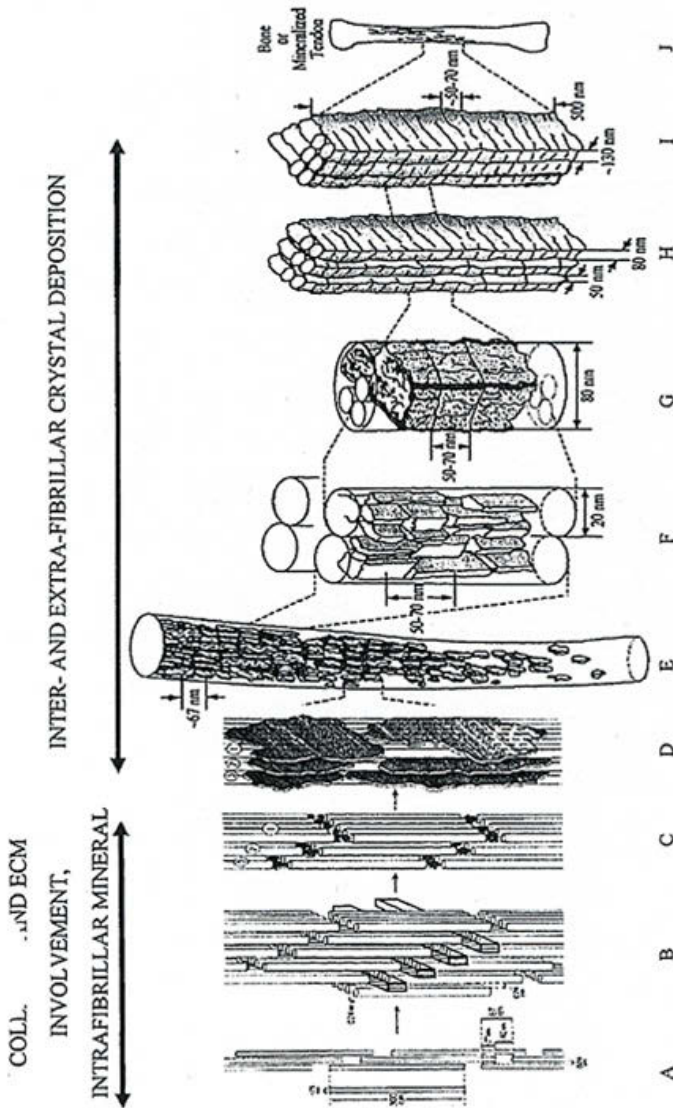


Fig. 2.1 Formation of bone mineral at different stages. Adapted from A. Veis [1]

The first 2D HETCOR experiments on bone samples were run by Santos *et al.* [36] in 1994 to separate different  $^{31}\text{P}$  sites with the same chemical shift. Also, this work showed that it was possible to separate the bone mineral  $^1\text{H}$  resonances from those from nonstructural water and organic material, making additional chemical treatment unnecessary.  $^1\text{H}$ - $^{31}\text{P}$  cross polarization kinetics of human trabecular bone mineral was studied by Kaflak *et al.* [37] who showed the presence of three structural components which were assigned to proton-rich, hydroxyapatite and proton-deficient phosphate domains. Furthermore, the group described a 2D HETCOR experiment and concluded there was a hydroxyl group deficiency in bone mineral compared to hydroxyapatite, and that there is no evidence that  $\text{HPO}_4^{2-}$  brushite-like ions are present in bone. The presence of  $\text{HPO}_4^{2-}$  units was debated for a long time until Cho *et al.* proved their presence in 2003 [38]. Also, it was shown that a significant fraction of  $\text{HPO}_4^{2-}$  units is located on the surface of the crystals and the concentration of unprotonated phosphates is greater within the mineral core than at the surface [39].

The organic-mineral interface at early stages of mineralization, concentrating on the role of phosphoproteins, was studied by Wu *et al.* [40], who found that by far the major phosphate components identified by solid-state  $^{31}\text{P}$  NMR in the very earliest stages of mineralization are protein phosphoryl groups which are not complexed with calcium. However, very small amounts of calcium complexed protein phosphoryl groups as well as even smaller, trace amounts of apatite crystals were also present at the earliest phases of mineralization. These data support the hypothesis that phosphoproteins complexed with calcium play a significant role in the initiation of bone calcification. Protein-driven mineralization was investigated in detail by the group of G. Drobny. They used a phosphorylated hexapeptide from the N-terminal region of statherin - a small, multifunctional protein, which inhibits primary and secondary precipitation of hydroxyapatite in saliva, as well as serving as a boundary lubricant [41]. Constant composition kinetic characterization demonstrated that, like the native statherin, this peptide inhibits the growth of hydroxyapatite seed crystals when preadsorbed to the crystal surface. Their results support a structural model where the N-terminus is disordered, potentially to maximize interactions between the hydroxyapatite surface and the negatively charged side chains found in this region, the middle portion is largely  $\alpha$ -helical and the C-terminus has either a more extended conformation or a

mixture of helix and extended conformations [42-44]. The protein-guided mineralization concept has also been studied *in vitro* by Shaw *et al.* using  $^{31}\text{P}$ - $^{13}\text{C}$  REDOR technique to determine the orientation of the COOH terminus of an amelogenin protein on the mineral surface. The experimental results provide direct evidence orienting the charged COOH-terminal region of the amelogenin protein on the hydroxyapatite surface, optimized to exert control on developing enamel crystals [45]. The backbone dynamics of isolated collagen fibrils have been studied by Aliev *et al.* using solid-state NMR  $^{13}\text{C}$  chemical shift anisotropy and  $^2\text{H}$  quadrupolar line shape analysis. The results showed that motional averaging of the NMR interactions occurs primarily via small-angle librations about internal bond directions. This type of dynamics is compatible with both the presence of cross-links in collagen and the X-ray data, as well as dynamic models used for other proteins [46].

Polysaccharide mobility in cartilage was studied by Huster *et al.* Since cartilage composition is very similar to that of bone: collagen, proteoglycans, water and hydroxyapatite, these studies were crucial for further polysaccharide-mineral interactions investigations. Their results showed an increase in fast and slow motions in collagen with increasing hydration. These motions are segmental and are due to water molecules that associate with polar groups in the collagen structure [47; 48].

## 2.9. Conventional structural studies

Rey *et al.* used FTIR for bone mineral phase investigations in 1989. Their results showed that non-apatitic environments of phosphate and carbonate ions occur in bone mineral [49]. *In vitro* FTIR studies of  $\text{CO}_2$  incorporation in hydroxyapatite were reported in 1998 by Cheng *et al.*, who showed that the 1414, 1447 and 1500  $\text{cm}^{-1}$  bands were assignable to  $\text{CO}_3^{2-}$  ions in  $\text{OH}^-$  sites of the CaHAP crystals and the 1457 and 1550  $\text{cm}^{-1}$  bands to  $\text{CO}_3^{2-}$  ions in  $\text{PO}_4^{3-}$  sites. This assignment is different from those in the literature. The results demonstrated that the inclusion of  $\text{CO}_3^{2-}$  ions in  $\text{PO}_4^{3-}$  sites is maximal for CaHAP formed at pH 5.94, and that in  $\text{OH}^-$  sites increases as the solution pH rises [50]. Most current research on protein-mediated mineralization with FTIR imaging is being done by Ling *et al.* on dentin matrix

protein (DMP1) *in vivo*. They find that DMP1 has multiple roles (both direct and indirect) in the regulation of postnatal mineralization [51].

XRD studies on bone material started in the 1940s and rat bone mineral content was characterized by Hirschman *et al.* as  $[\text{CaHPO}_4]_{1.6} [\text{CaCO}_3] [\text{Ca}_3(\text{PO}_4)_2]_{2.0}$  [52]. Later in the 60s, investigation concentrated on line broadening to estimate crystal sizes [53; 54]. One of the best known XRD works on bone mineral investigation was by Eanes *et al.* in 1970 on calcified turkey tendon, which discovered d-spacing [55] between collagen fibres filled with crystalline calcium phosphate. It was also found that the presence of mineral appears to increase the resistance of collagen to permanent thermal denaturation.

Mineral phase of human foetal bones were investigated in 2003 by Dalconi *et al.* and proved that early-forming bone minerals can be described by a calcium–phosphate phase (bioapatite) whose structure closely resembles that of hexagonal hydroxyapatite. The bioapatite crystallites are small, elongated along the crystallographic c-axis, and grow as bone maturation proceeds [56].

Thermal behaviour of bone mineral was investigated by Danilchenko *et al.* by XRD and showed that the thermal behavior of the bone mineral depends not only on the structural distortions, but also on the crystal habit, texture and ordering of biocrystals in tissue. The temperature growth of biogenic apatite crystals, unlike synthetic hydroxyapatite, is seen to be non-monotonic and multi-staged. At 600 to 700°C the biomineral crystallites grow rapidly due to disappearance of the mosaic structure as the lattice imperfections are annealed. After heating between 700°C and 900°C the bone mineral appears to be composed of roughly equidimensional  $\geq 200$  nm crystals. The further growth of the crystals in the range from 900 to 1300°C occurs by the mass transport mechanism, supporting the idea that the bone mineral is not a discrete aggregation of crystals, but rather a continuous mineral phase with direct crystal-crystal bonding [57].

M. Epple's group studied bone samples in 2000 with modern solid-state chemical methods: combined thermogravimetry, differential thermal analysis, mass spectrometry (TG-DTA-MS), X-ray powder diffraction (synchrotron),

X-ray absorption spectroscopy (EXAFS, Ca K-edge, synchrotron), and infrared spectroscopy. The results complement those from medical histology. It was shown that the mineral phase consists of disordered apatite with no indication of another calcium phosphate phase. Size and morphology of the bone mineral particles are independent of the nature of the bone sample, but there are significant differences in the overall composition of the bone samples and in the carbonate content of the mineral phase. It was concluded that the biological resorption of living bone (remodeling) is closely related to morphology and composition of its mineral phase [58].

### 3. Nuclear Magnetic Resonance for studying nanocrystalline biomaterials

This chapter describes the principal experimental techniques that are used for biomaterials' structure investigations. Because of nanoscopic particle size of precipitated biomaterials such as bones, teeth, seashells, synthetic materials, etc. one has to deal with rather large relative surface volume fractions. Stress in the surface due to sudden change of chemical composition transforms into stress towards the interior covering several unit cells. Hence, not only Bragg peak broadening occurs due to the geometric dimension of the surface layer but also a broadening due to internal stresses (slight distribution of bonding distances and angles). In addition it was found that, particularly on precipitated materials, the surface may have and has indeed a different chemical composition. E.g. nanocrystalline hydroxyapatite surface contains  $\text{HPO}_4^{2-}$  units [16]. Disorder in crystal surface becomes more relevant as crystal size decreases and this leads to more complex NMR spectra. Moreover structural complexity of the natural samples makes the spectra overloaded. All this leads to very tricky NMR experiments that demand high-precision setup and high-quality data to evaluate. It is common that quality of the experimental data grows nonlinear with time and the consequence is hugely experimentally time consuming. This is the reason why an experiment should be organised in a way to get satisfactory data in a reasonable time and a key point for this in NMR is programming the pulse sequences for spectrometer. Several aspects should be kept in mind during preparation of a pulse program:

- ability to get only the signals of interest (spectral editing)
- use of saturation because of different relaxation times ( $T_1$ ,  $T_2$ ) for different structural units
- suppression of spin-diffusion
- high-precision setup of pulses, especially for long REDOR experiments
- proper phase cycling

Conventional as well as high-end experiments that are used in the study are explained in this chapter together with basic NMR theory.

The experiments include: Single Pulse, Spin-Echo (also Rotor Synchronized Echo), Cross Polarization, Rotational Echo Double Resonance (REDOR), Heteronuclear Correlation (HETCOR), Homonuclear Correlation and their combinations. A new technique called “*Direct detection of the indirect dimension of a standard 2D HETCOR*” is described in detail in the next chapter.

A detailed description of solid-state NMR theory and experiments is given in number of books. “Spin dynamics” by Prof. Malcolm H. Levitt is probably the best one to start with.

### 3.1. Introduction to NMR spectroscopy of spin-1/2 nuclei

The total Hamiltonian of a nucleus in a magnetic field is [59]:

$$\hat{H} = \hat{H}_0 + \hat{H}_M \quad 3.1-1$$

where  $H_0$  is the unperturbed Hamiltonian of the nucleus, and  $H_M$  is perturbation due to the Zeeman interaction with magnetic field along z-axis [59]:

$$\hat{H}_M = -\gamma_I \hbar B_0 \hat{I}_z \quad 3.1-2$$

where  $\gamma_I$  is the atom’s gyromagnetic ratio. The quantity  $\omega_0 = -\gamma_I B_0$  is called Larmor frequency and is specific for each isotope. Further, only spin-1/2 atoms are supposed and  $\hbar$  is omitted. Zeeman interaction splits energy levels with  $m = \pm 1/2$  as shown in Fig. 3.1.

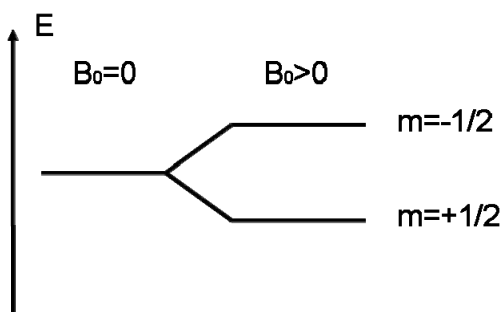


Fig. 3.1 Energy levels diagram for spin-1/2 nuclei with and without external magnetic field.

The populations  $p$  of the energy levels in thermal equilibrium are governed by Boltzman distribution [59]:

$$\frac{p_{\beta}}{p_{\alpha}} = e^{-\frac{\Delta E}{k_B T}} \quad 3.1-3$$

The lower energy state ( $m=+1/2$ ) is usually referred to as  $\alpha$  and more energy state ( $m=-1/2$ ) is referred to as  $\beta$ .

Net magnetization vector of a sample in thermal equilibrium is given by the expression [59]:

$$M_z = \frac{2k_B T}{\gamma B_0} (p_{1/2} - p_{-1/2}) \quad 3.1-4$$

where  $p_{1/2}$  and  $p_{-1/2}$  are the populations of  $1/2$  and  $-1/2$  states, respectively.

To force the transitions between the energy states a radiofrequency (RF) pulse has to be irradiated. The interaction term of the RF pulse with I spin can be given as [59]:

$$\hat{H}_{rf} = -\gamma_i B_1 (\cos(\omega_{rf} t) \hat{I}_z + \sin(\omega_{rf} t) \hat{I}_y) \quad 3.1-5$$

Here it is supposed that  $B_1$  is along the x-axis, and thus perpendicular to  $B_0$  and  $\omega_{rf}$  is the irradiation frequency. In the case of  $\omega_{rf} \approx \omega_0$  energy of RF pulse can be effectively absorbed forcing the spin to change its state with so-called *nutaton frequency* [59]:

$$\omega_{nut} = |\gamma B_{rf}| \quad 3.1-6$$

Basic NMR experiment consists of an RF pulse followed by an acquisition interval. Mostly, a pulse is a fracture of a nutation period and is measured in degrees as follows:

$$t_{deg} = \frac{t_{rf} \omega_{nut}}{2\pi} 360^\circ \quad 3.1-7$$

where  $t_{rf}$  is the pulse duration. Applied perpendicular to the z-axis a  $90^\circ$  pulse has an effect of populations' equalization simultaneously to coherence excitation in xy-plane corresponding to [59]:

$$\hat{R}_\alpha(90^\circ) \hat{I}_z \hat{R}_\alpha^{-1}(90^\circ) = -\hat{I}_{90^\circ+\alpha} \quad 3.1-8$$

where  $\hat{R}_\alpha$  is a rotational operator over the  $\alpha$ -axis. The same expression 3.1-8 is valid for RF pulse-effect calculations with arbitrary angle over any axis. It can be further generalized by accounting commutation relationship for spin operators [59]:



$$[\hat{I}_x, \hat{I}_y] = i\hat{I}_z \quad 3.1-9$$

If the phase of a pulse is the same as transverse magnetization vector has, than this pulse is called *spin lock pulse*, since its effect on the spin system is equal to rotating a vector around itself.

In the spectrometers RF coil (which is usually used for both pulse irradiation and signal acquisition) the magnetization, precessing with  $\omega_0$ , produces an oscillating magnetic flux density [3]:

$$\vec{B}(t) = \mu_0 \vec{M}(t) \quad 3.1-10$$

resulting in a voltage  $U = -\frac{d\Phi}{dt}$  with  $\Phi(t) = \int \vec{B}(t)d\vec{A}$ . The oscillating voltage U is the subject for electronic acquisition system to measure as a sample response.

Arbitrary net magnetization vector  $\vec{M}$  tends to evolve into its equilibrium state  $\vec{M}^{eq}$  due to relaxation phenomena. These include transverse ( $T_2$ ) and longitudinal ( $T_1$ ) terms. Transverse (or spin-spin) relaxation affects  $M_x$  and  $M_y$  components and comes as an exponential multiplier as follows [59]:

$$M_x(t) = (M_x \cos \omega_0 t - M_y \sin \omega_0 t) \exp\left(-\frac{t}{T_2}\right) \quad 3.1-11$$

$$M_y(t) = (M_x \sin \omega_0 t + M_y \cos \omega_0 t) \exp\left(-\frac{t}{T_2}\right) \quad 3.1-12$$

Longitudinal (or spin-lattice) relaxation affects  $M_z$  component and can be presented as follows [59]:

$$M_z(t) = (M_z - 1) \exp\left(-\frac{t}{T_1}\right) + 1 \quad 3.1-13$$

A single pulse experiment can be presented in terms of a self-explanatory diagram (Fig. 3.2):

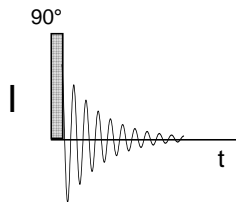


Fig. 3.2 A pulse scheme for a single pulse experiment.

Here the vertical bar presets a  $90^\circ$  or  $\pi/2$  pulse generating transverse magnetization and the curve indicates the signal acquisition.

### 3.2. Essential SSNMR interactions and Magic Angle sample Spinning

*Dipolar coupling* of two nuclei arises as a second term in multipoles' interaction deconvolution and therefore can be written as [60]:

$$U = \frac{\mu_0}{4\pi} \left( \frac{\vec{\mu}_1 \vec{\mu}_2}{r^3} - 3 \frac{(\vec{\mu}_1 \vec{r})(\vec{\mu}_2 \vec{r})}{r^5} \right) \quad 3.2-1$$

where  $\vec{\mu}_i$  are point magnetic dipoles and  $\vec{r}$  is the vector connecting the dipoles. Since  $\hat{\mu} = \gamma \hat{I}$  in the case of nuclear spins the expression can be rewritten as interaction Hamiltonian [60]:

$$\hat{H}_{DC} = -\frac{\mu_0}{4\pi} \frac{\gamma_1 \gamma_2}{r^3} (A + B + C + D + E + F) \quad 3.2-2$$

where [60]:

$$\begin{aligned} A &= \hat{I}_z^1 \hat{I}_z^2 (3 \cos^2 \theta - 1) \\ B &= -\frac{1}{4} [\hat{I}_+^1 \hat{I}_-^2 + \hat{I}_-^1 \hat{I}_+^2] (3 \cos^2 \theta - 1) \\ C &= \frac{3}{2} [\hat{I}_z^1 \hat{I}_+^2 + \hat{I}_+^1 \hat{I}_z^2] \sin \theta \cos \theta \exp(-i\varphi) \\ D &= \frac{3}{2} [\hat{I}_z^1 \hat{I}_-^2 + \hat{I}_-^1 \hat{I}_z^2] \sin \theta \cos \theta \exp(+i\varphi) \\ E &= \frac{3}{4} [\hat{I}_+^1 \hat{I}_+^2] \sin^2 \theta \exp(-2i\varphi) \\ F &= \frac{3}{4} [\hat{I}_-^1 \hat{I}_-^2] \sin^2 \theta \exp(+2i\varphi) \end{aligned} \quad 3.2-3$$

Here  $\hat{I}_\pm$  are the raising and lowering operators defined elsewhere[59],  $\theta$  is an angle between  $\vec{r}$  and the z-axis and  $\varphi$  is the corresponding azimuthal angle. Since the strength of the interaction depends on the internuclear distance and molecular orientation it can serve as structural information source which is extensively used in a number of NMR experiments (Cross Polarization, REDOR, HETCOR etc. explained further).

Two cases have to be mentioned: *homonuclear* and *heteronuclear* dipolar couplings. In homonuclear dipolar coupling case it is possible to simplify expression 3.2-2 to the following view [60]:

$$\hat{H}_{\text{hom}DC} = -d \frac{1}{2} (3 \cos^2 \theta - 1) \left[ 3 \hat{I}_z^1 \hat{I}_z^2 - \hat{I}^1 \hat{I}^2 \right] \quad 3.2-4$$

where the bar over the Hamiltonian denotes the first order average in the rotating

frame and  $d$  is the dipolar coupling constant  $d = -\left(\frac{\mu_0}{4\pi}\right) \frac{1}{r^3} \gamma_1 \gamma_2$ . Consider now a two-

spin system with dipolar coupled spins. Every spin pair will then be in one of 4 possible energy states:  $\alpha\alpha$ ,  $\alpha\beta$ ,  $\beta\alpha$  or  $\beta\beta$ . The effect of dipolar coupling on such a system consists of two parts:

the energy levels shift due to  $\hat{I}_z^1 \hat{I}_z^2$  component

mixing of  $\alpha\beta$  and  $\beta\alpha$  wave functions due to  $[\hat{I}_+^1 \hat{I}_-^2 + \hat{I}_-^1 \hat{I}_+^2]$  spin operator term which indirectly comes in the expression 3.2-4.

In general, for a many-spin system, the second term will mix degenerate Zeeman levels, resulting in a huge range of transition frequencies in the NMR spectrum of such a spin system and this results in very broad lines. Homonuclear dipolar coupling is an essential phenomenon for spin-diffusion experiments, where due to the “flip-flop” interactions ( $[\hat{I}_+^1 \hat{I}_-^2 + \hat{I}_-^1 \hat{I}_+^2]$ ) polarization dissipates from one magnetic domain to the others.

For the case of heteronuclear dipolar coupling, expression 3.2-4 can be further simplified by accounting the difference in Larmor frequencies for different isotopes.

This leads to the expression [60]:

$$\hat{H}_{\text{het}DC} = -d (3 \cos^2 \theta - 1) \hat{I}_z^1 \hat{I}_z^2 \quad 3.2-5$$

In biological samples heteronuclear dipolar coupling plays an important role both in line broadening and in polarization transfer to rare spins.

*Chemical shift* effect arises due to electrons' ability to generate secondary magnetic field as a response to the external magnetic field. The total magnetic field at the nucleus therefore changes and consequently changes the resonance frequency  $\omega_0$ . The effect can be described in secular approximation by the following interaction Hamiltonian [59]:

$$\hat{H}_{CS} = -\gamma \hat{I}_z \delta_{zz} B_0 \quad 3.2-6$$

where  $\delta_{zz}$  is the component of *chemical shift tensor*  $\delta$ . The tensor depends on the orientation of the molecule with respect to the magnetic field  $B_0$  and also on the location of the nuclear spin within the molecule. Three principal values of the chemical shift tensor are frequently expressed as the isotropic value  $\delta_{iso}$ , the anisotropy  $\delta_{aniso}$  and the asymmetry  $\eta$  [59]:

$$\begin{aligned} \delta_{iso} &= \frac{1}{3}(\delta_{xx} + \delta_{yy} + \delta_{zz}) \\ \delta_{aniso} &= \delta_{zz} - \delta_{iso} \\ \eta &= \frac{\delta_{xx} - \delta_{yy}}{\delta_{aniso}} \end{aligned} \quad 3.2-7$$

The contribution to the frequency of the observed NMR signal from the chemical shift interaction is [59]:

$$\begin{aligned} \omega_{cs}(\theta, \varphi) &= \omega_0 - (\delta_{xx} \sin^2 \theta \cos^2 \varphi + \delta_{yy} \sin^2 \theta \sin^2 \varphi + \delta_{zz} \cos^2 \theta) \\ or \\ \omega_{cs}(\theta, \varphi) &= -\omega_0 \delta_{iso} - \frac{1}{2} \omega_0 \delta_{aniso} [3 \cos^2 \theta - 1 + \eta \sin^2 \theta \cos 2\varphi] \end{aligned} \quad 3.2-8$$

The total spectral frequency in absolute units is the Larmor frequency plus the chemical shift contribution. A reference substance is used and frequencies of signals are measured relative to a specific line in the spectrum of the substance. The shift values are usually given in parts per million – ppm, according to [59]:

$$\delta = \frac{\delta_{iso} - \delta_{ref}}{\delta_{ref}} \quad 3.2-9$$

In static powder solids, the anisotropic part usually leads to enormous line broadening and changing of line shape (see Fig. 3.3).

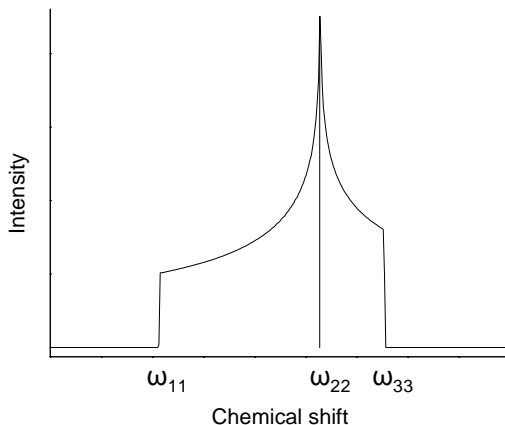


Fig. 3.3 Static powder Solid-State NMR typical line shape. The frequencies  $\omega_{ij}$  correspond to the principal values of the chemical shift tensor.

*Magic Angle Spinning* (MAS) is used routinely in the vast majority of solid-state NMR experiments, where its primary task is to remove the effects of chemical shift anisotropy and to assist in the removal of heteronuclear dipolar coupling effects. If we spin a sample about an axis inclined at an angle  $\theta_R$  to the applied field, then  $\theta$ , the angle between  $B_0$  and principal z-axis of chemical shift tensor (Fig. 3.4), varies with time as the molecule rotates with the sample. If  $\theta_R=54.74^\circ$  (magic angle) then the average of the orientation dependence can be found as in 3.2-10 [60].

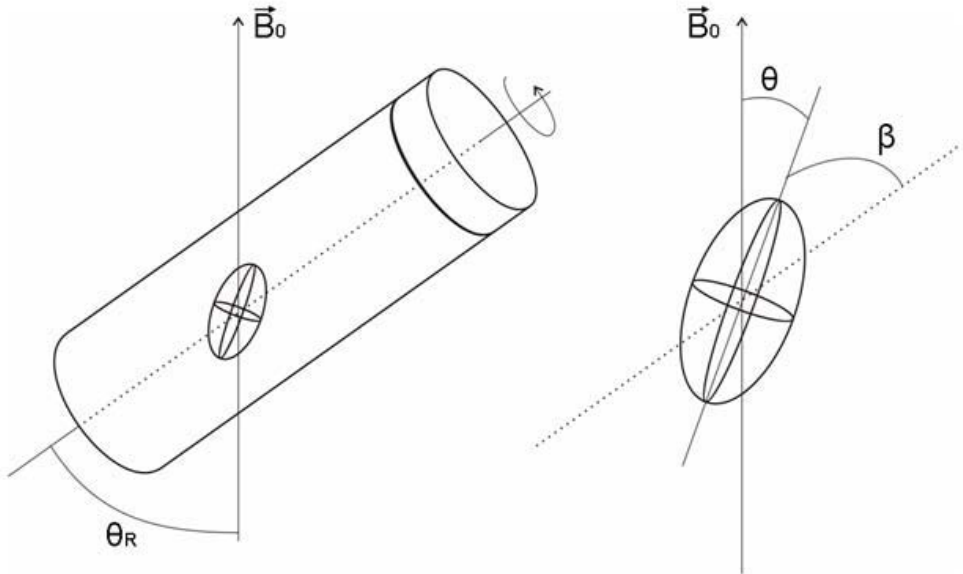


Fig. 3.4 MAS experiment. Left – a cylindrical rotor with chemical shift tensor indicated. Right – position of the tensor relatively to magnetic field and rotation axis.  $\theta_R$  – magic angle of  $54.74^\circ$ ,  $\theta$  is the angle between applied magnetic field and the principal z-axis of the chemical shift tensor and  $\beta$  is the angle between z-axis of the chemical shift tensor and rotation axis.

$$\omega(\alpha, \beta, \gamma; t) = -\omega_0(\delta_{iso} + [A_1 \cos(\omega_R t + \gamma) + B_1 \sin(\omega_R t + \gamma)] + [A_2 \cos(2\omega_R t + 2\gamma) + B_2 \sin(2\omega_R t + 2\gamma)]) \quad 3.2-10$$

with  $A_1$ ,  $A_2$ ,  $B_1$  and  $B_2$  defined elsewhere [60].

The first term is the isotropic term. The remaining terms oscillate at frequencies  $\omega_R$  and  $2\omega_R$  respectively. When the spinning rate is much greater than the chemical shift anisotropy these terms have a negligible effect on the NMR spectrum. In the case of  $\omega_R \leq \delta_{aniso}$  these terms create spinning sidebands which come into the spectrum as signals “echoes” spaced by intervals equal to  $\omega_R$  (see Fig. 3.5).

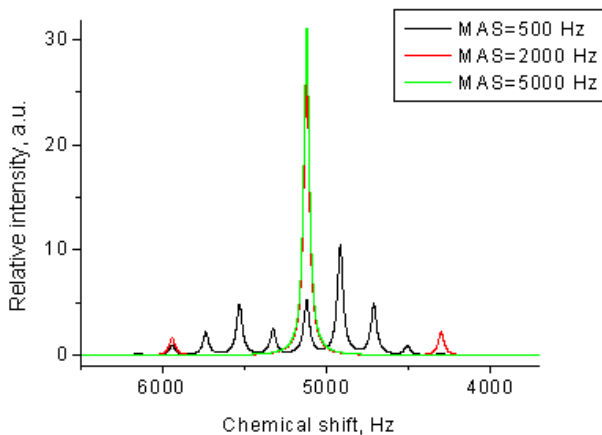


Fig. 3.5 Simulated NMR Single Pulse spectra with different Magic Angle Spinning speed.

In the case of dipolar couplings (homo- or heteronuclear) the term  $(3\cos^2\theta-1)$  averages out by fast ( $\omega_R \gg d$ ) sample rotation [60]:

$$\langle 3\cos^2\theta - 1 \rangle = \frac{1}{2}(3\cos^2\theta_R - 1)(3\cos^2\beta - 1) \quad 3.2-11$$

and in case of magic angle spinning with  $\theta_R=54.74^\circ$  the term completely averages out thus narrowing the spectrum.

### 3.3. Essential techniques for solid-state NMR

#### Spin-Echo

Inhomogeneous line broadening occurs due to magnetic field inhomogeneity and samples own magnetic susceptibility. Spin-Echo experiment helps to overcome the problems and is used for  $T_2$  relaxation measurements, for separation of signals with different  $T_2$ , etc. The corresponding pulse sequence is presented in Fig. 3.6

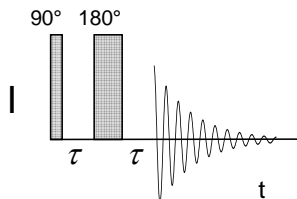


Fig. 3.6 Spin-Echo pulse sequence

During waiting period  $\tau$  a signal tends to dephase in the  $xy$ -plane.  $180^\circ$  pulse applied revolves the spin state of the system and it evolves back during the second  $\tau$ -period and becomes refocused at time  $2\tau$ . The process can be presented in terms of signals phase evolution:

$$\varphi_{xy} \xrightarrow{\hat{H}_{in.hom}} (\varphi_{xy} + \Delta\varphi_{xy}) \xrightarrow{\hat{H}_{pulse}} (\varphi_{xy} - \Delta\varphi_{xy}) \xrightarrow{\hat{H}_{in.hom}} \varphi_{xy} \quad 3.3-1$$

where  $\varphi_{xy}$  is the signal phase after the  $90^\circ$  pulse and  $\Delta\varphi_{xy}$  is the phase shift due to local magnetic field inhomogeneity. If  $\tau = NT_R$  ( $N$  full rotor cycles) then the experiment is called *Rotor Synchronized Echo* (RSECHO).

If waiting period  $\tau$  is long enough (i.e. longer than several  $T_2$ ) then corresponding signals are no longer detectable. This phenomenon is used further as echo-filtering in Echo-CP-REDOR type sequences (explained further in this chapter).

### Cross polarization

Rare spins, such as  $^{13}\text{C}$  (natural abundance  $^{13}\text{C} = 1\%$ ), and spins with extremely long  $T_1$  relaxation are usually measured using polarization transfer techniques. In this case transverse magnetization is firstly generated on abundant spins, such as protons, and then the polarization transfers to the rare spins by means of dipolar coupling. After magic angle spinning, *cross polarization* is one of the most widely used techniques in solid-state NMR. The technique uses simultaneous irradiation of two spin lock pulses on two channels (e.g.  $^1\text{H}$  and  $^{13}\text{C}$ ). Since the duration of both pulses has to be equal they are usually referred to as *contact pulse*. Corresponding RF magnetic fields must obey the Hartmann-Hahn condition [4]:

$$\gamma_H B_{RF}^H = \gamma_C B_{RF}^C \quad 3.3-2$$

The proton-carbon interaction Hamiltonian of a system with several protons coupled to a diluted  $^{13}\text{C}$  nuclei after some reorganization can be written as [61]:

$$\begin{aligned} \hat{H}_{HC}^* = & -\sum_i C_i^{HC} \left[ \left( \sum_i \hat{I}_{iz}^H \hat{I}_z^C + \sum_i \hat{I}_{iy}^H \hat{I}_y^C \right) \cos(\omega_1^H - \omega_1^C)t \right. \\ & \left. + \left( \sum_i \hat{I}_{iz}^H \hat{I}_y^C + \sum_i \hat{I}_{iy}^H \hat{I}_z^C \right) \sin(\omega_1^H - \omega_1^C)t \right]; \quad 3.3-3 \\ C_i^{HC} = & \frac{\mu_0 \gamma_H \gamma_C}{4\pi} \frac{1}{r_i^3} \frac{1}{2} (3 \cos^2 \theta_i - 1) \end{aligned}$$

where asterisk means toggling frame [60] and  $\omega_\alpha^\beta$  are nutation frequencies. The sum over  $i$  accounts all protons coupled to the carbon nucleus. When  $\omega_1^H \neq \omega_1^C$ , the



interaction Hamiltonian has little effect on the spin system as it contains oscillating terms which roughly average to zero over the pulse length (usually from tens of microseconds to tens of milliseconds). However, when  $\omega_1^H \cong \omega_1^C$  (the Hartmann-Hahn condition), the oscillating terms disappear and the interaction causes a double resonance effect between  $^1\text{H}$  and  $^{13}\text{C}$  spins. The  $\hat{I}_{by}^H \hat{I}_y^C$  term contains  $\hat{I}_{i+}^H \hat{I}_{-}^C$  and  $\hat{I}_{i-}^H \hat{I}_{+}^C$  terms which cause magnetization transfer between the spins.

Magic angle spinning introduces time dependence into the interaction. In this case  $C_i^{HC}$  term start oscillating on  $\pm\omega_R$  and  $\pm 2\omega_R$  and if  $\omega_R \gg \frac{\mu_0 \gamma_H \gamma_C}{4\pi r_i^3}$  the net cross polarization term in the Hamiltonian averages to zero.

The Hartmann-Hahn condition under magic angle spinning becomes  $\omega_1^H - \omega_1^C = \pm\omega_R$  - the so-called sideband match conditions.  $^{13}\text{C}$  NMR spectra of biological samples cover the range of about 200 ppm, thus different peaks have different match conditions leading to signals losses. To broaden the Hartmann-Hahn match conditions, a ramp is used on one of the channels as shown in Fig. 3.7.

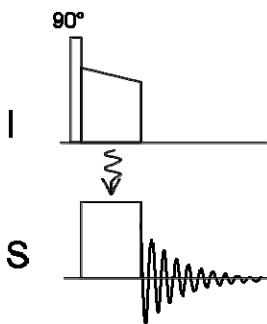


Fig. 3.7 Ramped cross polarization pulse sequence. Abundant nuclei are on channel I and the rare ones – on channel S.

To suppress spin diffusion processes between the abundant nuclei during the contact pulse, a Frequency Switched Lee-Goldburg Cross Polarization [62] (FSLG-CP) technique can be utilized.

Polarization transfer to the rare nuclei can be characterised by a CP build-up curve. Differences in number of neighbouring I (abundant) spins and spatial proximity to them define how fast S (rare) spins will acquire polarization during the contact pulse. Following the signal growth on S channel by making a row of experiments with increasing spin lock pulse duration it is possible to separate fast and slow-growing components of the signal. In the case of cross polarization between dilute and abundant nuclei, signal growth of former ones can be characterised with two time constants [61]:

$$I(t) = \frac{I_0}{1 - T_C / T_{1\rho}} \left( \exp(-t / T_{1\rho}) - \exp(-t / T_C) \right) \quad 3.3-4$$

where  $T_{1\rho}$  is an abundant nuclei transverse relaxation time during the spin lock pulse and  $T_C$  is rare nuclei build-up rate. Here an additional assumption was made that spin-lattice relaxation rate of diluted spins is much bigger compared to  $1/T_C$ . This is quite usual for most of  $^1\text{H}$ - $^{13}\text{C}$  and  $^1\text{H}$ - $^{31}\text{P}$  cross polarization experiments. In the case of  $^1\text{H}$ - $^{31}\text{P}$  cross polarization in hydroxyapatite crystallites (they are characterised in chapters 4 and 5) it is more reasonable to use another presentation of the build-up curve accounting nearest protons for polarization transfer and the rest of the protons as a spin bath. In general, for isolated  $\text{SI}_n$  clusters in a powder sample under MAS but without extensive molecular motion the following holds [61]:

$$I(t) = I_0 \exp(-t / T_{1\rho}) \left[ 1 - \frac{1}{n+1} \exp(-t / T_{df}) \right] \quad 3.3-5$$

Here  $1/T_{df}$  is a typical spin diffusion rate between protons and phosphorus atoms and  $n$  is the number of I spins in the  $\text{SI}_n$  cluster. Typical cross polarization build-up behaviour in a two-spin system is presented in Fig. 3.8. Dipolar coupling constant value can be calculated by fitting the experimental results.

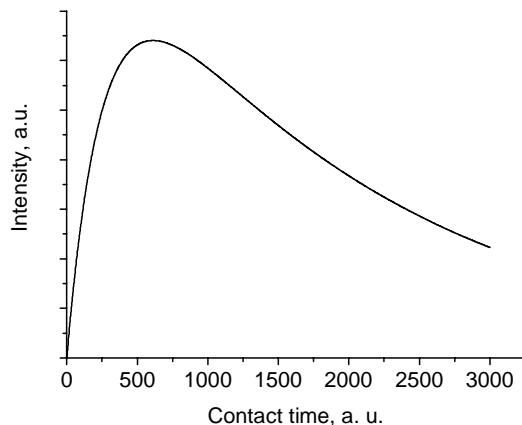


Fig. 3.8 A sketch of a CP build-up curve.

## REDOR

Measuring internuclear distances provides important structural information for all branches of chemical sciences [6]. *Rotational Echo Double Resonance* (REDOR) is a versatile and straightforward experiment for such purposes. Its important feature is that dipolar coupling constants can be obtained in a simple manner without the need to know the chemical shift or any other interaction. The experiment basically includes two series of  $\pi$  pulses on dephasing channel separated by a refocusing  $\pi$  pulse on the observed channel spaced by a half rotor period delays (Fig. 3.9).

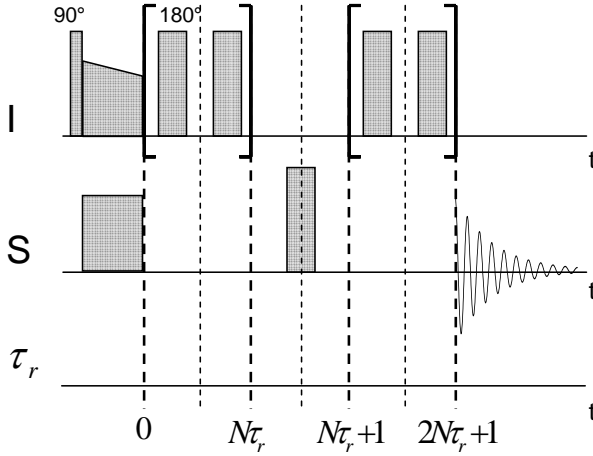


Fig. 3.9 REDOR pulse sequence with prior CP step.

The heteronuclear dipolar coupling interaction is described by expression 3.2-5. The effect of  $180^\circ$  pulse on I (or S) spins is equal to sign reversal of the interaction Hamiltonian [60]:

$$\hat{H}_{hetDC} = -d(3\cos^2\theta - 1)\hat{I}_z^1(-\hat{I}_z^2) = d(3\cos^2\theta - 1)\hat{I}_z^1\hat{I}_z^2 = -\hat{H}_{hetDC} \quad 3.3-6$$

and integrated over a rotor period [60]:

$$\hat{H}_{hetDC} = \frac{1}{\tau_R} \left( \int_0^{\tau_R/2} \hat{H}_{DC}(t) dt - \int_{\tau_R/2}^{\tau_R} \hat{H}_{DC}(t) dt \right) \quad 3.3-7$$

becomes nonzero, thus “reintroducing” heteronuclear dipolar coupling in an MAS experiment. The  $180^\circ$  pulse on S channel is necessary to refocus chemical shifts offset and acts as in RSECHO sequence.

The signal is measured as a ratio of two experiments: with  $180^\circ$  pulses on I channel (dephasing pulses) on (S) and off ( $S_0$ ). In the first case additional dephasing occurs compared to the second case due to the reintroduced dipolar coupling. For two spin system this can be presented as follows [60]:

$$\frac{S(N\tau_R)}{S_0(N\tau_R)} = \frac{1}{2\pi} \int_0^{\pi/2} \int_0^{2\pi} \cos(N\Delta\Phi(\beta, \gamma, \tau_R)) \sin\beta d\beta d\gamma \quad 3.3-8$$

where

$$\Delta\Phi(\beta, \gamma, \tau_R) = \pm 2\sqrt{2} \frac{d}{\omega_R} \sin 2\beta \sin \gamma \quad 3.3-9$$

is additional phase acquired due to the dipolar coupling interaction and  $\beta$ ,  $\gamma$  describe the molecular orientation relative to the external magnetic field. REDOR curve for a two-spin system is described by expression 3.3-10 [63] and is plotted in Fig. 3.10.

$$\frac{S_0(N\tau_R) - S(N\tau_R)}{S_0(N\tau_R)} = \frac{\Delta S}{S_0} = 1 - \frac{\sqrt{2}\pi}{4} J_{1/4}(\sqrt{2}ND\tau_r) J_{-1/4}(\sqrt{2}ND\tau_r) \quad 3.3-10$$

In the case of sample with only IS spin pairs it is possible to perform a so-called REDOR transform [63] and to obtain dipolar coupling constants directly from the experimental data. Also initial behaviour of the REDOR curve can be approximated by a parabolic function [64]:

$$\frac{\Delta S(N\tau_R)}{S_0(N\tau_R)} \cong K(Nd\tau_R)^2 \quad 3.3-11$$

with  $K \approx 1.066$ . This allows fast approximating of a mean I-S distance.

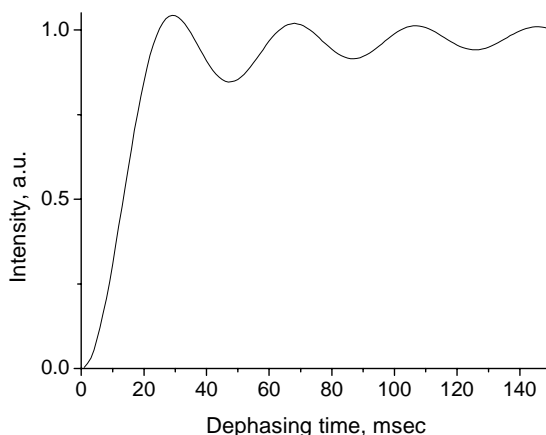
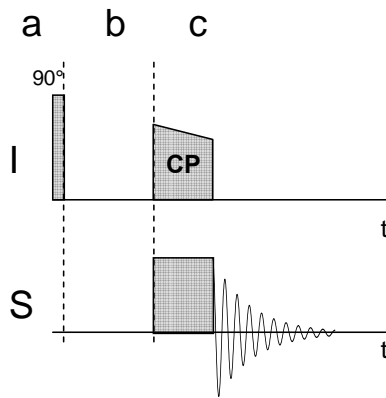


Fig. 3.10 Typical REDOR dephasing curve for an isolated two-spin system.

## 2D Correlation experiments

In 2D Fourier Transformed Spectroscopy (FTS), the 2D spectrum is obtained by Fourier transforming a signal  $S(t_1, t_2)$  which depends on two independent time variables  $t_1$  and  $t_2$  [5]. The three phases which are characteristic for all 2D experiments are: preparation period, evolution period and detection period. During the first preparation period, the system is prepared in a suitable initial state. During the evolution period the system evolves under the influence of the

interactions and assumes at the end of this interval a particular state which depends on the interactions involved and on the elapsed time  $t_1$ . During the detection period the transverse magnetization is acquired as a function of  $t_2$ . A series of experiments with increasing  $t_1$  is recorded and stored as a 2D spectrum. 2D experiments used in the present work can be subdivided into two groups by the correlation type they observe: homonuclear and heteronuclear. The 2D spin diffusion experiment, for example, is an extension of the 1D version that correlates homonuclear signals between themselves on the basis of homonuclear coupling (Fig. 3.12). The Heteronuclear Correlation (HETCOR) experiment correlates the I spins with S spins that are in close proximity (Fig. 3.11).



*Fig. 3.11 Sample 2D heteronuclear correlation experiment. Three intervals are denoted: a – preparation period; b – evolution period, I spins evolve under the interactions involved; c – detection period, cross polarization utilized to transfer polarization to the S spins.*

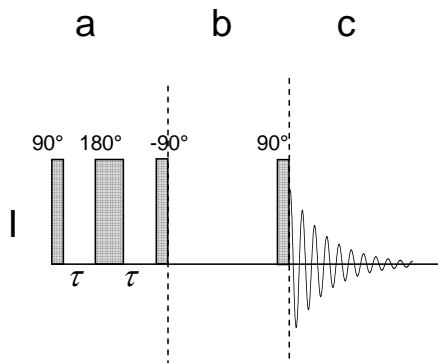


Fig. 3.12 Sample homonuclear 2D spin diffusion experiment. Three intervals are denoted: *a* – preparation period, echo sequence used for signals with long  $T_2$  selection; *b* – evolution period, spin information floats from the selected spins to other parts; *c* – detection period.

These 2D experiments are designed to fulfil the following tasks:

- to separate different interactions (e.g. shifts and couplings) in orthogonal frequency dimensions, with the purpose of resolving 1D spectra by spreading overlapping resonances in a second dimension
- to correlate chemical shifts of coupled spins
- to study dynamic processes such as chemical exchange, cross-relaxation and spin-diffusion [65]

### Decoupling techniques

Achieving high spectral resolution is an important prerequisite for the application of solid-state NMR to biological molecules [66]. Increasing the resolution allows to resolve a larger number of resonances. Heteronuclear spin decoupling techniques are widely used for this purpose. Most common decoupling sequences are continuous wave (CW) and two-pulse phase-modulated decoupling (TPPM) [67]. Continuous high-power irradiation on one-spin species eliminates the heteronuclear couplings to the other spin species, regardless of the states of the magnetization [3]. This happens because the average of the dipolar Hamiltonian precesses over RF field and vanishes over integer precession periods and tends to zero for long irradiation times.

Two-pulse phase-modulated decoupling [67] consists of pulses with a flip angle  $\beta_p$  and alternating phases  $\pm\varphi/2$ . The optimum value for the flip angle is typically near  $180^\circ$ . The optimum value of the phase  $\varphi$  can vary over quite a large range and is usually between  $10^\circ$  and  $50^\circ$ . Both the flip angle and the phase vary as a function of the spinning speed, the spectrometer, the probe and the sample.

#### 3.4. Additional Solid-State NMR techniques

Due to the complexity of biomaterials any attempt to characterize their structure meets with a lot of difficulties making the investigation a state-of-the-art task. Absence of long-range order, a great number of organic and inorganic compounds tightly bounded together and structural changes through a sample are the main problems one has to keep in mind when planning an experiment. Conventional NMR spectra of such complicated materials are, of course, very overloaded with signals and the question is how to get information of interest? One way is to use methods for signal selection. Selection can be based on several phenomena: different dipolar coupling strength, relaxation effects, etc. Another opportunity is to combine different approaches in order to have a picture from the several points of view. Further, some experiments are described that have a great importance for biomaterials characterization.

##### **Echo-CP-REDOR (ECR) and Echo-REDOR-CP (ERC)**

A group of experiments are proposed and applied for structural characterization of bone-like biomaterials. The number of nearest neighbours and their distances are crucial for mineral phase of bone characterization. This characterization is performed using REDOR technique. Unfortunately, the hydroxyapatite line in bone samples is relatively broad and organic matrix signals almost overlay it. Echo selection ( $T_2$  filter) performs almost exclusive selection of hydroxyapatite signal suppressing organic matrix signals due to their short transverse relaxation time. Further, the experiment can be carried out in two ways: phosphorus nuclei dephased by protons or protons dephased by phosphorus. In the first case, polarization is transferred to  $^{31}\text{P}$  channel and then phosphorus is dephased by  $180^\circ$  pulses on proton channel. This allows only the dipolar dephasing behaviour of the



phosphorus nuclei that are in spatial proximity from the selected protons to be measured. These are the nuclei in the core of the mineral crystallites. Information acquired in such a way tells us about proton surrounding of the phosphorus nuclei. In the second case, protons are dephased by phosphorus and then the rest of polarization is transferred to  $^{31}\text{P}$  channel for acquisition. Information acquired in such a way tells us about phosphorus surrounding of the pre-selected protons seen from phosphorus side.

Note, that there is no difference for REDOR on which channel to put dephasing  $180^\circ$  pulses [6]. The only reason to decide whether it is worth leaving dephasing pulses on the original channel or to change to another one is spectrum width, since if there is only one narrow component, it can be refocused easier than if there are many broad components lasting over a great spectral region.

Corresponding pulse sequences are presented on Fig. 3.13

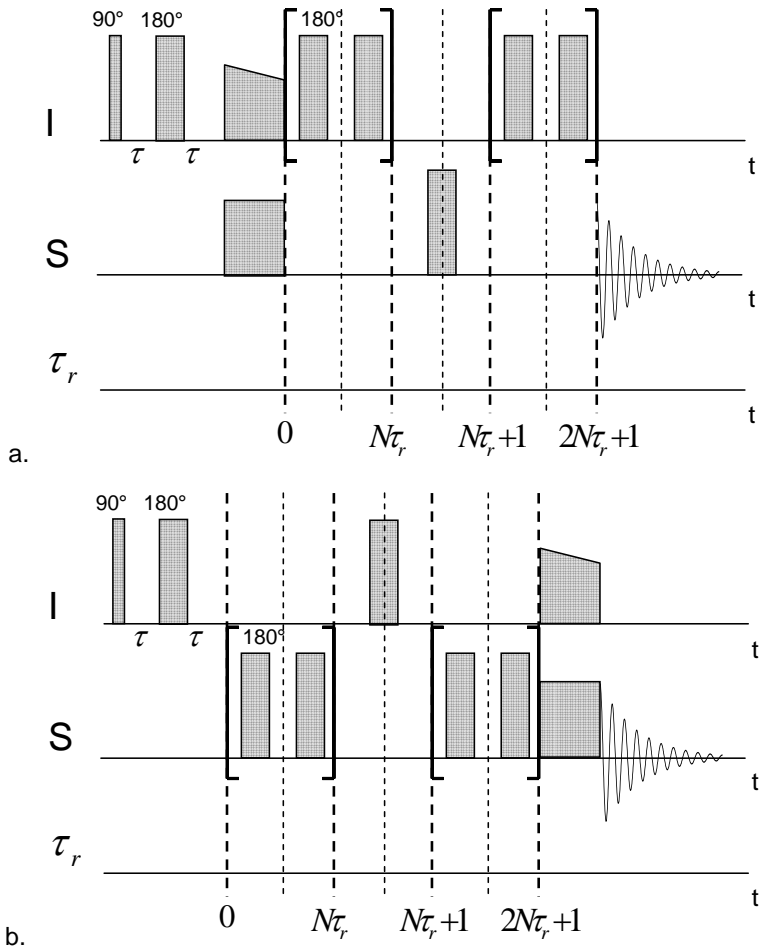


Fig. 3.13 Echo-CP-REDOR (a) and Echo-REDOR-CP (b) pulse sequences.

## 4. Direct detection of the indirect dimension of a standard 2D HETCOR

Polarization transfer methods from abundant to diluted spins exploiting heteronuclear dipolar couplings (e.g. continuous wave cross polarization (CP) [4], recoupled polarization transfer (REPT) [68]) are very important in NMR spectroscopy. Originally developed for the enhancement of the sensitivity of detection of diluted spins ( $^{13}\text{C}$ ,  $^{29}\text{Si}$ ,  $^{15}\text{N}$ ) polarization transfer is the most important step for various two-dimensional (2D) NMR experiments [65; 69]. In heteronuclear correlation spectroscopy experiments, the spatial proximity of heteronuclei, like  $^1\text{H}$  and  $^{13}\text{C}$ , can be probed. If heteronuclear  $J$ -couplings are used in the transfer step [70] solely chemically bonded species are detected, such as CH, CH<sub>2</sub> or CH<sub>3</sub> groups. Such experiments are essential for the spectral assignment of  $^1\text{H}$  resonances in complex materials, such as cellulose, and the determination of their chemical shifts along the  $^{13}\text{C}$  peaks, because the  $^1\text{H}$  spectral resolution is rather poor [71]. Similarly,  $J$ -couplings through Al-O-P bonds can be used to verify such bonding scenarios in solids [72; 73].

If heteronuclear dipole interactions are used for the polarization transfer step spatial proximities between the nuclei can be exploited. A chemical bond is not required. Such experiments are also very useful, particularly if spatial proximities of molecules to specific structural units are to be probed. One question in natural or synthetic biomaterials such as bone or nanocrystalline hydroxyapatite or plasma sprayed coatings is, e.g. whether or not water molecules are close to phosphate units in the structure or if hydroxyl units exist in the phosphate network [38; 74; 75]. For solving such structural problems, usually 2D heteronuclear correlation experiments are required. Depending on the I spin line widths, such experiments can become time consuming. The narrow OH<sup>-</sup> signal in hydroxyapatite or even bone is a typical example for biomaterials. Therefore, a large number of  $t_1$  increments must be used making the measurements very long.

In this chapter a simple alternative for the full 2D experiment is presented. Rather than detecting the transferred I spin magnetization indirectly through the S spins, the transferred polarization part is acquired directly in two scans (“two-step” experiment) of an ordinary CP experiment (one without and another with the S spin

lock pulse on). As a result, the transferred I spin signal is recovered and used for spectroscopy. In the following the experiment is explained and several very useful applications of this simple trick will be shown. For example, it is possible to acquire the F1 sum projection of a 2D experiment in just two scans resulting in a significant time saving because there is no need to increment the  $t_1$  time domain. Another example concerns phosphate-containing biomaterials, where  $^1\text{H}$ - $^{31}\text{P}$  CP curves (for example to distinguish  $\text{HPO}_4^{2-}$  units from  $\text{PO}_4^{3-}$  groups with water or hydroxyl ions nearby) can be measured this way in a 1D fashion. Furthermore, interatomic distances can be determined from such CP transfer curves e.g. [76], and the proposed experiment circumvents the necessary 2D measurement whenever the  $^1\text{H}$  spectral resolution is sufficient, e.g. using very high MAS rotation frequencies. Finally it will be demonstrated that organic-inorganic interfaces can be studied in detail by blanking unwanted (bulk) signals such that the surface sites can be viewed.

### 4.1. Materials and methods

Described NMR experiments have been carried out using a nanocrystalline hydroxyapatite sample which was prepared at the University of Duisburg-Essen (M. Epple group) by chemical precipitation [77]. This hydroxyapatite sample is  $\text{Ca}^{2+}$  deficient, having a Ca/P ratio of 1.52 instead of 1.667 for stoichiometric hydroxyapatite [78]. The mean crystal size is typically  $40 \times 10 \times 10$  nm.

The o-phospho-L-serine sample is a commercial product (Fluka).

The basic idea of this experiment is to directly use the part of the I spin magnetization that is lost during the polarization transfer step (mostly CP) to the S spins where it is detected indirectly in the  $F_1$  dimension of a full 2D experiment. The principle is summarized in Fig. 4.1 and requires two subsequent steps: The first experiment does not involve a polarization transfer, which is done with the CP pulse on the S channel switched off, so the spin-locked I spin magnetization remains and generates a signal. In the second experiment the CP condition is fulfilled, and, therefore, the I spin signal is somewhat reduced due to the magnetization transfer process to the S spins. By taking the difference of both signals the desired I spin signal is recovered. The idea to use this "lost" polarization

part for spectroscopy seems unusual. However, as will be shown below, it offers some interesting possibilities.

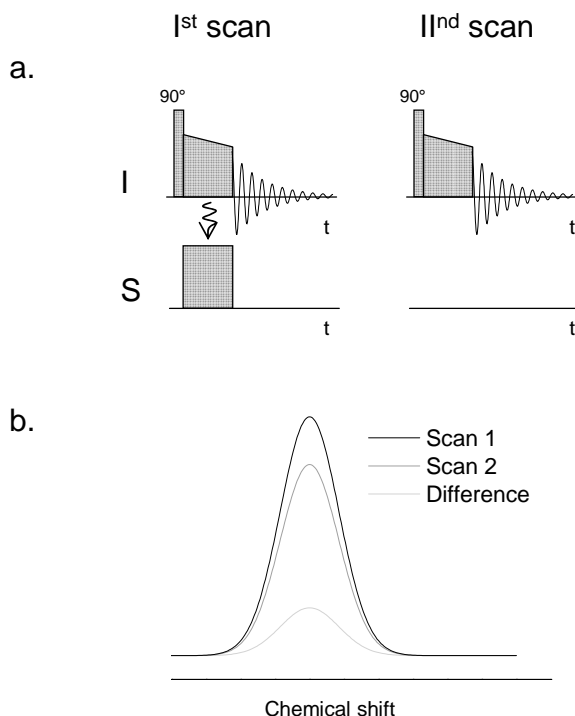


Fig. 4.1 a) Two consecutive scans of the “two-step” experiment and b) difference spectrum presents the losses of *I*-spin magnetization.

## 4.2. Results and Discussion

### Fast acquisition of the F1 sum projection of a 2D NMR experiment with two scans

The nanocrystalline hydroxyapatite has been investigated in detail by  $^{31}\text{P}$  and  $^1\text{H}$  NMR [79] showing that this  $\text{Ca}^{2+}$  deficient hydroxyapatite consists of a crystalline core containing 50% of the total phosphate content with stoichiometric hydroxyapatite composition, whereas the other 50% of “phosphate” form an about 1nm-thick surface layer with  $\text{PO}_4^{3-}$  and  $\text{HPO}_4^{2-}$  units. This surface layer is amorphous and does not contain any hydroxyapatite structural motifs (no  $\text{OH}^-$  !),

but contains crystal water molecules in its structure. From the NMR data an overall Ca/P ratio of 1.51 was determined thus explaining for the first time the  $\text{Ca}^{2+}$  deficiency on a structural basis.

The  $^1\text{H}$ - $^{31}\text{P}$  heteronuclear correlation spectrum of the nanocrystalline hydroxyapatite sample is shown in Fig. 4.2. The CP contact time was 2 ms.

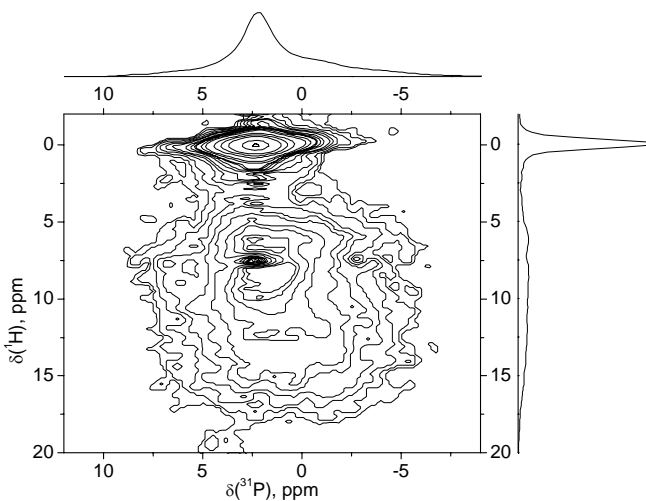


Fig. 4.2  $2\text{D } ^1\text{H}\text{-}^{31}\text{P}$  heteronuclear correlation experiment of nanocrystalline hydroxyapatite with the F2 and F1 sum projections shown on top and right, respectively.

This 2D spectrum consists basically of two peaks. The narrow correlation signal at 0 ppm ( $^1\text{H}$ ) and 2.3 ppm ( $^{31}\text{P}$ ) is the typical signature for stoichiometric hydroxyapatite (discussed in detail in chapter 5). This signal comes from the crystalline bulk of the nanocrystals. The second correlation peak is caused by the molecular structure of the amorphous surface layer and shows a broad  $^1\text{H}$  line shape between 3-17 ppm. Water molecules (around 5 ppm) and the protons of  $\text{HPO}_4^{2-}$  groups (up to 17 ppm) compose this signal. Simultaneously, the  $^{31}\text{P}$  correlation peak of these  $\text{HPO}_4^{2-}$  and additional  $\text{PO}_4^{3-}$  units is much broader than the hydroxyapatite  $^{31}\text{P}$  signal thus verifying the amorphous nature of the surface layer as can be seen in the F2 sum projection on top.

By definition the  $^1\text{H}$  spectrum using the recovered  $^1\text{H}$  signal using the two-scan method is equivalent to the F1 sum projection of the indirect dimension of the 2D heteronuclear experiment at the same CP contact time. Both spectra are shown in Fig. 4.3 for comparison. The main advantage is that no  $t_1$  increment is needed. Hence,  $^1\text{H}$  spectral resolution is not a problem which otherwise would increase the required number of  $t_1$  increment steps, thus saving a considerable amount of time. The time gain is about 16 in this example. Both spectra are equivalent; the slight deviations are presumably caused by the fact that there is no receiver deadtime problem for the indirect dimension in the 2D spectrum, whereas the direct acquisition of the  $^1\text{H}$  signals may suffer from the delayed signal acquisition (16  $\mu\text{s}$  in this example).

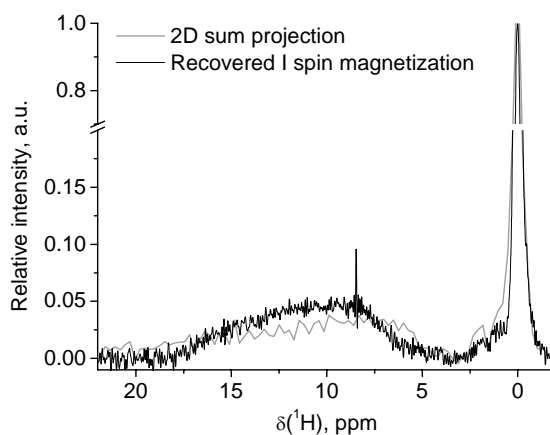


Fig. 4.3 Comparison of the F1 sum projection of a 2D HETCOR spectrum (hatched line) with the  $^1\text{H}$  line shape using the recovered  $^1\text{H}$  spin magnetization (solid line) with the same CP time. The time gain is about 16.

It should be noted that this proposed method is not restricted to the shown 2D heteronuclear correlation experiment using CP. Any other polarization transfer mechanism can be used like Lee-Goldburg CP [62], REPT [80], or even  $J$ -coupling [71]. Furthermore, any spin manipulations during the  $t_1$  time domain can be applied, provided those can also be done equivalently in the I spin signal acquisition period.

For example, if  $^1\text{H}$  PMLG decoupling [6] is used in  $t_1$  to suppress unwanted spin diffusion, one should use w-PMLG [81] instead for the 1D experiment. Many other possibilities exist.

#### **Fast measurement of CP transfer curves of overlaid peaks**

Interatomic distances can be determined using the dipolar couplings between the nuclei. REDOR [6] is a standard technique for measuring distances between heteronuclei. The experiment is simple and robust and does not require polarization transfer steps. Alternatively, the CP build-up behaviour of  $^{13}\text{C}$  signals with simultaneous suppression of  $^1\text{H}$  spin diffusion (LG-CP) has been used to extract C-H distance information in small molecules e.g. [76]. As long as the spectral resolution on the detected nucleus is given (almost no problem for  $^{13}\text{C}$  NMR) 1D LG-CP spectra can be acquired. However, if the spectral resolution is not given, i.e. if several CP signals overlap, a simple data analysis is no longer possible. As seen in Fig. 4.2, this problem exists for nanocrystalline hydroxyapatite. The F2 projection of the 2D HETCOR spectrum of the sample shows overlaid peaks in the  $^{31}\text{P}$  dimension. Hence, if one is interested in the dipolar coupling using the CP transfer curves one has to acquire full 2D data sets.

However, spectral resolution is given for  $^1\text{H}$  NMR. Hence, measuring the F1 sum projection with the proposed two-scan technique (using transferred  $^1\text{H}$  polarization) the time-consuming 2D experiments are replaced by a 1D version. In this case, the CP curve containing the heteronuclear dipole coupling is now measured via  $^1\text{H}$  detection which has also a sensitivity advantage because of the large gyromagnetic ratio. A series of 41 experiments was carried out for the nanocrystalline hydroxyapatite to demonstrate the precision of CP curve determination. For each  $^1\text{H}$  chemical shift, the corresponding CP data can be obtained easily. The CP transfer curves for the  $\text{OH}^-$  protons of the crystalline hydroxyapatite core and of those in  $\text{HPO}_4^{2-}$  groups of the amorphous surface layer are shown in Fig. 4.4. These transfer curves are useful not only to distinguish between hydrogen in the form of hydrogen phosphate groups or hydroxyl in spatial proximity of phosphate groups; in principle the mutual distances can also be determined. Note: the corresponding  $^{31}\text{P}$  signals are almost identical and differ only in their line width.



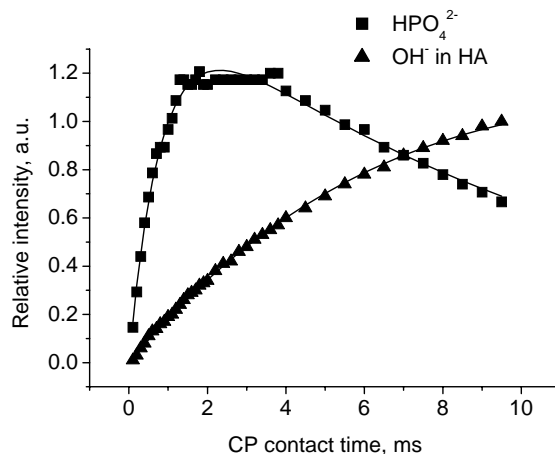


Fig. 4.4  $^1\text{H}$  detected CP curves of nanocrystalline hydroxyapatite using the recovered  $^1\text{H}$  signal of the protons of  $\text{HPO}_4^{2-}$  units of the amorphous surface (squares, data taken at 10 ppm) and of the OH protons of the crystalline hydroxyapatite bulk (triangles, 0 ppm data); cf. also Fig. 4.3

### Spectral editing and probing organic-inorganic interfaces

Organic-inorganic interfaces play an important role not only in material sciences where components with different mechanical properties are combined to produce novel, smart materials having an improved performance. Bone – as a natural example - is a complex composite of organic and mineral phases conferring toughness and stiffness, respectively [81]. The organic phase is a matrix of proteins, mainly collagen, and other macromolecules including PGs rich in acidic GAGs. The inorganic phase is a hydroxylated calcium phosphate resembling hydroxyapatite. Although the relationship between the two phases must be crucial to the properties of bone in health and disease, little is known about the macromolecules stabilising the boundary. Consequently, bone has also been studied extensively by NMR [32; 38; 82-84]. The primary target for NMR investigations of the organic-inorganic interface is to detect the direct binding sites between the organic matrix and the mineral crystal. So far, various papers have been published for synthetic model systems [44; 85-87] and for bone itself [88; 89].

Here, another useful experiment based on the suggested difference method is explained. The basic problem for identifying the organic binding sites is that both the  $^1\text{H}$  and  $^{13}\text{C}$  spectra are crowded by all protein resonances. In other words, the signals of the interface binding sites are superimposed by unwanted protein matrix signals. These must be suppressed. The idea is the following: In a first step, the  $^1\text{H}$  magnetization of the mineral crystal in bone is selected with simultaneous suppression of all  $^1\text{H}$  protein signals. This can easily be achieved by the proposed two-scan method. Due to the CP process to  $^{31}\text{P}$ , only the proton signals of the mineral crystal of bone remain, whereas all protein resonances disappear. After that,  $^1\text{H}$  spin diffusion is allowed and the  $^1\text{H}$  magnetization (still in the inorganic crystal) can flow across the interface. In a subsequent step using a short CP contact time to  $^{13}\text{C}$  the organic binding sites at the interface can be identified completely background-free from the entire protein matrix.

This concept shall be demonstrated on a model compound. The structure of an isolated O-phospho-L-serine molecule is shown schematically in Fig. 4.5.

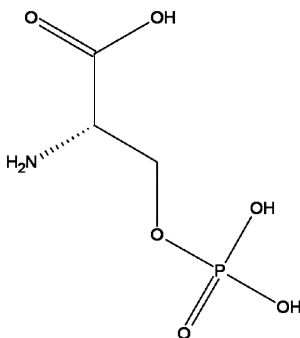


Fig. 4.5 Schematic structure of O-phospho-L-serine

The phosphate group shall represent the “surface group of a hypothetical mineral crystal” and the organic part of the molecule serves as “protein matrix”. Intermolecular interactions are neglected as an approximation. Using the proposed difference method with short CP contact time of  $80\ \mu\text{s}$ , the  $^1\text{H}$  signals of the protons of the hydrogen phosphate group can be selected almost exclusively (cf. Fig. 4.6). Note, that due to intermolecular interactions some carboxyl protons are also excited, but this is not relevant for this model case. This step is equivalent to the

selection of the  $^1\text{H}$  magnetization in the mineral crystal of bone. Now, the  $^1\text{H}$  magnetization is stored along the z-axis. Due to spin diffusion this  $^1\text{H}$  magnetization “flows” then into the organic part of the molecule as can be seen in Fig. 4.6. After only 2 ms all  $^1\text{H}$  signals of the molecule appear as expected. Further work on bone is now in progress exploiting this principle.

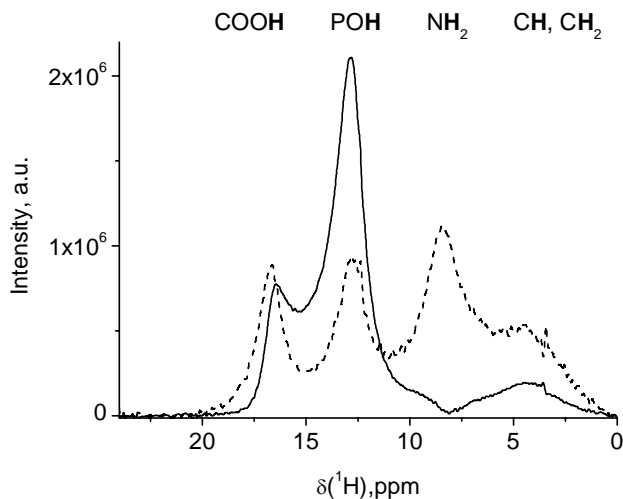


Fig. 4.6 Recovered  $^1\text{H}$  MAS NMR spectrum of *O*-phospho-*L*-serine after 80  $\mu\text{s}$  CP contact time (solid line) and after an additional  $^1\text{H}$  spin diffusion delay of 2 ms (hatched) on. For details see text.

### 4.3. Conclusions

It has been shown that in CP experiments the transferred I spin magnetization can be used for spectroscopy which is normally lost when detecting the S spin magnetization. This transferred part of the I spin magnetization can easily be “recovered” by taking the difference between two scans without and with polarization transfer active. This simple trick enables a wide range of useful experiments. First of all, this 1D signal is equivalent to the entire F1 sum projection of 2D heteronuclear experiments without increment of the indirect dimension. As it can be employed in any n-dimensional experiment it means a reduction of the time dimensions by one.

Furthermore, this experiment is ideal for spectral editing purposes. If one is, for example, solely interested in  $^1\text{H}$  signals of protons coupled to heteronuclear spins with simultaneous suppression of all uncoupled sites, one straightforward opportunity is to use first the normal CP step from the protons to the S spins, then store the S spin magnetization, saturate all proton signals and, finally, do backward CP to  $^1\text{H}$ . Thus, two CP steps are required and the second suffers from intensity losses, due to the gyromagnetic ratios and the fact that this CP must be short to avoid spin diffusion. Using the proposed experiment this selection process is done directly without the need of the second sensitivity-consuming CP step. As mentioned earlier, any kind of spin manipulation in  $t_1$  and polarization transfer methods can be applied, thus making the experiment applicable for a number of different cases. The most important application, is to be seen in the investigation interfaces of synthetic and natural organic-inorganic compound materials like bone due to the unique signal editing features.

## 5. Nanocrystalline hydroxyapatite: NMR and XRD structural investigations

Nanocrystalline hydroxyapatite is a material intermediate between highly crystalline and highly disordered biological hydroxyapatites. Surface effects, such as strain, lattice distortions and substitutions of individual atoms or structural units, play a significant role in the overall chemistry of nanocrystalline samples because the volume of the surface layer becomes comparable to the volume of the “bulk” material, or core of the particles. The situation is even worse for biological samples. For example, in the case of bones mineral crystallites are extremely small and their hydroxyapatite crystalline core does not have direct contact to the organic matrix which actually directs the mineralization process [1; 12]. Crystalline hydroxyapatite forms only about 20% of bone mineral phase [38]. As diffraction measurements can provide information only on crystalline structures almost 80% of the bone mineral is out of scope of these analytical techniques. Detailed investigations of nanocrystalline hydroxyapatite are important for several reasons: to learn more about the influence of surface effects on crystallite structure, for better understanding of biomineralization processes and to prepare biomimetic materials for healing bones, etc.

The nanocrystalline hydroxyapatite sample used in this work was prepared by a continuous precipitation process from aqueous solution [90]. A small portion of carbon dioxide from the air was integrated as carbonate. These precipitated calcium phosphate nanoparticles have an elongated shape with mean dimensions of 10x10x40 nm (Fig. 5.1, left side). The XRD pattern of this material is highly broadened compared to the pattern of crystalline hydroxyapatite (Fig. 5.1, upper right side). However, as both XRD and IR spectra show the same structural features, it had commonly been concluded that this nanocrystalline precipitated product consists solely of hydroxyapatite [17; 91].

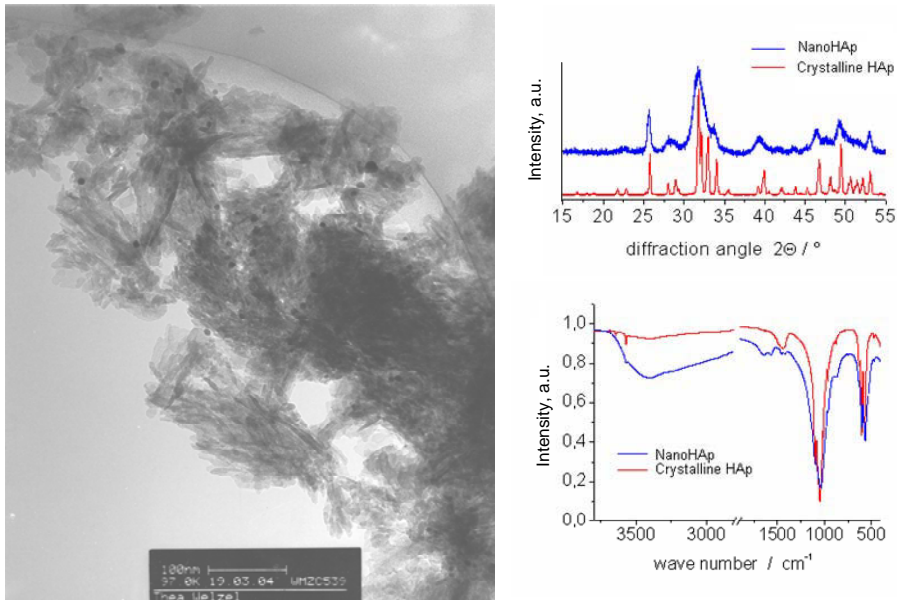


Fig. 5.1 Particles of the nanocrystalline hydroxyapatite sample. TEM micrograph (left), XRD (top right) and IR (bottom right). Pictures are adapted from Jäger et al. [16]

Chemical analysis of the nanocrystalline hydroxyapatite sample yielded 34.1 wt% Ca and 54.0 wt%  $\text{PO}_4^{3-}$  giving the overall molar Ca/P ratio of 1.51. This deviates from 1.67 - the ratio for the *stoichiometric* hydroxyapatite structure,  $\text{Ca}_5(\text{PO}_4)_3\text{OH}$ . Hence, it is commonly concluded that the material presents a calcium-deficient hydroxyapatite (CDHA) [33; 90]. A possible way to explain the calcium deficiency in the nanocrystalline sample is to assume the presence of a second phase, different from hydroxyapatite, and having a lower Ca/P ratio [92]. Possible candidates for such a hypothetical second composition are octacalcium phosphate (OCP),  $\text{Ca}_8(\text{PO}_4)_6 \cdot 5\text{H}_2\text{O}$ , and dicalcium phosphate dihydrate (Brushite),  $\text{CaHPO}_4 \cdot 2\text{H}_2\text{O}$ , having the Ca/P ratios 1.33 and 1.00, respectively. The remaining mass of 11.9 wt% in the material from the elemental analysis is ascribed to water, hydroxide ions and carbonate as shown by thermogravimetry [16].

---

By performing integrations of a 2D HETCOR spectrum and studying CP dynamics of narrow (around 0 ppm  $^1\text{H}$ ) and broad (3-18 ppm  $^1\text{H}$ ) signals (Fig. 5.2) Jäger et al. [16] showed that the nanocrystalline hydroxyapatite sample contains a hydroxyapatite phase together with  $\text{HPO}_4^{2-}$  groups and water molecules which are combined together forming nanocrystals with a crystalline hydroxyapatite core and a disordered surface layer (Fig. 5.3). The thickness of the surface layer is about 10% of the particle dimensions (10x10x40 nm). Therefore this surface layer contains half of the phosphate content, which – due to its disordered nature – does not contribute to the intensity of the hydroxyapatite diffraction lines in the XRD pattern. The average chemical composition of the surface layer was determined [16] and formally corresponds to octacalcium phosphate,  $\text{Ca}_8(\text{HPO}_4)_2(\text{PO}_4)_4 \cdot 5\text{H}_2\text{O}$ , and thus a possible explanation of the calcium deficiency of the sample was emerged.

Still the question about the stoichiometry of the crystalline core remained. XRD patterns only indicate hydroxyapatite diffraction lines and are very broad. So, the signals of other composition (which has to be in the diffractogram since water and  $\text{HPO}_4^{2-}$  groups has been found by NMR) can lie under the hydroxyapatite signals and, therefore, can not be easily detected. This chapter is devoted to the detailed study of  $^1\text{H}$ - $^{31}\text{P}$  dipolar couplings in order to prove, that the crystalline core of the nanocrystalline sample is hydroxyapatite; and to show that carefully measured XRD diffractograms contain information about the disordered surface layer.

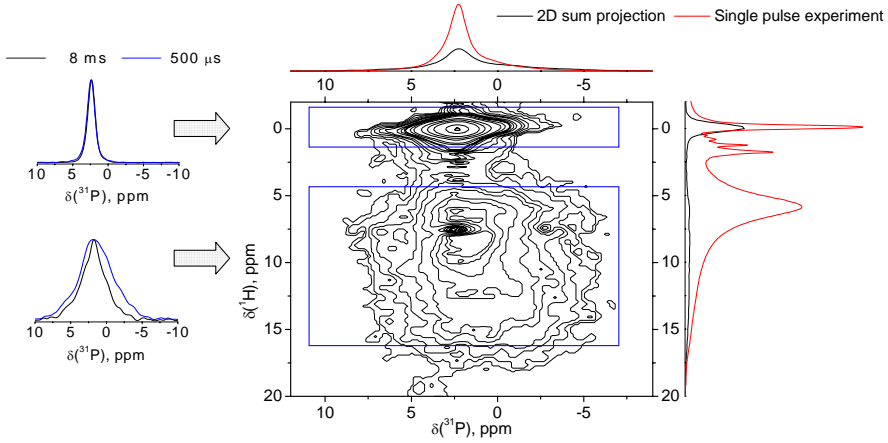


Fig. 5.2 2D  $^1\text{H}$ - $^{31}\text{P}$  HETCOR experiment on nanocrystalline hydroxyapatite sample. Left side – 2D integrations using two different contact times (500  $\mu\text{s}$  and 8 ms) compared. Top and right – overall  $^{31}\text{P}$  and  $^1\text{H}$  projections respectively compared with  $^{31}\text{P}$  and  $^1\text{H}$  single pulse experiments (in red). The peak at 0 ppm on the  $^1\text{H}$  scale corresponds to the OH groups in hydroxyapatite phase (core of the particles) and the broad component in the region from 3 to 18 ppm is constituted of water and  $\text{HPO}_4^{2-}$  signals.

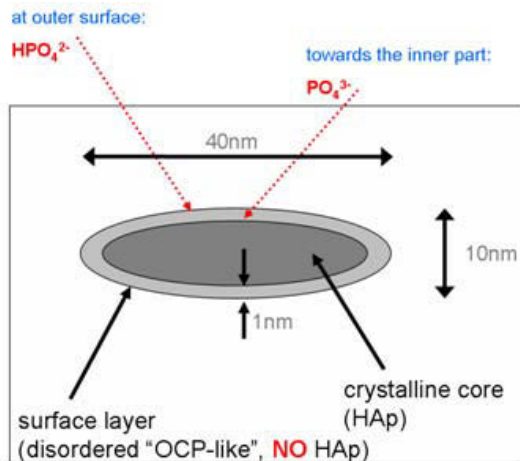


Fig. 5.3 “Core+surface” model of nanoparticles of hydroxyapatite from Jäger et al. [16].



## 5.1. Stoichiometry of the crystalline core

All hydrogen atoms in a highly crystalline hydroxyapatite form OH<sup>-</sup> groups and are in crystallographically and chemically equal positions. Therefore, the corresponding <sup>1</sup>H NMR spectrum has only one narrow peak located at 0 ppm (black line in Fig. 5.4).

To prove that the 0 ppm line is indeed characteristic for the hydroxyapatite structure, <sup>1</sup>H-<sup>31</sup>P dipolar couplings were measured with Cross Polarization and REDOR techniques and the results for highly crystalline and nanocrystalline samples were compared.

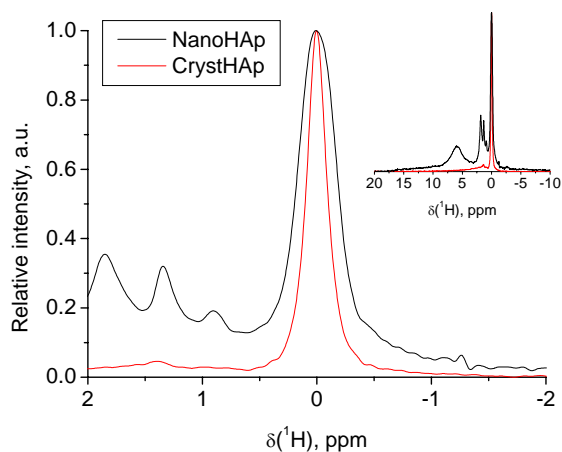
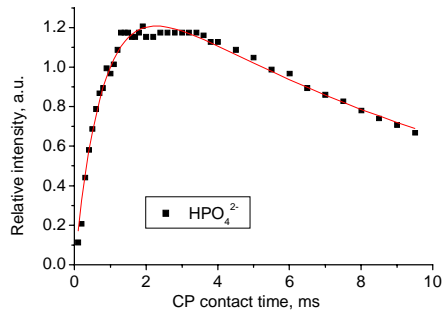


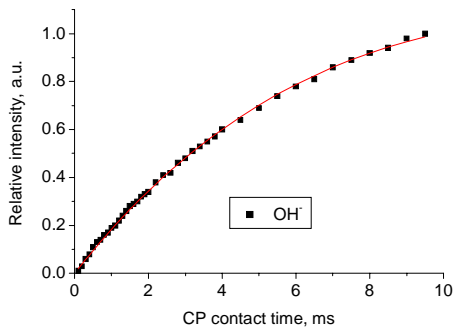
*Fig. 5.4* <sup>1</sup>H NMR of nanocrystalline and crystalline hydroxyapatite samples. Inset: full spectrum range. Significant line broadening of OH signal occurs for nanocrystalline sample. Also, strong water (approx. 6 ppm) and HPO<sub>4</sub><sup>2-</sup> (around 10-12 ppm) signals appear in the spectrum which are ascribed to the surface layer [16]. Sharp signals around 2-3 ppm are due to impurities.

The cross polarization behaviour of the OH<sup>-</sup> and HPO<sub>4</sub><sup>2-</sup> groups, indicated on right side of Fig. 5.2, was studied by a set of several 2D experiments with different contact time and by a “two-step” experiment to save time and increase the productivity. A series of 41 experiments with contact times from 100 μs to 9.9 ms was carried out and the experimental data were fitted with the equation 3.2-2 [93]. The resulting build-up times are: T<sub>C</sub>=6.36±0.09 and 0.88±0.04 ms for P-OH<sup>-</sup> and

$\text{HPO}_4^{2-}$  groups respectively. As it was expected, the broad component showed faster cross polarization build-up behaviour due to the shorter H-P distance in  $\text{HPO}_4^{2-}$  groups and additional protons from structural water. Such a big  $T_C$  value for the P-OH line is characteristic for the hydroxyapatite structure since it depends on the mean internuclear  $^1\text{H}$ - $^{31}\text{P}$  distance, which is approx. 0.53 nm in hydroxyapatite (2 OH groups and further 4 OH groups having a distance to the closest phosphorus atom of 0.4 nm and 0.6 nm respectively), and on the crystal lattice parameters.



a.



b.

Fig. 5.5 Cross polarization build-up curves fitting a) for  $\text{HPO}_4^{2-}$  groups and b) for OH groups. For details see text.

The fact that both build-up curves are fitted nicely with a single curve model confirms that proton environment of the phosphorus atoms is constant in the crystalline core as well as in the surface layer, but they differ from each other.

A detailed study of the proton environment of phosphorus atoms was performed with the  $^{31}\text{P}\{^1\text{H}\}$  REDOR technique. Since the technique is sensitive to the number of dephasing atoms, to the distances between the given atom and all the dephasing atoms as well as to the interatomic geometry, it can be utilized to study the stoichiometry of the crystalline core. Two  $^{31}\text{P}\{^1\text{H}\}$  REDOR dephasing curves were measured for the nanocrystalline and the crystalline samples. The curves are presented in Fig. 5.6 and show excellent coincidence especially at dephasing times shorter than 1.5 ms. This can serve as evidence that the mean proton-phosphorus interatomic distance and the mutual disposition of the nearest protons around the  $\text{PO}_4^{3-}$  group are the same in both samples.

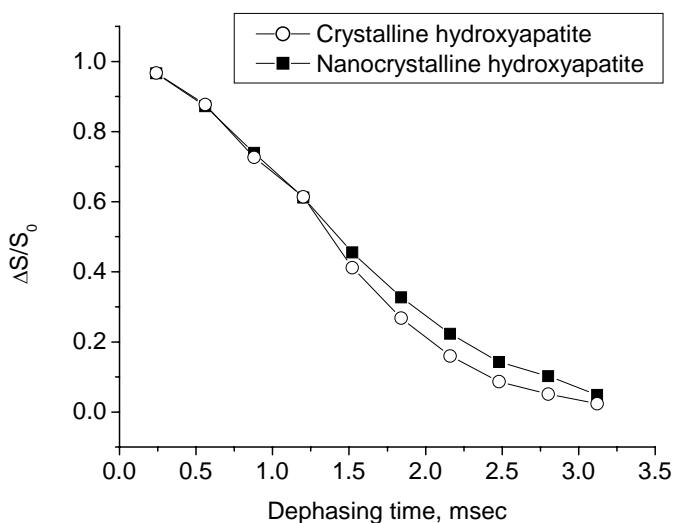


Fig. 5.6  $^{31}\text{P}\{^1\text{H}\}$  REDOR dephasing curves for crystalline and nanocrystalline hydroxyapatite samples.

Phosphorus environment of protons was studied by Echo- $^1\text{H}\{^{31}\text{P}\}$ REDOR and Echo- $^1\text{H}\{^{31}\text{P}\}$ REDOR-CP techniques. The corresponding dephasing curves are presented in Fig. 5.7 and Fig. 5.8.

The slightly slower dephasing behaviour of the nanocrystalline hydroxyapatite sample seen in Fig. 5.7 could be explained by taking into account the fact that the  $\text{PO}_4^{3-}$  groups in the interface between the core and the surface layer tend to become protonated  $\text{HPO}_4^{2-}$  (as in surface layer) thus changing the crystal lattice parameters of the core. Moreover, water incorporated into the surface layer and partial substitutions of  $\text{PO}_4^{3-}$  groups increase the mean  $\text{OH}^-$ - $\text{PO}_4^{3-}$  distance. All this leads to a slower dephasing of the hydroxyl groups in the core-surface interface. Performing an Echo-REDOR-CP experiment gives preferably the dephasing behaviour of the pure hydroxyapatite structure and it can be clearly seen (Fig. 5.8) that within the limits of experimental error the curves are identical. This means that the phosphorus environment of  $\text{OH}^-$  groups in the crystalline core of the nanocrystalline hydroxyapatite particles is the same as in crystalline hydroxyapatite sample.

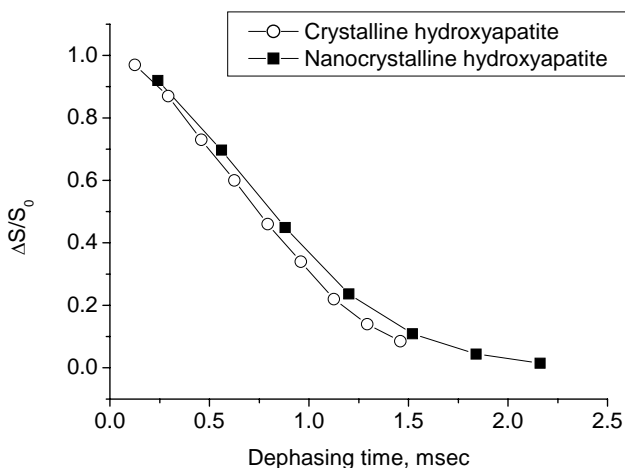


Fig. 5.7  $^1\text{H}\{^{31}\text{P}\}$  REDOR dephasing curves curves after Echo-REDOR experiment on nanocrystalline and crystalline hydroxyapatite samples. Data points are acquired by lineshape fitting.

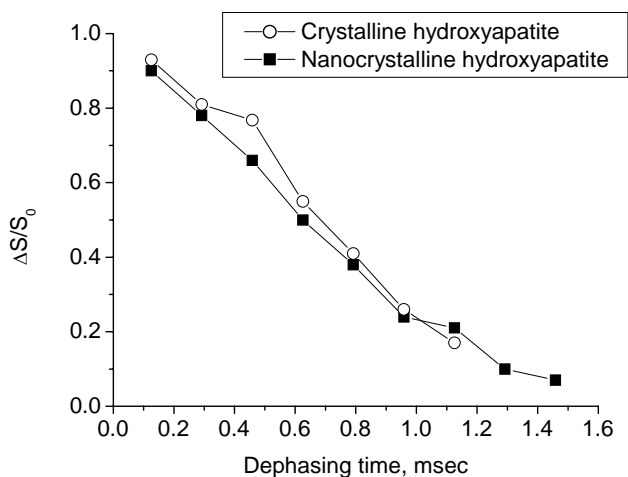


Fig. 5.8  $^1\text{H}\{^{31}\text{P}\}$  REDOR dephasing curves after Echo-REDOR-CP experiment on nanocrystalline and crystalline hydroxyapatite samples.

Therefore, detailed study of  $^1\text{H}\text{-}^{31}\text{P}$  dipolar couplings in the crystalline core of the nanocrystalline hydroxyapatite showed that the phosphorus environment of the  $\text{OH}^-$  groups and the proton environment of  $\text{PO}_4^{3-}$  groups are very similar to that of crystalline hydroxyapatite.

## 5.2. Why does the surface layer not contribute to the XRD lines?

Since it was found that nanocrystals of hydroxyapatite contain a surface layer, which is chemically different from stoichiometric hydroxyapatite, the question arose whether it is possible to see this layer in XRD diffractograms? Is this layer completely disordered or does it consist of a crystalline phosphate phase? To answer these questions the nanocrystalline hydroxyapatite sample was measured and the background-subtracted diffraction pattern was fitted with a simulated diffraction pattern. The observed XRD diffractogram of nanocrystalline hydroxyapatite was measured by Prof. Dr. M. Epple and the simulations were

carried out with Accelrys® Material Studio®. The simulations were made at several levels of sophistication of the crystallographic model.

Firstly, a theoretically calculated diffraction pattern was fitted to the observed diffractogram of nanocrystalline sample using hydroxyapatite as the only crystallographic phase and the only parameter to change was the crystallite size.

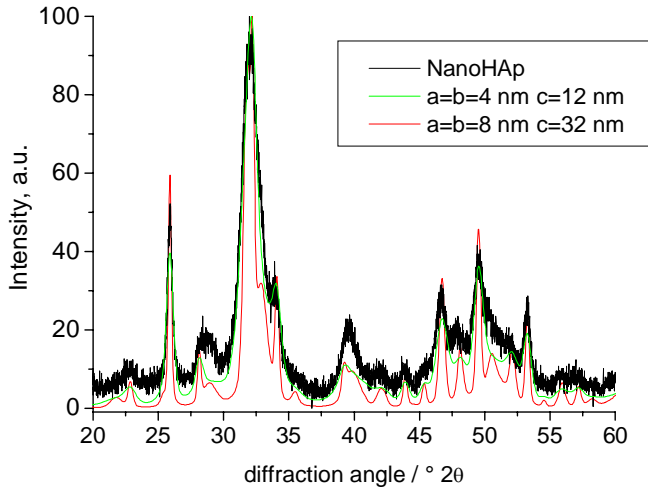


Fig. 5.9 Observed diffractogram of nanocrystalline hydroxyapatite and 2 simulations with different crystallite sizes.

Although a crystallite size of 4x4x12 nm gives the better fit of the XRD pattern than the model with crystallite dimensions of 8x8x32 nm (Fig. 5.9), this crystallite size is too small as compared to the 10x10x40 nm size determined by TEM. The situation can be improved by introducing a strain parameter into the simulation. In this case the crystallite size is fixed and the strain in the crystallographic directions a, b and c has to be fitted. Several crystal sizes were used for such simulations: 3x3x40, 4x4x40, 6x6x40 and 8x8x40 nm. Due to the crystal symmetry of hydroxyapatite, the directions a and b are crystallographically equivalent and the same value of strain has to be applied simultaneously for them. The best fit is achieved with a crystallite size 8x8x30 nm and 2% strain in the crystallographic directions a, b and c (Fig. 5.10).

This simulation shows a better fit to the observed data, but the diffraction lines at  $28^\circ$ ,  $40^\circ$  and narrow peaks in the region  $46^\circ$ - $58.5^\circ$  are still not broad enough.

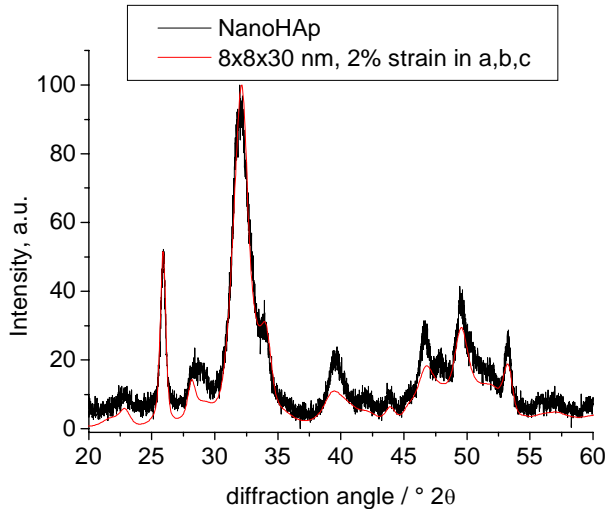


Fig. 5.10 Fitting of the observed diffractogram with 2% strain.

Summarizing the results obtained with the two levels of sophistication of the crystallographic model described so far it is found that the results of evaluating the XRD pattern by simulation methods and of TEM measurements differ slightly in resulting crystallite size. Moreover, the calcium deficiency and the presence of  $\text{HPO}_4^{2-}$  groups, found previously by NMR, can not be explained.

The next step to improve the fitting crystallographic model was to take into account the surface layer separately to see how the surface effects may influence the simulated diffraction pattern.

A two-phase model derived from the NMR investigations was considered consisting of a crystalline hydroxyapatite core and a chemically different surface layer. Core dimensions of  $1 \times 1 \times 60$ ,  $2 \times 2 \times 60$ ,  $4 \times 4 \times 60$  and  $6 \times 6 \times 60$  hydroxyapatite unit cells were taken (Fig. 5.11) for the simulations (one hydroxyapatite unit cell is  $9.4 \times 9.4 \times 6.9$  nm size). The surface was simulated as a 1 unit cell thick layer covering the core. The simulations were made in the following manner:

- at first, 4 compositions for the surface layer were assumed: monetite ( $\text{CaHPO}_4$ ), brushite ( $\text{CaHPO}_4 \cdot 2(\text{H}_2\text{O})$ ), tricalcium phosphate ( $\text{Ca}_3(\text{PO}_4)_2$ ) and hydroxyapatite
- the “averaged” simulated patterns were constructed from calculating the equally weighted sum of these individual patterns
- 32 diffraction patterns for each of the 4 compositions were simulated to account different crystallite sizes (in total 4 sizes) and different values of strain (in total 8 values). For each core size surface diffractograms were simulated with 0%, 0.5%, 1%, 1.5%, 2%, 2.5%, 3% and 5% strain in all crystallographic directions for each composition.

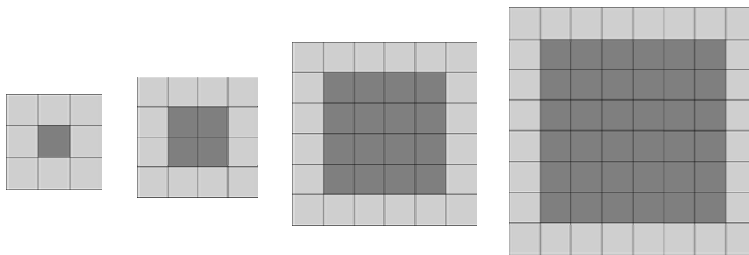


*Fig. 5.11 The particle sizes and relative core/surface content used in XRD simulations. Every small box represents a “unit cell”. The core is stoichiometric crystalline hydroxyapatite. The surface is modelled as average of monetite, brushite, tricalcium phosphate and hydroxyapatite.*

Such a model actually describes the situation in which the sample consists of four types of particles, differing in the composition of their surface layers. This model can be handled mathematically but it represents only an approximation to the real situation where all particles are thought to be identical, having the same “average” surface layer content of a microscopic mixture of monetite, brushite, tricalcium phosphate and hydroxyapatite.

The contributions of the core and the surface to the diffraction pattern were weighted accordingly to their volume in the crystallite (e.g. a crystallite with  $6 \times 6 \times 60$  unit cells has 960 core cells and 1200 surface cells, that gives a core/surface ratio of 0.8).



Two examples of these simulated diffractograms of “averaged” surface composition are presented in Fig. 5.12. Despite hydroxyapatite composition is included into the “average” model, the peaks at  $12^\circ$  and peaks in the region from  $17^\circ$  to  $35^\circ$  do have poor coincidence with observed peaks.

If try to fit the observed data with synthesized pattern consisting from hydroxyapatite core diffractogram with “average” surface diffractogram varying only their intensities, the surface contribution goes down to a neglectable value (Fig. 5.12, Fig. 5.13).

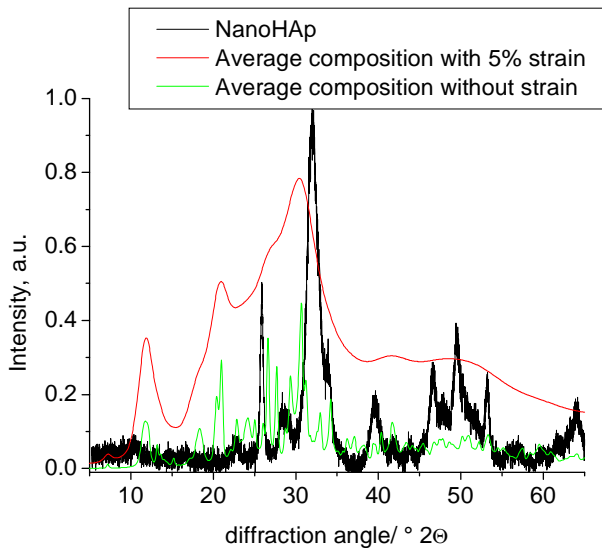


Fig. 5.12 Observed XRD patterns of nanocrystalline hydroxyapatite vs. the simulated “averaged” XRD pattern of the surface layer, calculated with two different values of strain. Not yet normalized.

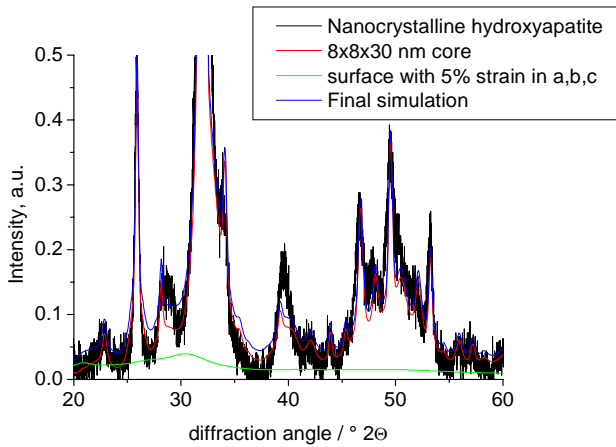


Fig. 5.13 Final simulation of the 60x60x300 nm crystallite with “core+surface” model. The graphs are scaled by particle volume and signal area.

The fact that no structure gives a better fit of the simulated pattern to the observed one leads to the conclusion that the 11.9 wt% not determined in elemental analysis, which are made up of water,  $\text{CO}_3^{2-}$  and  $\text{HPO}_4^{2-}$  groups, do not form any long-range ordered structure. An attempt to find their contributions to the diffraction pattern can only be made if no baseline subtraction is performed (baseline signal is not observable in the hydroxyapatite diffraction pattern displayed in Fig. 5.9, Fig. 5.10, Fig. 5.12 and Fig. 5.13, as it was subtracted automatically by the diffractometer software).

The original observed diffraction patterns, so called RAW-files, of the nanocrystalline hydroxyapatite, of the bone and of the mineralized cartilage as well as of the background signal of the glass sample holder are shown in Fig. 5.14. All the diffraction patterns show a strong, exponential decay like baseline which also contains information about the disordered surface layer. Careful evaluation of the baseline signal is an essential point for the interpretation of XRD patterns of materials containing nanocrystalline components.

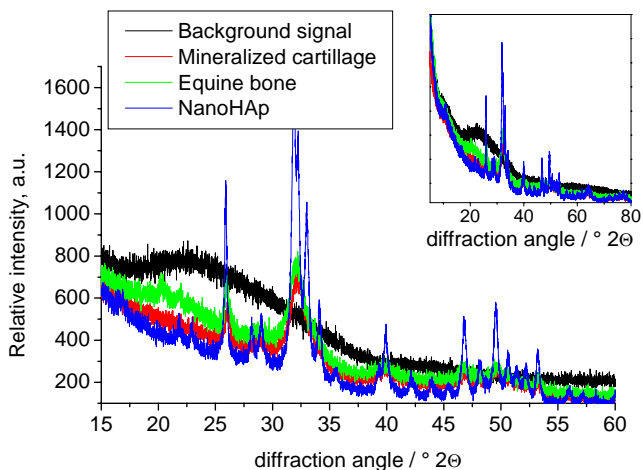


Fig. 5.14 Section of the raw XRD diffractograms of nanocrystalline hydroxyapatite, mineralized cartilage, equine bone, and signal of the empty sample holder. Top right – the same, but full angle range.

An opportunity to avoid background signal problems is to measure several samples, such as nanocrystalline and highly crystalline hydroxyapatites, in a row using identical experimental conditions. In this case there is a chance that the true background signal (coming up from the experimental conditions) of the two patterns is similar and therefore it can be separated from the contributions of the disordered components of the nanocrystalline sample. Such measurements were kindly carried out by Dr. Burkhard Peplinski. The resulting diffraction patterns were normalized for measuring time and are presented in Fig. 5.15.

In order to obtain further information about the structure of the nanocrystalline sample and especially its disordered surface layer, a Fourier filter line broadening method was applied to the observed diffractogram of a highly crystalline hydroxyapatite reference sample. Since the broadening technique does not introduce any additional background signals and keeps the signal areas constant it can be applied for the purposes. A limitation of this data treatment method is that it does not allow to broaden the lines differently for the different crystallographic directions. Therefore, not all diffraction lines are described with the same quality. Since the hydroxyapatite structure of the core represents only about 60% of the

total particle volume, the broadened diffractogram of the crystalline hydroxyapatite reference sample has to be scaled down by factor of 1.67 (Fig. 5.16). The comparison of the two diffraction patterns in Fig. 5.16 revealed that the observed diffraction pattern of the nanocrystalline sample contains a very broad signal in the region of  $20^{\circ}$ - $60^{\circ}$ . It represents X-ray amorphous content in the particles surface layer. The broad peaks resemble that of hydroxyapatite and can not be associated with any other known calcium phosphate structure that contains water or  $\text{HPO}_4^{2-}$  groups. Therefore it can be concluded that the surface layer of the hydroxyapatite nanocrystals has a highly distorted (but not completely disordered!) structure resembling that of hydroxyapatite with  $\text{HPO}_4^{2-}$  (and some  $\text{CO}_3^{2-}$ ) groups instead of  $\text{PO}_4^{3-}$  groups and water instead of  $\text{OH}^-$  groups.

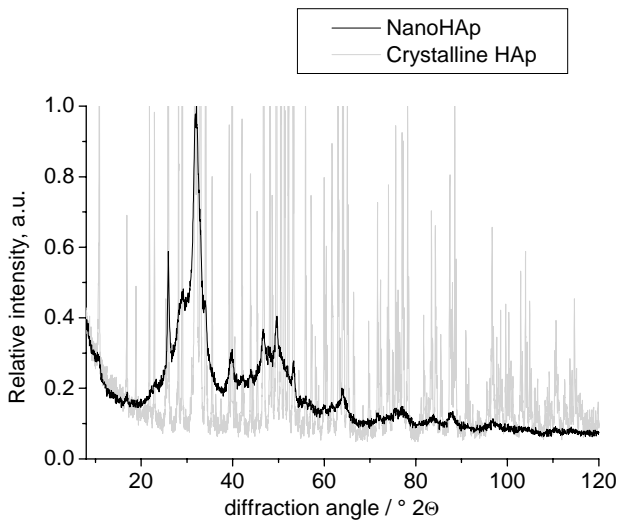


Fig. 5.15 High-end raw XRD diffractograms of nanocrystalline and highly crystalline hydroxyapatite samples.

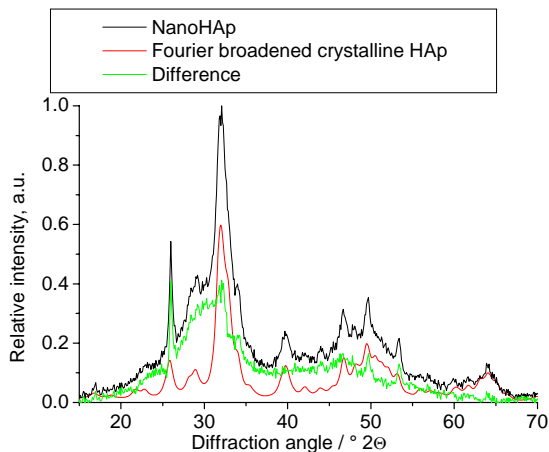


Fig. 5.16 Normalized by experimental data and phosphate content Fourier broadened diffractogram of highly crystalline hydroxyapatite and nanocrystalline hydroxyapatite. Difference line represents amorphous phase.

### 5.3. Conclusions

An NMR strategy was developed to study the structure of nanocrystalline hydroxyapatite in detail. By precise measurements of both proton environment of phosphate groups and phosphorus environment of hydroxyl groups it has been proved that the crystal structure of the crystallite core of the nanoparticles is identical with the crystal structure of *stoichiometric* hydroxyapatite. It has been shown that using NMR techniques it is possible to study the crystalline part of nanoparticles and its structural properties independent of the disordered surface phase, thus obtaining detailed information about biomineralization processes during bone formation and bone remodelling. Such information is important for designing drugs and new materials.

The combination of NMR and XRD investigations on nanocrystalline hydroxyapatite sample showed that often applied in the evolution of XRD patterns baseline subtraction must be carried out extremely carefully to get information about poorly ordered or disordered materials. High X-ray hardware demands and the complexity of baseline interpretation make XRD investigation of nanocrystallite materials a non-trivial task.

Also it was found that the surface of the hydroxyapatite nanocrystals is not completely disordered, as it was suggested before, but resembles the hydroxyapatite structure with  $\text{HPO}_4^{2-}$  (and some  $\text{CO}_3^{2-}$ ) groups instead of  $\text{PO}_4^{3-}$  groups and water instead of  $\text{OH}^-$  groups. Since this is the surface that defines the chemical properties of the nanoparticles of hydroxyapatite, the results presented in this chapter are of key importance for a deeper understanding of bioactivity, reactivity and molecular binding ability of nanocrystalline hydroxyapatite.

## 6. Mineral phase of bone characterization

The mineral phase of bones and teeth consists of carbonated calcium phosphate, the approximate chemical composition of which can be described as  $\text{Ca}_{10}(\text{PO}_4)_{6-x}(\text{CO}_3)_x(\text{OH})_2$  and mostly corresponds to the hydroxyapatite structure with some of the phosphate groups being substituted by carbonate units. Incorporation of carbonate units is usually approx. 4%-5%. The crystallites of bone mineral are needle- or plate-like with typical dimensions of 3x20x45 nm [12]. Due to the extremely small size, substitutions, crystal lattice distortions and surrounding organic matrix, structural elucidation becomes a state-of-the-art task [94]. Early X-ray investigations showed that nanocrystals consist of 2 phases – crystalline hydroxyapatite-like and amorphous [95]. The amorphous layer was associated with an intermediate phase being formed as a precursor of the hydroxyapatite mineral from the supersaturated solution. But some of further radial distribution function studies failed to detect an amorphous calcium-phosphate solid phase in bone mineral [96]. The presence of additional ions, such as  $\text{F}^-$ ,  $\text{Sr}^{2+}$  and others, can influence the properties of the bone crystals. Fluorine can simultaneously shift the mineralization profile of bone to higher mineral density, while increasing bone turnover and bone mass. On the other hand, strontium can have the opposite effect by increasing bone mass while shifting the mineralization profile towards lower mineral density. When given at a high dose, it can prevent mineral formation and induce rickets. The possible mechanism here is replacing  $\text{Ca}^{2+}$  in the apatite lattice, thus increasing bone mineral solubility [97].

Grynopas *et al.* have studied the effects of age and diseases on bone mineral formation and resorption in terms of hypo- and hypermineralization. He showed that the distribution of bone particles of various age can be influenced by biological and chemical factors. For example, rapid growth, or rapid remodelling induces a shift of mineralization profile towards lower mineral densities. This shift is accompanied by a decrease in crystal size [97]. In general, mineralization of bone in normal physiology and in many pathologies is driven by the rate of bone

turnover: the higher the rate of turnover the greater the hypomineralization and vice versa. In common diffraction peaks of bone mineral tend to become narrower with age [98]. This was interpreted as an increase in crystallite size and decrease of crystal defects.

FTIR studies showed a dependence of mineralization and crystallization from the place inside an osteon: most of the mineral was concentrated in the center of an osteon. Moreover, carbonate density or  $\text{CO}_3^{2-}/\text{PO}_4^{3-}$  ratio is inversely proportional to the distance from the osteonal center with maximum dropdown of 20%-30% for most mature mineral in the osteon [99].

The aim of the present study was to exploit the advantages of solid-state nuclear magnetic resonance techniques to characterise the mineral structure of equine bones.

### **Sample preparation and histology**

Osteochondral samples from the dorsal proximal aspect of the third tarsal bone were obtained from 5 horses following humane destruction for reasons other than this study. These were stored frozen at  $-20^\circ\text{C}$  until examination. The horses without lameness were aged 3 (sample 85), 6 (sample 82), and 7 (sample 27) years. The horses with osteo-arthritic change were aged 10 (sample 124) and 17 (sample 64) years.

Osteochondral samples underwent routine histological preparation, decalcification and paraffin-embedding. 4  $\mu\text{m}$  thick sections were stained with Toluidine blue and Haematoxylin and Eosin for evaluation of the articular cartilage and subchondral bone. Sections were assessed for evidence of osteoarthritic change.

Samples 27, 82 and 85 had no evidence of osteoarthritic change in either the cartilage or subchondral bone at any site within the joint. Samples 64 and 124 had clear evidence of osteoarthritic change within this joint cartilage, structural disorganization with chondrone formation and subchondral bone fibrosis. Sample 64 had clear definition of the subchondral bone margins. Sample 124 had marked



thickening of the subchondral bone with generalized loss of porosity, typical of osteoarthritic change.

## 6.1. NMR experiments on the bone samples

Phosphorus spin-echo experiment of the bone samples shows exclusively the mineral phase of the bone tissue which is presented by a slightly asymmetrical line consisting from a hydroxyapatite signal centered at 2.3 ppm with line width about 3.5 ppm and a broad component underneath (Fig. 6.1). The origin of this broad component becomes clear from a 2D HETCOR experiment discussed later. Such a big value for the hydroxyapatite signal line width (compared to pure hydroxyapatite line width of 1.1 ppm) is due to small crystallite size and consequent lattice distortions, impurities and substitutions. The proton spin-echo spectrum of 3 samples (Fig. 6.2) shows the same structural features as nanocrystalline hydroxyapatite (e.g. OH<sup>-</sup> signal of hydroxyapatite at 0 ppm, broad water peak centered at 5 ppm and a shoulder of HPO<sub>4</sub><sup>2-</sup> up to 17 ppm) together with additional organic matrix sharp resonances in the range between 1-3 ppm. For mineral phase characterization reasons the proton spectrum has to be cleared from organic signals. This can be performed by measuring a 2D <sup>1</sup>H-<sup>31</sup>P HETCOR experiment. Fig. 6.3 shows the two-dimensional <sup>1</sup>H-<sup>31</sup>P HETCOR spectra for samples 27 and 64 as typical samples from the healthy and osteoarthritic groups. The spectra were recorded using FSLG (frequency switched Lee-Goldburg) cross polarization and <sup>1</sup>H-<sup>31</sup>P mixing times of 0.5 ms, 2 ms and 8 ms. These spectra show the spatial correlations between <sup>1</sup>H spins (from various groups) and <sup>31</sup>P spins in the sample, and so essentially contain information about the spatial proximity of <sup>1</sup>H containing groups in the mineral closely bound to the neighbouring phosphate and mineral surface, there being little phosphate elsewhere in the bone matrix observable by NMR [38]. As most protons of the protein matrix are not close to <sup>31</sup>P, the protons in the protein matrix are not observed in this experiment, making it an excellent method to examine the mineral component of a sample exclusively, without resorting to deproteination of the sample, as discussed previously by Ackerman *et al.* [38].

The spectra in Fig. 6.3 show at least three broad signals in the  $^1\text{H}$  dimension: a sharper signal at approximately 0 ppm due to  $\text{OH}^-$  hydroxyl ions, a broad peak centered around 5.5 ppm due to structural water in the mineral (or at least, water in close proximity to mineral phosphate, otherwise this signal would not appear in the spectrum at all) and a very broad peak in the region 5 – 15 ppm from  $\text{HPO}_4^{2-}$  hydrogen phosphate groups. The  $\text{OH}^-$   $^1\text{H}$  signal is correlated with a relatively narrow  $^{31}\text{P}$  resonance, indicating that the phosphate groups in close spatial proximity to the hydroxyl groups are relatively well ordered, and thus belong to a relatively crystalline hydroxyapatite structure. The  $\text{H}_2\text{O}$  and  $\text{HPO}_4^{2-}$   $^1\text{H}$  signals, on the other hand, are correlated with relatively broad  $^{31}\text{P}$  lines, indicating that these  $^1\text{H}$  and their nearby phosphate/hydrogen phosphate groups are in relatively disordered environments.

HETCOR spectra in Fig. 6.3 were in fact recorded for between four and ten mixing times for each sample. This allows the approximate rate constants for the (presumed exponential) build-up of  $^{31}\text{P}$  magnetization by cross polarization from  $^1\text{H}$ , which in turn depends on the  $^1\text{H}$ - $^{31}\text{P}$  distances involved, as well as other interactions affecting both the  $^1\text{H}$  and  $^{31}\text{P}$  spins and any local molecular dynamics (for instance, local rotations or librations of water molecules) to be determined.

The rate constants were determined by fitting the experimental data to equation 3.2-2 [93]. The  $\tau_{HP}$  rate constants determined for the  $^{31}\text{P}$  signal intensity in the three regions indicated in Fig. 6.4 are given in Table 6.1-1 and Table 6.1-2 for HETCOR spectra using Hartman-Hahn and FSLG cross polarization respectively. It should be noted that  $\tau_{HP}$  for the  $\text{OH}^-/\text{PO}_4^{3-}$  region is difficult to determine accurately due to the near linear profile of the signal build-up for the  $^{31}\text{P}$  intensity in this spectral region over the range of mixing times used.

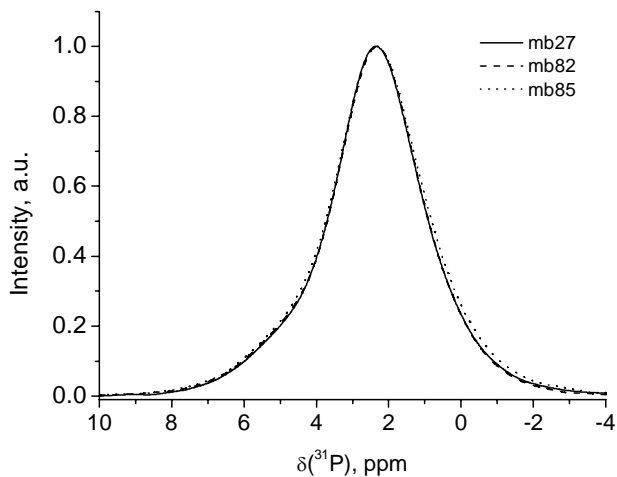


Fig. 6.1 Fully relaxed  $^{31}\text{P}$  echo experiment on three bone samples.  
Repetition delay 2880 s.

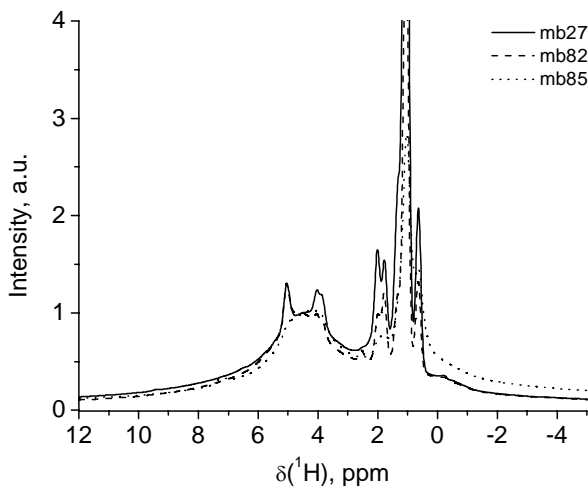
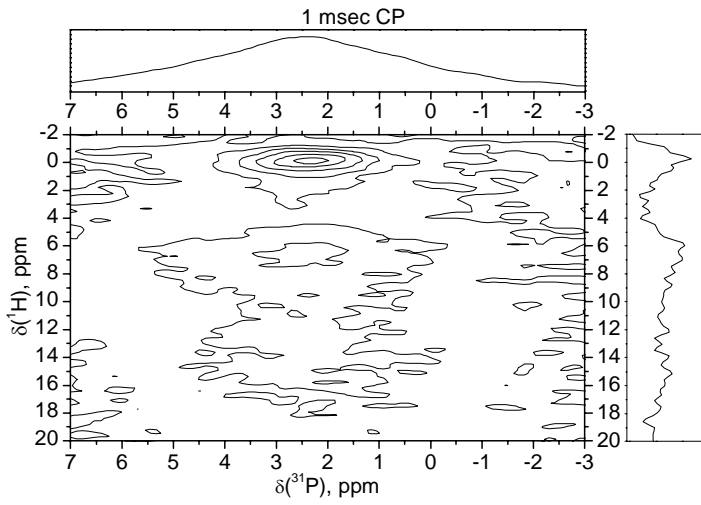
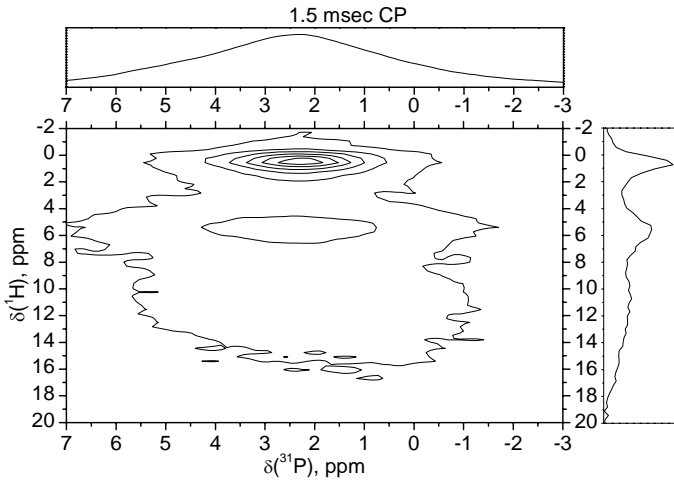


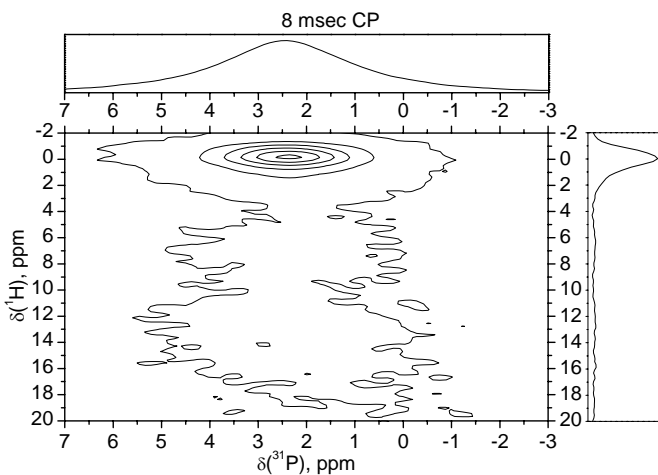
Fig. 6.2 Fully relaxed  $^1\text{H}$  echo experiment on three bone samples.  
Repetition delay 10 s.



a.



b.



c.

Fig. 6.3 2D  $^1\text{H}$ - $^{31}\text{P}$  FSLG HETCOR for sample 27 at mixing time of 1 ms (a), sample 64 at mixing time of 1.5 ms (b) and sample 27 at mixing time of 8 ms (c).

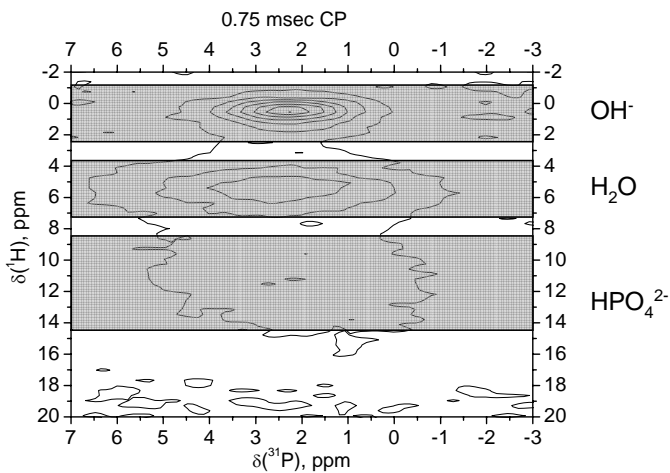


Fig. 6.4 OH, water and  $\text{HPO}_4^{2-}$   $^1\text{H}$  spectral assignment on the  $^1\text{H}$ - $^{31}\text{P}$  correlation spectra of the sample 27.

## 6. Mineral phase of bone characterization

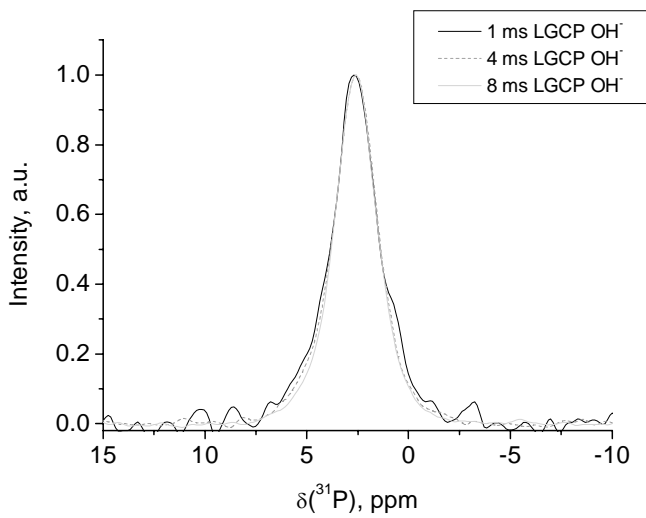
Table 6.1-1 The rate constants  $\tau_{HP}$  for the  $^{31}P$  intensity in the three spectral regions shown in Fig. 6.4 of  $^1H$ - $^{31}P$  HETCOR spectra recorded using Hartman-Hahn cross polarization. Error estimates are from curve fitting and do not take direct account of experimental errors.

Sample	$\tau_{HP}$ (OH/ $PO_4^{3-}$ region) / ms	$\tau_{HP}$ ( $H_2O$ / $PO_4^{3-}$ region) / ms	$\tau_{HP}$ ( $HPO_4^{2-}$ region) / ms
27	$2.9 \pm 0.5$	$0.6 \pm 0.1$	$0.4 \pm 0.2$
64	$10 \pm 4$	$0.6 \pm 0.1$	$0.6 \pm 0.1$
124	$2.6 \pm 0.8$	$0.7 \pm 0.1$	$0.6 \pm 0.2$

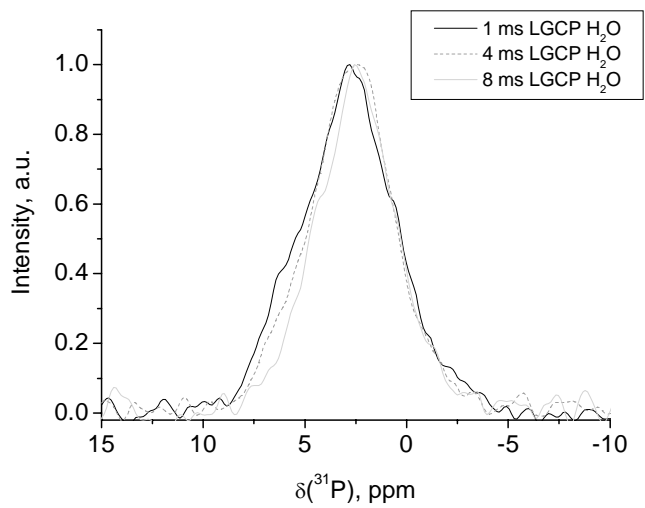
Table 6.1-2 The rate constants  $\tau_{HP}$  for the  $^{31}P$  intensity in the three spectral regions shown in Fig. 5.4 of  $^1H$ - $^{31}P$  HETCOR spectra recorded using FSLG cross polarization. Error estimates are from curve fitting and do not take direct account of experimental errors.

Sample	$\tau_{HP}$ (OH/ $PO_4^{3-}$ region) / ms	$\tau_{HP}$ ( $H_2O$ / $PO_4^{3-}$ region) / ms	$\tau_{HP}$ ( $HPO_4^{2-}$ region) / ms
64	$1.7 \pm 0.3$	$0.5 \pm 0.1$	$0.4 \pm 0.1$
124	$2 \pm 1$	$0.3 \pm 0.1$	$0.2 \pm 0.2$

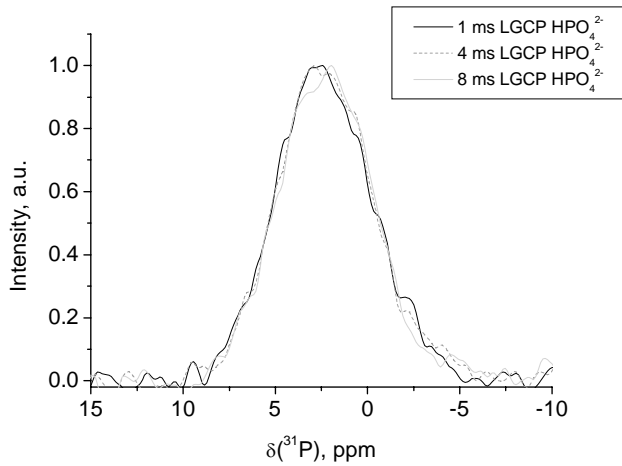
The  $^{31}P$  line shapes extracted from the two-dimensional HETCOR spectra are presented in Fig. 6.5. These are plotted for sample 27 for different  $^1H$ - $^{31}P$  FSLG mixing times for the three spectral regions indicated in Fig. 6.4. Other samples give near identical plots.



a.



b.



c.

Fig. 6.5 The  $^{31}\text{P}$  line shapes extracted from the two-dimensional FSLG HETCOR spectra for the three spectral regions defined in Fig. 6.4 OH (a), water (b) and  $\text{HPO}_4^{2-}$  (c) for sample 27 for FSLG mixing times of 1, 4 and 8 ms.

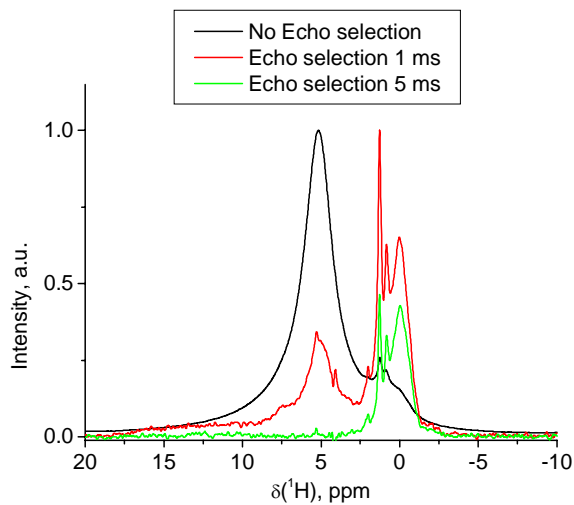


Fig. 6.6 Total suppressing of water and hydrogen phosphate signals and partial suppressing of organic matrix signals in a bone sample by Echo experiment.



Preliminary Echo experiments on nanocrystalline hydroxyapatite showed that the water and hydrogen phosphate signals can be effectively vanished from  $^1\text{H}$  spectra by increasing the delay  $\tau$  (increasing number of loops in Echo sequence), thus allowing to concentrate investigations on the mineral core rather than on both mineral core and distorted surface. The same experiment on the bone samples (Fig. 6.6) showed a high level of effectiveness of the “crystallite surface” signals suppression together with partial suppression of organic matrix signals. The broadened signal of mineral  $\text{OH}^-$  proton dephases slightly faster than in nanocrystalline hydroxyapatite sample but in 30 echo loops there is still enough magnetization left for subsequent REDOR experiments.

Echo-REDOR, Echo-CP-REDOR and Echo-REDOR-CP experiments were held to characterize the  $\text{PO}_4^{3-}\text{-OH}^-$  distributions. Example Echo-REDOR experiments for crystalline, nanocrystalline hydroxyapatite and bone samples are presented in Fig. 6.7. An obvious dependence of dephasing behaviour from the crystallite size can be noticed in the figure. Attempts to fit the bone dephasing curve on hydroxyapatite curves give time scaling factors 0.9 and 0.8 for nano- and crystalline curves, respectively. This factor includes the influence of lattice distortions and  $\text{PO}_4^{3-}$  substitutions. Both phenomena, increasing internuclear  $^1\text{H}\text{-}^{31}\text{P}$  distances and lack of dephasing atoms, lead to slower dephasing behaviour, but at the moment their roles cannot be estimated.

Performing a short CP step after the Echo-REDOR sequence allows us to select preferably the signals from the closest  $^1\text{H}\text{-}^{31}\text{P}$  spin pairs (Fig. 6.8). Comparing the resulting REDOR curve with the original dephasing curve gives additional information about interatomic distance distribution.

Hydrogen environment of phosphorus atoms in bone mineral can be studied by an Echo-CP-REDOR experiment. The experiment allows phosphorus atoms that are in spatial proximity to  $\text{OH}^-$  units to be selected and their dephasing behaviour to be studied (Fig. 6.9).

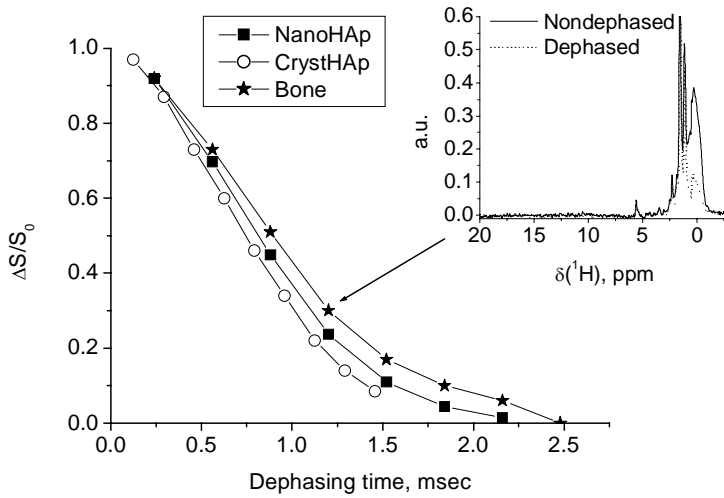


Fig. 6.7  $^1\text{H}\{^{31}\text{P}\}$  REDOR dephasing curve after Echo signal selection on  $^1\text{H}$  channel. Data points are acquired by line shape fitting. Top right – Echo filtered example spectrum for bone for 1 ms dephasing time

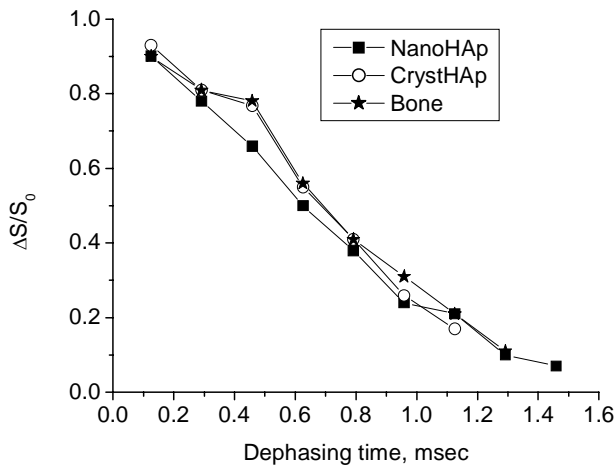


Fig. 6.8  $^1\text{H}\{^{31}\text{P}\}$  REDOR dephasing curve after Echo-REDOR-CP experiment on a bone sample compared to nanocrystalline hydroxyapatite sample. The similar dephasing behaviour strengthens the idea of similar constitution of bone mineral and (nano)crystalline hydroxyapatite.

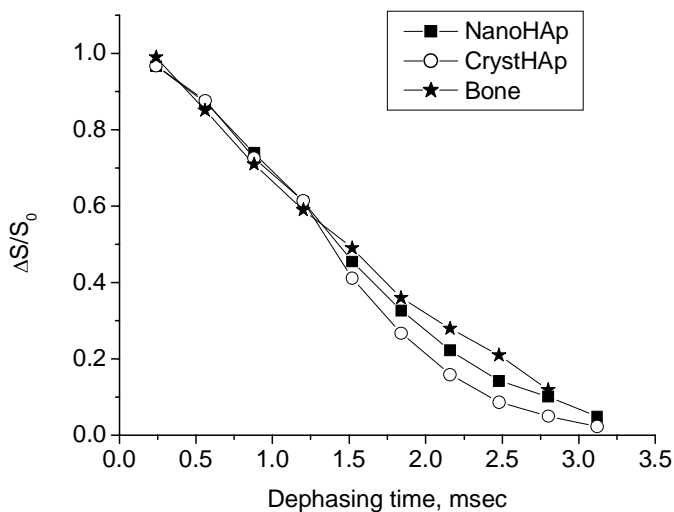
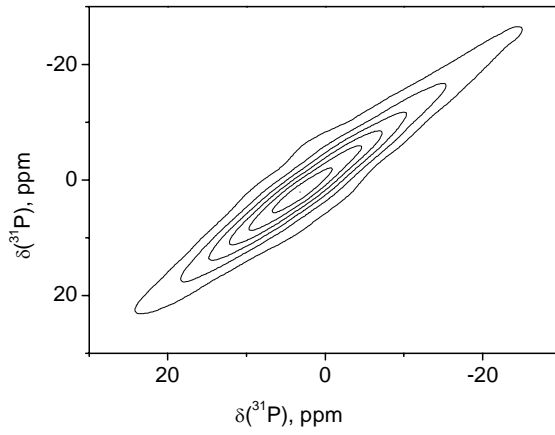
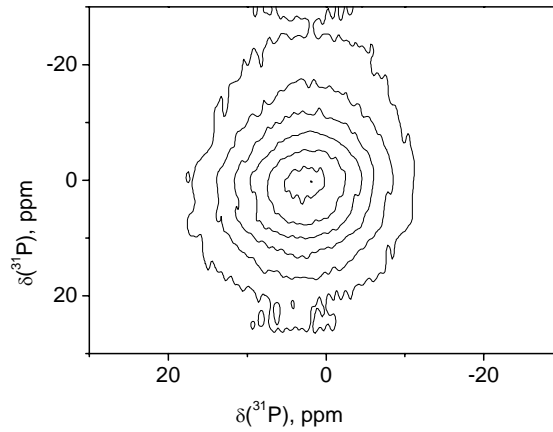


Fig. 6.9  $^{31}\text{P}\{^1\text{H}\}$  REDOR dephasing curve after Echo-CP-REDOR experiment on a bone sample compared to crystalline and nanocrystalline hydroxyapatite samples. For details see text. Data points are acquired by line shape fitting.

Two-dimensional  $^{31}\text{P}$ - $^{31}\text{P}$  correlation spectra for the samples under non-spinning conditions for mixing times of 1 ms, 10 ms, 100 ms, 1 s and 10 s at room temperature (Fig. 6.10) were undertaken to establish whether all mineral crystals are similar or whether there are populations with different species of phosphate groups.



a.



b.

Fig. 6.10  $^{31}\text{P}$ - $^{31}\text{P}$  Static Homonuclear Correlation experiment on sample 27 with correlation times 1 ms (a) and 1 s (b).

## 6.2. Results and discussion

### **Osteoarthritis and bone mineral changes**

The mineral  $^1\text{H}$  and  $^{31}\text{P}$   $T_1$  relaxation time constants for each sample have been recorded. These are shown in Table 6.2-1. It should be noted that a single  $T_1$  time constant describes the relaxation of the entire  $^1\text{H}$  spectrum within experimental error. The estimates of error are estimates of the error from fitting the experimental data points to an exponential curve. They do not take into account either noise in the experimental data nor the effects of any baseline errors (for instance) in the experimental data. Thus, from the values in Table 6.2-1, it is concluded that the  $T_1$  values for both mineral  $^1\text{H}$  and  $^{31}\text{P}$  are very similar between all samples once all sources of error are taken into account. Two methods were used for determining the  $T_1$  values: (1) direct  $T_1$  measurements, after first selecting the mineral  $^1\text{H}$  spectroscopically (which is done here using a rotor-synchronised echo; the protein  $^1\text{H}$  signals have relatively short transverse relaxation times and so the decay during the echo period, leaving only the mineral  $^1\text{H}$  signal at the end of the echo experiments), and (2) indirect measurement using cross polarization from  $^1\text{H}$  to  $^{31}\text{P}$  (which automatically selects the mineral  $^1\text{H}$ , as only these are close enough to  $^{31}\text{P}$  spins to cross polarize). In the first case, we obtain relaxation information of every  $^1\text{H}$  signal independently. In the second case, we obtain the information about  $^1\text{H}$  relaxation through the  $^{31}\text{P}$  nuclei. In general, the  $T_1$  relaxation times measured in these two ways can be different. The difference tells us about the internal structure of proton lines: if, for example,  $T_1$  relaxation measured via cross polarization to  $^{31}\text{P}$  is faster, then there are at least two components forming the  $^1\text{H}$  line and this should be taken into account when analyzing the experimental relaxation data. However,  $T_1$  values measured by methods (1) and (2) were very similar, strongly suggesting that a one-exponent analysis is sufficient.

Table 6.2-1 The  $^1\text{H}$  and  $^{31}\text{P}$   $T_1$  relaxation time constants for the bone samples used in this work. The measurement method is described in the Experimental section.

Sample	27	82	85	64	124
$^1\text{H } T_1 / \text{s}$	$1.1 \pm 0.3$	$1.1 \pm 0.2$	$1.0 \pm 0.2$	$1.1 \pm 0.2$	$1.2 \pm 0.3$
$^{31}\text{P } T_1 / \text{s}$	$244 \pm 4$	$207 \pm 3$	$213 \pm 3$	$228 \pm 3$	$206 \pm 6$

Data in Table 6.1-1 and Table 6.1-2 shows that the  $\tau_{HP}$  rate constants for each  $^{31}\text{P}$  spectral region are very similar within the limits of error for all samples studied. This, plus the similarity of the two-dimensional HETCOR spectra themselves leads to the conclusion that the mineral compositions and structures are very similar for all samples and thus joint disease has not changed the mineral structure in any way that is possible to measure here.

Furthermore, in the work, using different cross polarization contact times (100  $\mu\text{s}$  and 9 ms) yields very similar  $T_1$  behaviour, despite the fact that for a 100  $\mu\text{s}$  contact time, there is almost no signal from hydroxyapatite  $\text{OH}^-$   $^1\text{H}$  present in the spectrum and at 9 ms, almost no  $\text{HPO}_4^{2-}$  or  $\text{H}_2\text{O}$  signal contributes to the spectra. This further suggests that one exponent fitting of the experimental  $T_1$  relaxation curves may be used and, within error limits, this gave acceptable fits in every case.

### **Hydroxyapatite regions: diluted over the crystals or stoichiometric “subcrystals”?**

The spectra shown in Fig. 6.3 for the two different samples are very similar to each other for equivalent mixing times. Moreover, they are similar to those reported previously by other workers examining the mineral structure of bone from bovine and rat species [100], and bovine, rat and human [101]. Very similar spectra are found for all the other samples in this work. Results from experiments which used Hartmann-Hahn cross polarization rather than FSLG are similar also (a loss of the water signal due to spin-diffusion processes can occur in Hartmann-Hahn experiments). The latter is not surprising as  $^1\text{H}$ - $^1\text{H}$  distances in the mineral matrix are expected to be large so that at the MAS frequency (12.5 kHz), spin diffusion between  $^1\text{H}$  spins is expected to be slow on the timescale of the cross polarization

transfer and under such circumstances, the CP dynamics are similar for FSLG and Hartmann-Hahn conditions.

The more disordered region containing H<sub>2</sub>O/phosphate and HPO<sub>4</sub><sup>2-</sup> groups is ascribed to surface regions of the crystallites and the more ordered OH<sup>-</sup>/PO<sub>4</sub><sup>3-</sup> groups to a more crystalline core in the crystallites as it was shown recently for nanocrystalline hydroxyapatite in detail [93]. This is consistent with the idea that the surface regions of any crystal are expected to be more disordered due to the lack of coordination around surface ions, and/or coordination of surface ions by heterogeneous molecules from the protein matrix in the case of mineral crystals in bone. The H<sub>2</sub>O/phosphate region may arise in part or whole from matrix water bound to the surface of the mineral crystallites.

The <sup>31</sup>P line shape for the OH<sup>-</sup>/PO<sub>4</sub><sup>3-</sup> spectral region is invariant with mixing time in both the FSLG and Hartman-Hahn mixing time experiments (Fig. 6.5). This is the behaviour expected for a single-component (crystalline) system in which there is one type of PO<sub>4</sub><sup>3-</sup> in spatial proximity to one type of OH<sup>-</sup> hydroxyapatite.

The <sup>31</sup>P line shape for the H<sub>2</sub>O/phosphate region shows more complex behaviour: an initially broad <sup>31</sup>P line shape *decreases* in line width as the mixing time increases from 2 ms to 8 ms, the longest mixing time studied, for both FSLG (Fig. 6.5b) and Hartman-Hahn mixing (the latter not shown). One possible explanation for this effect is that at the longer mixing times, there is spin diffusion from H<sub>2</sub>O <sup>1</sup>H to OH<sup>-</sup> groups in the ordered hydroxyapatite regions somewhere in the experiment prior to cross polarization to <sup>31</sup>P, so that magnetization which initially started on H<sub>2</sub>O ends up on the ordered phosphate groups (and <sup>31</sup>P spins thereof) in the hydroxyapatite core of the crystallites. However, FSLG mixing does not permit spin diffusion between <sup>1</sup>H spins during the mixing period and the longest *t*<sub>1</sub> time used in the HETCOR experiment is 6 ms which from previous work [102] is too short a time for there to be significant spin diffusion between <sup>1</sup>H spins (significant spin diffusion between OH<sup>-</sup> and H<sub>2</sub>O only occurs on a timescale of 200 ms [102]). Thus, the existence of the narrowed <sup>31</sup>P line does not arise from spin diffusion between <sup>1</sup>H, but must instead arise from a second phosphate site spatially correlated with H<sub>2</sub>O which has different cross polarization dynamics to the

sites which account for the main cross polarization events at shorter mixing times. The fact that this second site does not become apparent until longer mixing times suggests that either (a) its cross polarization transfer rate constant  $\tau_{HP}$  is significantly longer, or (b) the decay constant governing the decay of the  $^{31}\text{P}$  cross polarization signal is significantly less than those for the sites which account for the majority of polarization transfer at short mixing times. Alternatively, both (a) and (b) may occur to some extent. In case (a), the conclusion would be that the  $\text{H}_2\text{O}$  from which the cross polarization is occurring for this second  $\text{H}_2\text{O}$ /phosphate site is relatively distant from the phosphate to which it cross polarizes and in case (b), that the rotating-frame spin-lattice relaxation times for the  $^{31}\text{P}$  and/or  $^1\text{H}$  involved in the cross polarization process for the second  $\text{H}_2\text{O}$ /phosphate site are significantly smaller than for other  $\text{H}_2\text{O}$ /phosphate groups with the faster cross polarization rates.

Moreover, the phosphate groups involved in this second site are (from the narrowed  $^{31}\text{P}$  line shape) more ordered than for the rapidly cross polarizing  $\text{H}_2\text{O}$ /phosphate sites. A likely explanation is that the mineral bone crystals consist of crystalline hydroxyapatite as core covered with an amorphous layer as found for nanocrystalline hydroxyapatite [16]. It must then be concluded that the water molecules are close to this interface which in turn would explain the higher degree of order of the phosphate anions due to the near hydroxyapatite structure.

Two-dimensional  $^{31}\text{P}$ - $^{31}\text{P}$  correlation (Fig. 6.10) were undertaken to establish whether all mineral crystals are similar or whether there are populations with different species of phosphate groups. At short mixing times, the exchange pattern in the two-dimensional spectrum is simply a diagonal line shape as there is essentially no spin diffusion between the  $^{31}\text{P}$  spins on this timescale. As the mixing time increases, there are increasing amounts of exchange intensity correlating different  $^{31}\text{P}$  signals, until at mixing times of 1 s and above, the exchange pattern is essentially circular, indicating that all  $^{31}\text{P}$  signals are correlated with each other. Moreover, the buildup of exchange intensity with mixing time to this position is smooth. In other words, all the  $^{31}\text{P}$  sites represented in these spectra (and therefore, also the HETCOR spectra in Fig. 6.4) exist in every crystallite in the



sample, i.e. the different  $^1\text{H}$  sites and phosphate groups inferred from the HETCOR spectra in Fig. 6.4 are not in different mineral phases in different crystallites for instance.

Detailed investigation of phosphorus environment of OH units in the bone mineral phase with Echo-REDOR and Echo-REDOR-CP techniques (Fig. 6.7 and Fig. 6.8) clearly shows that:

- dephasing behaviours of the closest P-OH pairs in bone apatite and in nano- and crystalline hydroxyapatite samples are the same
- differences in dephasing behaviours of the samples in Fig. 6.7 become obvious accounting the increasing role of lattice distortions and atoms substitutions with decreasing the crystallite sizes

Comparing the Echo-CP-REDOR experimental data for both hydroxyapatite samples and bone (Fig. 6.9) it can be concluded that there is no significant difference in dephasing behaviour of the samples. This means that  $\text{PO}_4^{3-}$  units of the bone mineral are in the same proton environment as in hydroxyapatite. Since REDOR curves contain information about dipolar couplings to all nearest neighbouring atoms, the overall conclusion can be made that the phosphorus surrounding of  $\text{OH}^-$  units and proton surrounding of  $\text{PO}_4^{3-}$  units in the mineral core of crystalline, nanocrystalline hydroxyapatites and bone is the same. Moreover, bone mineral, as well as the nanocrystalline hydroxyapatite sample, can be described with the “core+surface” model.

### 6.3. Conclusions

The molecular-level structure of the mineral in bone taken from the subchondral regions of equine joints was investigated.  $^{31}\text{P}$ - $^{31}\text{P}$  correlation and  $^1\text{H}$ - $^{31}\text{P}$  dipolar dephasing experiments showed that despite low  $\text{OH}^-$  units content they are not distributed randomly over the crystallites but form a stoichiometric hydroxyapatite phase. Heteronuclear correlation experiments with different polarization transfer time (cross polarization contact time) and several  $^1\text{H}$ - $^{31}\text{P}$  dephasing experiments

gave enough evidence to conclude that the mineral phase of all bones is similar to that of nanocrystalline hydroxyapatite and can be described with “core+surface” model.

The bone samples where there was clinical and histological evidence of OA joint disease were compared with the healthy samples. Phosphorus echo experiments showed exact coincidence of all samples. Some differences in proton echo experiments cannot be correlated with diseased samples and in common all the spectral features are the same for all samples. No differences, in error limits, were found that could be associated with the disease. This can serve as proof that the mineral phase of bone stays untouched by osteoarthritis. These results will no doubt add to the debate about how precisely OA affects underlying bone structure and strength.

## 7. Organic-mineral interface in bone

Vertebrate bone is a complex composite of organic and mineral phases conferring toughness and hardness respectively. The organic phase is a matrix of proteins, mainly collagen, and other macromolecules including proteoglycans (PG) rich in acidic glucosaminoglycans (GAG - long unbranched polysaccharides consisting of a repeating disaccharide unit). Although the relationship between the two phases must be crucial to the properties of bone in health and disease, little is known about the macromolecules stabilising the boundary. Conjecture has centred around acidic proteins. The REDOR SSNMR technique and the abundance of  $^{31}\text{P}$  nuclei within the mineral phase offer a unique probe of the atomic-level structure and composition of the interface. In practice, signals from  $^{13}\text{C}$  nuclei less than 5 to 6 Å away from phosphorus nuclei in the mineral lose coherence and decrease in intensity; nuclei closest to the phosphorus-containing phase will do this most rapidly. It was shown that the closest  $^{13}\text{C}$  nuclei to bone mineral are in carbohydrates (see Fig. 7.2 for summary schematic).

The samples used in this study are equine bone sample, equine mineralized cartilage sample, hyaline cartilage sample and equine foetal bone sample at six months gestation. All the samples were prepared and stored as described in chapter 6.

### 7.1. Experiments and discussion

The signals affected at the shortest dephasing times in the equine bone  $^{13}\text{C}\{^{31}\text{P}\}$  REDOR experiments are the distinct shoulder on the high frequency edge of the carbonyl / carboxylate signal, at approx. 182 ppm, a lower frequency element of this envelope at approx. 175 ppm, and a broad signal centred at 76 ppm (Fig. 7.2a). At longer dephasing times small effects, which are nevertheless highly reproducible between adult samples, are seen to several signals most of which are probably from proteins, including collagen. Most of the signals in the  $^{13}\text{C}$  spectrum can be assigned by reference to random coil chemical shifts of the amino acid residues constituting Type I collagen [103; 104] which unusually includes a high proportion of hydroxyproline; a standard cross polarization MAS spectrum in

Fig. 7.2b is compared with the simulation in Fig. 7.2c. The 182 ppm and 175 ppm signals are consistent with carboxylate/carbonyl carbons, but none of the common amino acids give rise to chemical shifts which approximate that of the strongly dephasing 76 ppm signal. It must therefore arise from a non-protein biomolecule, or protein carbons in a magnetically unusual environment or one affected by post-translational modification. It is unlikely to be from the  $\gamma$ -carbons of hydroxyproline (71 ppm) or  $\gamma$ -carboxyglutamate (Gla, 55 ppm). Nor can it be the  $\beta$ -carbon of phosphoserine (61 ppm) or any other covalently phosphorylated carbon because the REDOR dephasing to such a carbon would be much more rapid than that observed [64; 105]. However, it is consistent with some of the secondary alcohol carbons in pyranose sugars like those comprising the oligosaccharide component of PGs or sialoproteins [104; 106].

Connective tissue GAGs consist of variants of a few primary structural types: hyaluronic acid, keratan, often sulfated on the C6-position, chondroitin, often sulfated on the C4- and sometimes on the C6-position, and dermatan (Fig. 7.1). Bone resonances are too broad to distinguish these species, and the REDOR-dephasing macromolecules may be of one or several GAG types, sialic acids, other sugars or a combination of all three.

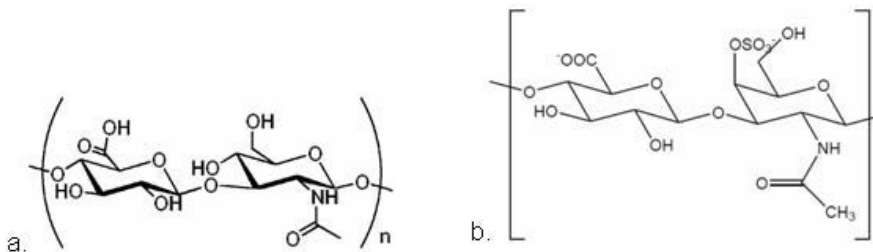


Fig. 7.1 GAG examples. Molecular structures of a) hyaluronan and b) chondroitin sulfate

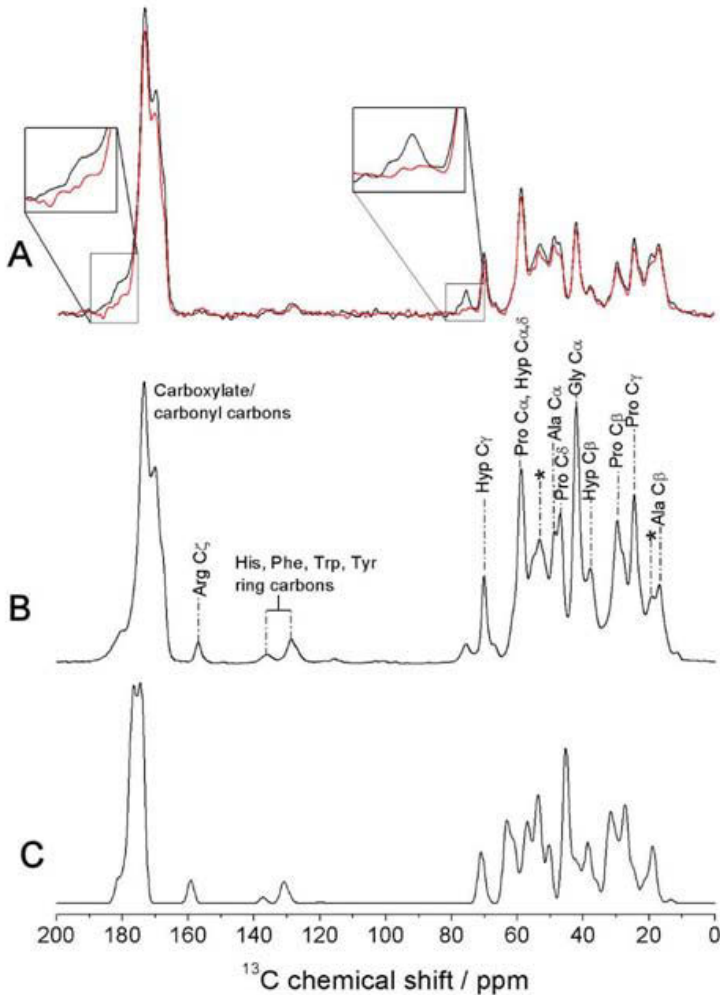


Fig. 7.2

*Solid-state NMR of bone:*

*(A) Representative  $^{13}\text{C}\{\beta^1\text{P}\}$  REDOR CPMAS spectrum of adult equine cortical bone comparing full dipolar decoupling (black trace) with the effects of reintroduction of  $^{31}\text{P}$ - $^{13}\text{C}$  coupling for 9.6 ms (red trace); the insets highlight the pronounced loss of intensity of the signals at 76 and 182 ppm.*

*(B) CPMAS spectrum of bone showing some assignments of the protein component; signals marked with asterisks are ascribable to overlapping resonances of less abundant amino acids.*

*(C) Simulated bone spectrum based on the composition of Type I collagen and the random coil  $^{13}\text{C}$  shifts of the common amino acids.*

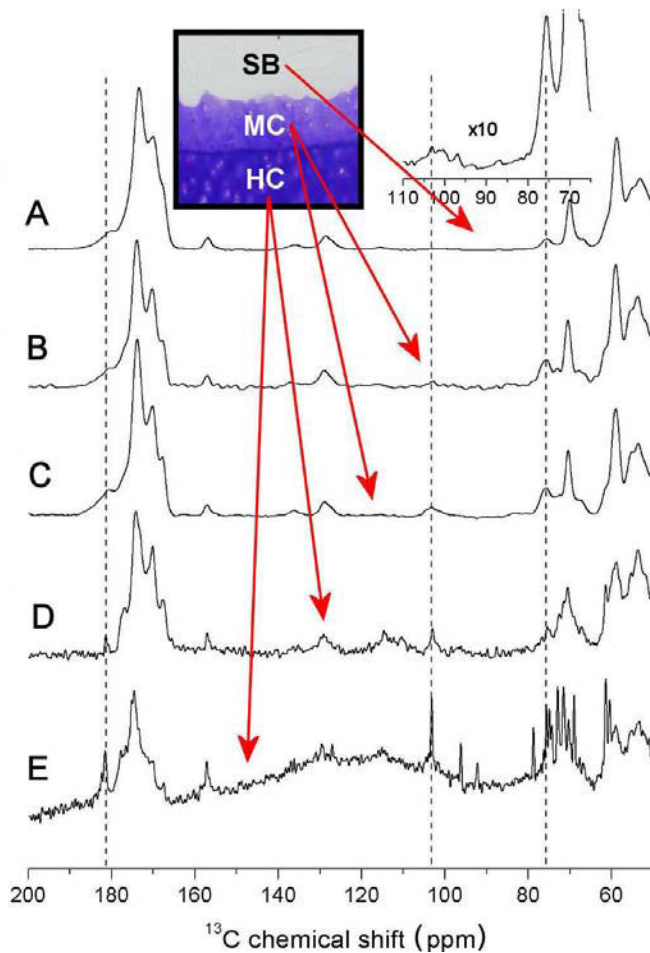


Fig. 7.3  $^{13}\text{C}$  spectra of bone-related connective tissues: (A) Adult subchondral bone (SB); 70 to 110 ppm is vertically expanded to emphasize the broad anomeric signal centred at 103 ppm. (B) Mineralized cartilage (MC) from proximal phalanx. (C) Mineralized cartilage from the radius. (D) Articular hyaline cartilage (HC) from same location as (B) (E) Hyaline cartilage observed by direct polarization MAS. Vertical dotted lines connect the signals at 76, 103, and 182 ppm which are common to the three tissue types and ascribed respectively to some of the ring, the anomeric, and the carboxylate, carbons of GAGs. There are other GAG ring signals between approx. 60 and 80 ppm. **Inset:** Histology showing toluidine blue staining (which is a semi-quantitative marker of GAG content) increasing in the same rank order as the relative intensity of the putative GAG NMR signals.

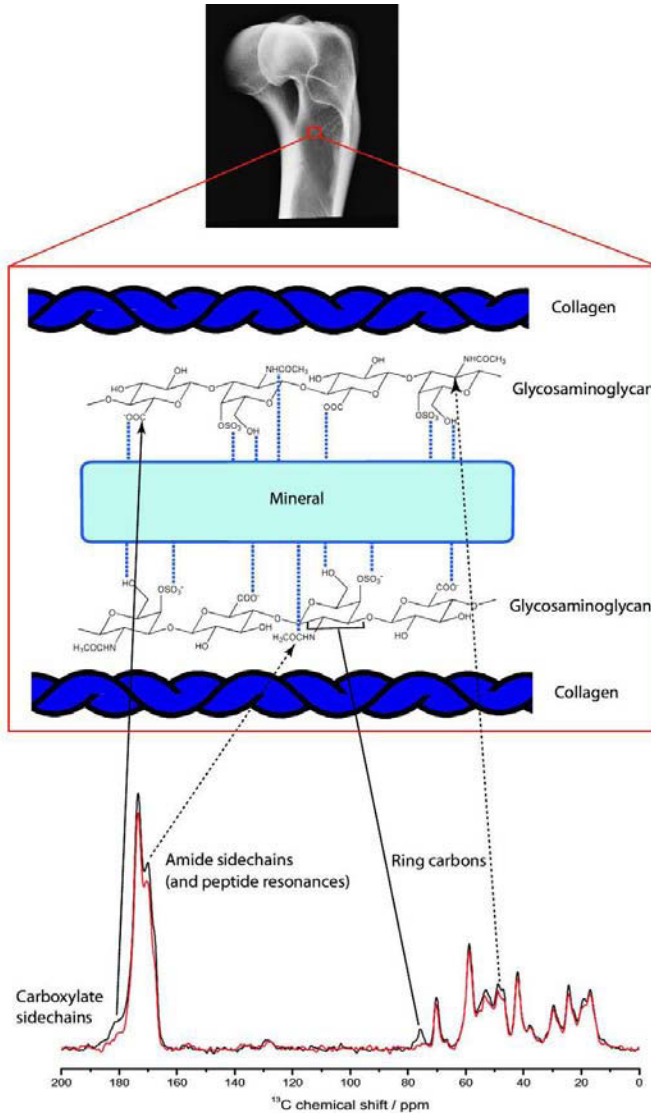


Fig. 7.4 The mineral-organic interface in bone: A schematic of the organic-mineral interactions in bone and their consequences for the SSNMR REDOR profile. Possible electrostatic interactions between GAG functional groups and the mineral surface are implied by the heavy dashed blue lines. The diagram makes no implications about the spatial relationship between GAG and the matrix of collagen triple helices.

The strongly dephasing signals were assigned by analogy with  $^{13}\text{C}$  NMR spectra from related tissues evolving, or with the potential to evolve, into bony material. Fig. 7.3 compares CPMAS spectra of adult equine bone (a) with those of equine mineralized cartilage (MC) (b & c), containing mineral essentially identical to that of bone by X-ray powder diffraction and  $^{13}\text{C}\{^{31}\text{P}\}$  REDOR itself. The 76 and 182 ppm signals are relatively more intense in mineralized cartilage than in bone; another at approx. 103 ppm, broad but nevertheless observable in bone, is more prominent in mineralized cartilage. Like 76 ppm, 103 ppm is not reconcilable with any common amino acids, but is a good match to the resonances of anomeric carbons in  $\beta$ -glycosidically linked polysaccharides. Articular hyaline cartilage (HC) shows two families of signals: one broad, therefore motionally restricted and detectable by CPMAS (Fig. 7.3d), the other sharper, therefore more mobile, and only seen with direct polarization MAS (e). Both populations show signals at 76, 103, 175 and 182 ppm consistent with GAGs. Those around 76 and 103 ppm also occur in aqueous solutions of GAG polysaccharides like chondroitin sulfates [106]. The relative prominence of the GAG signals increases from bone, with least abundant GAG, through mineralized cartilage, to hyaline cartilage, in which GAG is most abundant. If the 76 ppm signal were an amino acid resonance strongly shifted by mineral binding, its intensity would scale with that of the other protein signals, and not with the 103 ppm sugar anomeric signal. It should also become more, not less, prominent in bone than it is in MC. Neither is the case.

Thus REDOR shows that the biomolecules most intimately associated with bone mineral are sugars, quite probably GAGs, and not proteins at all.

*In vivo* the collagen fibre scaffold directs bone mineralization [107; 108] to periodic gaps in the collagen topography which accommodate plate-shaped mineral particles about 25 to 35 nm long and wide, and 2.5 to 3.5 nm thick. Later, more mineral inserts between the collagen bundles, so it is natural to enquire after any possible direct interaction of collagen itself with nascent mineral. The REDOR on a single sample of equine foetal bone at six months gestation has been performed. Even at long  $^{31}\text{P}$ - $^{13}\text{C}$  recoupling times the only dephasing signals are the familiar ones at 76 and 182 ppm, and others around 48 ppm which could be from ring carbons next to nitrogen in sugar amides, and which also dephase consistently in adult bone. There are no effects to other signals ascribable to protein.



Although this needs confirmation on more samples, it has been proposed that it reflects young mineral, formed in the hole zones of the collagen network, which only contacts GAGs. Later in life, mineral inserts in the interstices between the collagen fibrils and produces, and REDOR dephasing of both GAG and (more weakly) collagen signals occurs.

Proteins rich in serine (often phosphorylated) and acidic residues like osteopontin [109] and osteocalcin [110] influence biomineralization. While many, like the small leucine-rich repeat proteins (SLRPs), are glycosylated, the polysaccharide components have not received as much attention as the polypeptides to which they are attached. For instance, osteocalcin has been proposed as a mineral template [111]. In general proteins are uppermost in theories about biopolymer-directed mineralization, in spite of multifarious evidence that GAGs are important in bone formation. Mutations affecting the production of PGs [112] and GAGs [113; 114] produce abnormally massive, crystalline bone mineral, while sulfated GAGs profoundly influence calcium phosphate precipitation *in vitro* [115; 116]. Intimate associations between bone mineral and chondroitin and dermatan sulfate PGs have been demonstrated immunohistochemically [117]. The SSNMR demonstration that the biomolecules most closely bound to bone mineral are polysaccharides confirms their central role in biomineralization (Fig. 7.4).

Less is known about the molecular architecture of the GAGs and their relationships with other macromolecules in bone than in other connective tissue [118]. Chains of chondroitin or dermatan sulfates are attached to SLRPs which can also bind to collagen. Although the 3D structures of some unglycosylated SLRP polypeptides are known there is little detailed information about their interactions with collagen [119; 120]; modelling predicts that the pendant glycan chains point away from potential collagen-binding surfaces on the SLRPs. Perhaps some SLRPs help orienting GAG chains, and thus ultimately mineral particles, relative to collagen fibrils in mineralizing bone.

Macromolecules [116; 121] modulate biomineralization by directing formation of amorphous inorganic phases and preventing uncontrolled crystallization [122-124] which predisposes to bone weakness [125; 126]. Thus, moderating crystallization

is a vital element of the formation of healthy bone, a process to which the GAGs could be a key. Some can adopt regular secondary structures governed by inter-residue non-covalent interactions, like the extended ribbon-like [127] conformation of calcium chondroitin sulfate A [128]. GAGs present numerous regularly spaced recognition points for directing the growth of hydrated calcium phosphates from dissolved parent ions: polysaccharide sulfates and carboxylates can chelate  $\text{Ca}^{2+}$ , and N-acetylamido and hydroxyl groups can hydrogen bond with protonated  $\text{PO}_4^{3-}$ , water, and  $\text{OH}^-$ . The GAGs seem better suited to the initiation, propagation and control of the mineralization process than hydrophobic collagen or small globular proteins.

### 7.2. Conclusions

The organic-mineral interface in vertebrate bones was studied by REDOR NMR experiments to find out which macromolecules stabilize the organic-mineral boundary. It was noticed that one of the signals that dephases most rapidly is a broad signal at 76 ppm  $^{13}\text{C}$  which is ascribed to glucoseaminoglycans. It was shown that the signal intensity, and consequently the relative amount of GAG in bone, increases from subchondral bone to mineralized cartilage and to hyaline cartilage. Also no dephasing occurs to most of the protein signals even with long  $^{13}\text{C}$ - $^{31}\text{P}$  recoupling times for foetal bones. This leads to the conclusion that polysaccharides, not proteins, are closer to the mineral phase and thus have greater influence on mineral deposition, bone remodelling and other biomineralization processes. This idea is strengthened by studies of diseased bones that are poor in GAGs and produce abnormal bone mineralization.

This demonstration that sugars, not proteins, form the interface between the organic and mineral components fundamentally alters an accepted concept of bone structural biology. This could exert a major impact on the management of bone disorders by directing different therapeutic approaches, perhaps based on modulation of GAG metabolism. It may also offer new disease biomarkers for diagnosis in the clinic, and evaluating experimental treatments in the laboratory.

## 8. Conclusions and outlook

A new approach named “*Solid-state NMR spectroscopy using the lost I spin magnetization in polarization transfer experiments*” has been developed. It has been shown that in CP experiments the transferred I spin magnetization from abundant nuclei, which is normally lost when detecting the S spin magnetization, can be used for spectroscopy. This transferred part of the I spin magnetization can easily be “recovered” by taking the difference between two scans without, and with, polarization transfer.

This simple tactic enables a wide range of useful experiments. Firstly, this 1D signal is equivalent to the entire sum projection of the indirect dimension of 2D heteronuclear experiments without incrementation of the indirect dimension. As it can be employed in any n-dimensional experiment it means a reduction of the time dimensions by one. Further, this experiment is ideal for spectral editing purposes. Any kind of spin manipulation during the 2D evolution period and any polarization transfer methods can be applied, thus making the experiment applicable for a number of different tasks. Due to the unique signal editing features, the most important application is in the investigation of interfaces of synthetic and natural organic-inorganic composite materials like bone.

A detailed investigation of nanocrystalline hydroxyapatite core was made to prove that proton environment of the phosphates units and phosphorus environment of hydroxyl units are the same as in highly crystalline hydroxyapatite sample. For this,  $^1\text{H}\{^{31}\text{P}\}$  and  $^{31}\text{P}\{^1\text{H}\}$  REDOR experiments were provided. Proposed Echo-CP-REDOR and Echo-REDOR-CP modifications were applied to select hydroxyl and phosphate groups only in mineral core. Obtained results showed excellent coincidence of the  $^1\text{H}\{^{31}\text{P}\}$  and  $^{31}\text{P}\{^1\text{H}\}$  REDOR dephasing curves of nanocrystalline sample with those of highly crystalline sample, thus leading to conclusion that  $\text{OH}^-$  and  $\text{PO}_4^{3-}$  groups are not randomly distributed but form well defined hydroxyapatite crystal structure.

It was shown that X-ray diffraction methods usually do not detect the surface layer due to its amorphous nature. Very accurate measurements combined with high

precision diffractogram evaluation are crucial to separate the baseline signal from the extremely broad peaks of the disordered surface. It was found that the surface of the hydroxyapatite nanocrystals is not completely disordered, as it was suggested before, but resembles the hydroxyapatite structure with  $\text{HPO}_4^{2-}$  (and some  $\text{CO}_3^{2-}$ ) groups instead of  $\text{PO}_4^{3-}$  groups and water instead of  $\text{OH}^-$  groups.

Structural investigations were performed on bone mineral crystals from the subchondral regions of equine joints where there was clinical and histological evidence of osteoarthritis. No differences, in error limits, were found that could be associated with the disease. This can serve as a proof that the mineral phase of bone remains unaffected by osteoarthritis. A detailed investigation of the mineral crystalline core using dipolar dephasing experiments showed an excellent agreement with investigations of a nanocrystalline hydroxyapatite sample thus proving the theory that hydroxyapatite forms the core of the bone mineral crystallites surrounded by disordered hydroxyapatite-like structures (paper in preparation). These results will no doubt add to the debate about how precisely OA affects underlying bone structure and strength.

The organic-mineral interface of bone was studied in order to clarify which organic molecules are in the closest spatial proximity to the bone mineral phase and to investigate the influence of the organic matrix on the mineral formation.  $^{13}\text{C}\{^{31}\text{P}\}$  REDOR experiments for interatomic distance determination showed remarkable dephasing of the signals at 182, 175 and 76 ppm ( $^{13}\text{C}$ ). Whereas the 182 ppm and 175 ppm signals are consistent with carboxylate/carbonyl carbons possibly belonging to proteins, no common amino acid gives rise to chemical shifts in the region of the strongly REDOR-perturbed 76 ppm signal. It must therefore arise from a non-protein biomolecule or protein carbons in a magnetically unusual environment.

However, the chemical shift of 76 ppm is consistent with some of the secondary alcohol carbons in pyranose sugars like those comprising the polysaccharide component of proteoglycans or sialoproteins. The same experiment performed on foetal bone,  $^{13}\text{C}$  CP experiments of mineralized cartilage and hyaline cartilage together with data from the literature strengthen the idea that most probably these

---

peaks belong to a glycosaminoglycan rather than to a protein. This result is of key importance for distinguishing between protein-mediated biomineralization and polysachharide-mediated biomineralization models.

### **Future work**

The results of the present work open new perspectives and set new directions for biomineral investigations. Comparative studies on materials which mimic bone mineral, and authentic bone apatite, could reveal new methods of biomaterial synthesis which will contribute to bone disease therapy and bone reconstruction and regeneration after fracture. It can be investigated how is bone mineralized during life, what changes are characteristic of diseased bone, and how does this knowledge contribute to healing and preventing bone disease.

## 9. Appendix

### 9.1. Abbreviation list

ACP – amorphous calcium phosphate

BSP – bone sialoprotein

CDHA – calcium-deficient hydroxyapatite

CP – cross polarization

CPMAS – cross polarization with magic angle sample spinning

CW – continuous wave decoupling

DTA – differential thermal analysis

DXA – Dual energy X-ray absorptiometry

EXAFS – Extended X-ray Absorption Fine Structure

FSLG-CP – frequency switched Lee-Goldburg cross polarization

FTIR – Fourier transformed infrared spectroscopy

HC – hyaline cartilage

GAG – glucosaminoglycan

HAp – hydroxyapatite

HETCOR – heteronuclear correlation

LG-CP – Lee-Goldburg cross polarisation

MAS – magic angle sample spinning

MC – mineralized cartilage

MS – mass spectrometry

NanoHAp – nanocrystalline hydroxyapatite

NCP – noncollagenous matrix proteins

NMR – nuclear magnetic resonance

OA – osteoarthritis

PMLG – phase modulated Lee-Goldburg decoupling

PG – proteoglycan

PP – phosphophoryn

REDOR – rotational echo double resonance

REPT –recoupled polarization transfer

RF – radiofrequency  
 RSECHO – rotor-synchronized spin-echo  
 SLRP – small leucine-rich repeat proteins  
 SSNMR – solid-state nuclear magnetic resonance  
 TEM – transmission electron microscopy  
 TG – thermogravimetry  
 TPPM – two-pulse phase-modulated decoupling  
 w-PMLG – windowed phase modulated Lee-Goldburg decoupling  
 XRD – X-ray diffraction

## 9.2. Experimental parameters

All NMR experiments were performed at Bruker AVANCE 600 (BAM, Berlin) and Bruker Avance 400 (University of Cambridge, Cambridge) spectrometers. The probeheads used were Bruker widebore 4 mm triple- or 7 mm double-channel. The Magic Angle Sample Spining was set using KBr sample. Only original Bruker zirconium dioxide rotors were used for the measurements.

The following samples and values were used for calibration of the chemical shift axes:

<sup>1</sup> H	Adamantan (CH line), relative to Tetramethylsilane.....	1.78 ppm
<sup>13</sup> C	Adamantain (CH line), relative to Tetramethylsilane.....	38.5 ppm
	Glycin (carboxyl group), relative to Tetramethylsilane.....	176.4 ppm
<sup>31</sup> P	Hydroxyapatite, relative to 85 w.% H <sub>3</sub> PO <sub>4</sub> .....	2.3 ppm

All the experimental data were processed on Bruker XWinNMR™ 1.1 or Bruker TopSpin™ 1.3. All the graphs are plotted in Origin 6.1G™.

**Direct detection of the indirect dimension of a standard 2D HETCOR**2D  $^1\text{H}$ - $^{31}\text{P}$  heteronuclear correlation experiments

Sample.....	Nanocrystalline hydroxyapatite
$^1\text{H}$ frequency .....	600 MHz
$^{31}\text{P}$ frequency.....	243 MHz
Probehead.....	Triple
Rotor.....	4 mm, central 1/3 filled with the sample, the rest is filled with teflon film
Repetition time.....	2 s
Rotation speed.....	12.5 kHz
$^1\text{H}$ 90° pulse length....	3 $\mu\text{s}$ (83 kHz)
CP contact time.....	0.1-9.9 ms
Decoupling.....	TPPM

## "two-step" experiments

Sample.....	Nanocrystalline hydroxyapatite, O-phospho-L-serine
$^1\text{H}$ frequency .....	600 MHz
$^{31}\text{P}$ frequency.....	243 MHz
Probehead.....	Triple
Rotor.....	4 mm, central 1/3 filled with the sample, the rest is filled with teflon film
Repetition time.....	2 s
Rotation speed.....	12.5 kHz
$^1\text{H}$ 90° pulse length....	3 $\mu\text{s}$ (83 kHz)
CP contact time.....	0.1-9.9 ms
Decoupling.....	TPPM

**Nanocrystalline hydroxyapatite: NMR and XRD structural investigations**2D  $^1\text{H}$ - $^{31}\text{P}$  heteronuclear correlation experiment

Sample.....	Nanocrystalline hydroxyapatite
$^1\text{H}$ frequency .....	600 MHz
$^{31}\text{P}$ frequency.....	243 MHz
Probehead.....	Triple



Rotor.....	4 mm, central 1/3 filled with the sample, the rest is filled with teflon film
Repetition time.....	2 s
Rotation speed.....	12.5 kHz
<sup>1</sup> H 90° pulse length....	3 μs (83 kHz)
CP contact time.....	2 ms
Decoupling.....	TPPM

#### <sup>1</sup>H single pulse experiments

Sample.....	Nanocrystalline hydroxyapatite, crystalline hydroxyapatite
<sup>1</sup> H frequency .....	600 MHz
Probehead.....	Triple
Rotor.....	4 mm, central 1/3 filled with the sample, the rest is filled with teflon film
Repetition time.....	2 s
Rotation speed.....	12.5 kHz
<sup>1</sup> H 90° pulse length....	3 μs (83 kHz)

#### “two-step” experiments

Sample.....	Nanocrystalline hydroxyapatite, crystalline hydroxyapatite
<sup>1</sup> H frequency .....	600 MHz
<sup>31</sup> P frequency.....	243 MHz
Probehead.....	Triple
Rotor.....	4 mm, central 1/3 filled with the sample, the rest is filled with teflon film
Repetition time.....	2 s
Rotation speed.....	12.5 kHz
<sup>1</sup> H 90° pulse length....	3 μs (83 kHz)
CP contact time.....	0.1-9.9 ms
Decoupling.....	TPPM

$^{31}\text{P}\{^1\text{H}\}$  REDOR experiments

Sample.....	Nanocrystalline hydroxyapatite, crystalline hydroxyapatite
$^1\text{H}$ frequency .....	600 MHz
$^{31}\text{P}$ frequency.....	243 MHz
Probehead.....	Triple
Rotor.....	4 mm, central 1/3 filled with the sample, the rest is filled with teflon film
Repetition time.....	2 s
Rotation speed.....	12.5 kHz
$^1\text{H}$ 90° pulse length....	3 $\mu\text{s}$ (83 kHz)
CP contact time.....	2 ms
Dephasing times.....	240 $\mu\text{s}$ – 1 ms
Decoupling.....	TPPM

Echo- $^1\text{H}\{^{31}\text{P}\}$ REDOR and Echo- $^1\text{H}\{^{31}\text{P}\}$ REDOR-CP experiments

Sample.....	Nanocrystalline hydroxyapatite, crystalline hydroxyapatite
$^1\text{H}$ frequency .....	600 MHz
$^{31}\text{P}$ frequency.....	243 MHz
Probehead.....	Triple
Rotor.....	4 mm, central 1/3 filled with the sample, the rest is filled with teflon film
Repetition time.....	2 s
Rotation speed.....	12.5 kHz
$^1\text{H}$ 90° pulse length....	3 $\mu\text{s}$ (83 kHz)
Echo-selection delay..	5 ms
CP contact time.....	2 ms
Dephasing times.....	240 $\mu\text{s}$ – 1 ms
Decoupling.....	TPPM

The precipitated and dried calcium phosphate powder was preliminarily analysed by Epple *et al.* by X-ray diffraction (XRD; Bruker AXS D8 Advance;  $\text{CuK}\alpha$ ) [91] in default geometry.

Detailed XRD measurements for background signal analysis were performed on a Bruker-AXS D-5000 diffractometer in Bragg-Brentano geometry, using an 1.0 mm aperture slit, a 0.1 mm receiving slit, a sample spinner (0 or 15 rpm), a curved graphite monochromator in the diffracted beam, a scintillation counter and  $\text{CuK}\alpha_{1,2}$  radiation with 40 kV x 30 mA.

The specimens used for these XRD measurements had a diameter of 24 mm and a thickness of about 0.2 mm and were placed on a "background-free" sample holder (polished silicon monocrystal). The amount of the analysed powder was 68 micrograms of the nanocrystalline HAp and 166 micrograms of the crystalline HAp.

Data were collected in the  $2\Theta$ -range from  $5^\circ$  to  $120^\circ$  in steps of  $0.05^\circ$  using 60 seconds per step for the nanocrystalline HAp and in steps of  $0.02^\circ$  using 30 seconds per step for the crystalline HAp. For the analysis of the diffraction pattern the DiffracPLUS (Bruker-AXS, Karlsruhe, Germany; see [www.bruker-axs.de](http://www.bruker-axs.de)) and the BGMN (Bergmann, J.; distributed by GE Inspection Technologies, Ahrensburg, Germany) packages were used.

XRD simulations were performed in Accelrys MaterialStudio ([www.accelrys.com/products/mstudio/](http://www.accelrys.com/products/mstudio/)) package in Max Planck Institute, Golm.

### Mineral phase of bone characterization

#### $^1\text{H}$ single pulse experiments

Sample.....	Equine bone samples 27, 82, 85
$^1\text{H}$ frequency .....	600 MHz
Probehead.....	Triple
Rotor.....	4 mm, fully filled
Repetition time.....	100 $\mu\text{s}$ - 10 s
Rotation speed.....	12.5 kHz
$^1\text{H}$ $90^\circ$ pulse length....	3 $\mu\text{s}$ (83 kHz)

<sup>31</sup>P single pulse experiments

Sample.....	Equine bone samples 27, 82, 85
<sup>31</sup> P frequency .....	243 MHz
Probehead.....	Triple
Rotor.....	4 mm, fully filled
Repetition time.....	1-1880 s
Rotation speed.....	12.5 kHz
<sup>31</sup> P 90° pulse length...	5 μs (50 kHz)

2D <sup>1</sup>H-<sup>31</sup>P heteronuclear correlation experiment

Sample.....	Equine bone samples 27, 64, 82, 85, 124
<sup>1</sup> H frequency .....	600 MHz
<sup>31</sup> P frequency.....	243 MHz
Probehead.....	Triple
Rotor.....	4 mm fully filled
Repetition time.....	2 s
Rotation speed.....	12.5 kHz
<sup>1</sup> H 90° pulse length....	3 μs (83 kHz)
CP contact time.....	1-8 ms (HHCP and LGCP used)
Decoupling.....	TPPM

<sup>1</sup>H Echo-selection experiments

Sample.....	Equine bone samples 27, 82, 85
<sup>1</sup> H frequency .....	600 MHz
Probehead.....	Triple
Rotor.....	4 mm, central 1/3 filled with the sample, the rest is filled with teflon film
Repetition time.....	100 μs - 10 s
Rotation speed.....	12.5 kHz
<sup>1</sup> H 90° pulse length....	3 μs (83 kHz)
<sup>1</sup> H 180° echo pulse length.....	6 μs (83 kHz)
Echo delay.....	0 – 5 ms

$^{31}\text{P}\{^1\text{H}\}$  REDOR experiments

Sample.....	Equine bone sample 27
$^1\text{H}$ frequency .....	600 MHz
$^{31}\text{P}$ frequency.....	243 MHz
Probehead.....	Triple
Rotor.....	4 mm, central 1/3 filled with the sample, the rest is filled with teflon film
Repetition time.....	2 s
Rotation speed.....	12.5 kHz
$^1\text{H}$ 90° pulse length....	3 $\mu\text{s}$ (83 kHz)
CP contact time.....	2 ms
Dephasing times.....	240 $\mu\text{s}$ – 1 ms
Decoupling.....	TPPM

Echo- $^1\text{H}\{^{31}\text{P}\}$ REDOR and Echo- $^1\text{H}\{^{31}\text{P}\}$ REDOR-CP experiments

Sample.....	Equine bone sample 27
$^1\text{H}$ frequency .....	600 MHz
$^{31}\text{P}$ frequency.....	243 MHz
Probehead.....	Triple
Rotor.....	4 mm, central 1/3 filled with the sample, the rest is filled with teflon film
Repetition time.....	2 s
Rotation speed.....	12.5 kHz
$^1\text{H}$ 90° pulse length....	3 $\mu\text{s}$ (83 kHz)
Echo-selection delay..	5 ms
CP contact time.....	2 ms
Dephasing times.....	240 $\mu\text{s}$ – 1 ms
Decoupling.....	TPPM

2D  $^{31}\text{P}$ - $^{31}\text{P}$  homonuclear correlation experiment

Sample.....	Equine bone samples 27
$^1\text{H}$ frequency .....	400 MHz
$^{31}\text{P}$ frequency.....	162 MHz
Probehead.....	Dual
Rotor.....	4 mm central 1/3 filled with the sample, the rest is filled with teflon film
Repetition time.....	2 s
Rotation speed.....	12.5 kHz
$^1\text{H}$ 90° pulse length....	3 $\mu\text{s}$ (83 kHz)
$^{31}\text{P}$ 90° pulse length...	2.05 $\mu\text{s}$ (122 kHz)
CP contact time.....	4 ms
Total evolution time....	2.13 ms
Decoupling.....	TPPM

**Organic-Mineral interface in bone** $^{13}\text{C}\{^{31}\text{P}\}$  REDOR experiments

Sample.....	equine bone sample, equine mineralized cartilage sample and equine foetal bone sample
$^1\text{H}$ frequency .....	400 MHz
$^{13}\text{C}$ frequency.....	101 MHz
$^{31}\text{P}$ frequency.....	163 MHz
Probehead.....	Triple
Rotor.....	4 mm, central 1/3 filled with the sample, the rest is filled with teflon film
Repetition time.....	2 s
Rotation speed.....	12.5 kHz
$^1\text{H}$ 90° pulse length....	3 $\mu\text{s}$ (83 kHz)
$^1\text{H}$ - $^{31}\text{P}$ CP contact time.....	2.5 ms
Dephasing times.....	1.6 ms – 41 ms
Decoupling.....	TPPM

$^1\text{H}$ - $^{13}\text{C}$  CP experiments

Sample.....	equine bone sample, equine mineralized cartilage sample, hyaline cartilage sample and equine foetal bone sample
$^1\text{H}$ frequency .....	400 MHz
$^{13}\text{C}$ frequency.....	101 MHz
Probehead.....	Triple
Rotor.....	4 mm, central 1/3 filled with the sample, the rest is filled with teflon film
Repetition time.....	2 s
Rotation speed.....	12.5 kHz
$^1\text{H}$ 90° pulse length....	3 $\mu\text{s}$ (83 kHz)
$^1\text{H}$ - $^{31}\text{P}$ CP contact	
time.....	2.5 ms
Decoupling.....	TPPM

## 10. Literature

- [1] A. Veis, Mineralization in organic matrix frameworks, *Reviews in Mineralogy and Geochemistry*, Mineralogical Society of America, Washington, DC, USA, 2003, pp. 249-289.
- [2] A. Abragam, *The Principles of Nuclear Magnetism*, Oxford University Press, London, 1961.
- [3] K. Schmidt-Rohr, and H.W. Spiess, *Multidimensional Solid-State NMR and Polymers*, Academic Press, London, 1994.
- [4] S.R. Hartmann, and E.L. Hahn, Nuclear Double Resonance in the Rotating Frame, *Phys. Rev.* 128 (1962) 2042-2053.
- [5] R.R. Ernst, W.P. Aue, and E. Bartholdi, Two-dimensional spectroscopy. Application to nuclear magnetic resonance, *J. Chem. Phys.* 64 (1975) 2229-2246.
- [6] T. Gullion, Introduction to Rotational-Echo Double-Resonance NMR, *Concepts Magn. Reson.* 10 (1998) 277-289.
- [7] S. Maltsev, and C. Jäger, Solid-state NMR spectroscopy using the lost I spin magnetization in polarization transfer experiments, *Solid State Nuclear Magnetic Resonance* in press (2007).
- [8] S. Lees, A Mixed Packing Model for Bone-Collagen, *Calcified Tissue International* 33 (1981) 591-602.
- [9] P.U.P.A. Gilbert, M. Abrecht, and B.H. Frazer, *The Organic-Mineral Interface in Biominerals*, *Reviews in Mineralogy and Geochemistry*, Mineralogical Society of America, Washington, DC, USA, 2005, pp. 157-185.
- [10] A.S. Mount, A.P. Wheller, R.P. Paradkar, and D. Snider, Hemocyte-mediated shell mineralisation in the eastern oyster., *Science* 304 (2004) 297-300.
- [11] H.A. Lowenstam, Minerals formed by organisms., *Science* 211 (1981) 1126-1131.
- [12] S. Mann, *Biomineralization: Principles and Concepts in Bioinorganic Materials Chemistry*, Oxford University Press, Oxford, UK, 2001.
- [13] E.W.d.V.-d. Jong, and J.P.M.d. Vrind, Algal Deposition of Carbonates and Silicates, *Reviews in Mineralogy*, Mineralogical Society of America, Washington, DC, USA, 1997, pp. 267-307.
- [14] Y. Kitano, N. Kanamori, and A. Tokuyama, Effects of organic matter on solubilities and crystal form of carbonates., *Am Zoologist* 9 (1969) 681-688.



- 
- [15] L.C. Chow, and E.D. Eanes, Octacalcium Phosphate, KARGER, Gaithersburg, Md, 2001.
- [16] C. Jäger, T. Welzel, W. Meyer-Zaika, and M. Epple, A solid-state NMR investigation of the structure of nanocrystalline hydroxyapatite, *Magnetic Resonance in Chemistry* 44 (2006) 573-580.
- [17] T. Welzel, W. Meyer-Zaika, and M. Epple, Continuous preparation of functionalised calcium phosphate nanoparticles with adjustable crystallinity, *Chemical Communications Articles* (2004) 1204-1205.
- [18] N. Groom, Solid-state nuclear magnetic resonance studies of heterogenous materials, Downing college, University of Cambridge, Cambridge, 2005.
- [19] K.A. Piez, and B.L. Trus, A new model for packing of type-I collagen molecules in the native fibril, *Bioscience Reports* 1 (1981) 801-810.
- [20] S. Gajjerman, K. Narayanan, J. Hao, C. Qin, and A. George, Matrix Macromolecules in Hard Tissues Control the Nucleation and Hierarchical Assembly of Hydroxyapatite, *The Journal of Biological Chemistry* 282 (2006) 1193-1204.
- [21] J. Bradt, M. Mertig, A. Teresiak, and W. Pompe, *Chem. Mater.* 11 (1999) 2694-2701.
- [22] M.J. Olszta, E.P. Douglas, and L.B. Gower, Intrafibrillar Mineralization of Collagen using a Liquid-Phase Mineral Precursor, *Molecular Materials and Biomaterials* 774 (2003).
- [23] G.K. Hunter, M.D. Grynbas, P.-T. Cheng, and K.P.H. Pritzker, Effect of glycosaminoglycans on calcium pyrophosphate crystal formation in collagen gels, *Calcified Tissue International* 41 (1986) 164-170.
- [24] S.-H. Rhee, and J. Tanaka, Effect of Chondroitin Sulfate on the Crystal Growth of Hydroxyapatite, *Journal of the American Ceramic Society* 83 (2000) 2100-2102.
- [25] G.K. Hunter, P.V. Hauschka, A.R. Poole, L.C. Rosenberg, and A.H. Goldberg, Nucleation and inhibition of hydroxyapatiteformation by mineralized tissue proteins., *Biochemical Journal* (1996) 59-64.
- [26] W. Traub, T. Arad, and S. Weiner, Growth of mineral crystals in turkey tendon collagen fibers., *Connective Tissue Research* 28 (1992) 99-111.
- [27] W. Traub, T. Arad, and S. Weiner, Three-dimensional ordered distribution of crystal in turkey tendon collagen fibers, *Proceedings of the National Academy of Sciences of the United States of America* 86 (1989) 9822-9826.
- [28] G.K. Hunter, M.S. Poitras, T.M. Underhill, M.D. Grynbas, and H.A. Goldberg, Induction of collagen mineralization by a bone sialoprotein-decorin chimeric protein, *Journal of biomedical materials research* 55 (2001) 496-502.

- [29] M.E. Roy, S.K. Nishimoto, J.Y.R. JY, S.K. Bhattacharya, J.S. Lin, and G.M. Pharr, Correlations between osteocalcin content, degree of mineralization, and mechanical properties of *C. carpio* rib bone., *Journal of biomedical materials research* 54 (2001) 547-553.
- [30] H. Claassen, and J. Werner, Gender-specific distribution of glycosaminoglycans during cartilage mineralization of human thyroid cartilage, *Journal of Anatomy* 205 (2004) 371-380.
- [31] S.L. Lee, A. Veis, and T. Glonek, Dentin phosphoprotein: an extracellular calcium-binding protein., *Biochemistry* 16 (1977) 2971-2979.
- [32] W.P. Aue, A.H. Roufosse, M.J. Glimcher, and R.G. Griffin, Solid-state Phosphorus-31 Nuclear Magnetic Resonance Studies of Synthetic Solid Phases of Calcium Phosphate: Potential Models of Bone Mineral, *Biochemistry* 23 (1984) 6110-6114.
- [33] W.P. Rockwell, J.S. Waugh, and J.P. Yesinowski, High-resolution variable-temperature phosphorus-31 NMR of solid calcium phosphates, *J. Am. Chem. Soc.* 102 (1980) 2637-2643.
- [34] A.H. Roufosse, W.P. Aue, J.E. Roberts, M.J. Glimcher, and R.G. Griffin, Investigation of the Mineral Phases of Bone by Solid-state Phosphorus-31 Magic Angle Sample Spinning Nuclear Magnetic Resonance, *Biochemistry* 23 (1984) 6115-6120.
- [35] K. BESHAN, C. REY, M.J. GLIMCHER, M. SCHIMIZU, and R.G. GRIFFIN, Solid State Carbon-13 and Proton NMR Studies of Carbonate-Containing Calcium Phosphates and Enamel, *JOURNAL OF SOLID STATE CHEMISTRY* 84 (1989) 71-81.
- [36] R.A. Santos, R.A. Wind, and C.E. Bronnimann, 1H CRAMPS and 1H-31P HETCOR experiments on bone, bone mineral, and model calcium phosphate phases, *Journal of Magnetic Resonance B* 105 (1994) 183-187.
- [37] A. Kafak, D. Chmielewski, A. Gorecki, and W. Kolodziejcki, Kinetics of 1H-31P cross-polarisation in human trabecular bone, *Solid State Nuclear Magnetic Resonance* 10 (1998) 191-195.
- [38] G. Cho, Y. Wu, and J. Ackerman, Detection of Hydroxyl Ions in Bone Mineral by Solid-State NMR Spectroscopy, *Science* 300 (2003) 1123-1127.
- [39] Y. Wu, J. Ackerman, H. Kim, C. Rey, A. Barroug, and M. Glimcher, Nuclear Magnetic Resonance Spin-Spin Relaxation of the Crystals of Bone, Dental Enamel, and Synthetic Hydroxyapatites, *Journal of Bone and Mineral Research* 17 (2002) 472-480.
- [40] Y. Wu, J.L. Ackerman, E.S. Strawich, C. Rey, H.-M. Kim, and M.J. Glimcher, Phosphate Ions in Bone: Identification of a Calcium–Organic Phosphate Complex by 31P Solid-State NMR Spectroscopy at Early Stages of Mineralization, *Calcified Tissue International* 72 (2003) 610-626.

- 
- [41] P.A. Raj, M. Johnsson, M.J. Levine, and G.H. Nancollas, *J. Biol. Chem.* 267 (1992) 5968-5976.
- [42] J.R. Long, J.L. Dindot, H. Zebrosky, S. Kiihne, R.H. Clark, A.A. Campbell, P.S. Stayton, and G.P. Drobny, A peptide that inhibits hydroxyapatite growth is in an extended conformation on the crystal surface, *Proc. Natl. Acad. Sci. USA* 95 (1998) 12083-12087.
- [43] W.J. Shaw, J.R. Long, A.A. Campbell, P.S. Stayton, and G.P. Drobny, A Solid State NMR Study of Dynamics in a Hydrated Salivary Peptide Adsorbed to Hydroxyapatite, *J. Am. Chem. Soc.* 122 (2000) 7118-7119.
- [44] J.R. Long, W.J. Shaw, P.S. Stayton, and G.P. Drobny, Structure and Dynamics of Hydrated Statherin on Hydroxyapatite As Determined by Solid-State NMR, *Biochemistry* 40 (2001) 15451-15455.
- [45] W.J. Shaw, A.A. Campbell, M.L. Paine, and M.L. Snead, The COOH Terminus of the Amelogenin, LRAP, Is Oriented Next to the Hydroxyapatite Surface, *The Journal of Biological Chemistry* 279 (2004) 40263-40266.
- [46] A.E. Aliev, Backbone dynamics in collagen, *Chemical Physics Letters* 398 (2004) 522-525.
- [47] D. Huster, J. Schiller, and K. Arnold, Comparison of Collagen Dynamics in Articular Cartilage and Isolated Fibrils by Solid-State NMR Spectroscopy, *Magnetic Resonance in Medicine* 48 (2002) 624-632.
- [48] D. Reichert, O. Pascui, E.R. deAzevedo, T.J. Bonagamba, K. Arnold, and D. Huster, A solid-state NMR study of the fast and slow dynamics of collagen fibrils at varying hydration levels, *Magnetic Resonance in Chemistry* 42 (2004) 276-284.
- [49] C. Rey, J. Lian, M. Grynblas, F. Shapiro, L. Zylberberg, and M.J. Glimcher, Non-apatitic environments in bone mineral: FT-IR detection, biological properties and changes in several disease states., *Connect. Tissue Res.* 21 (1989) 267-273.
- [50] Z.H. Cheng, A. Yasukawa, K. Kandori, and T. Ishikawa, FTIR Study on incorporation of CO<sub>2</sub> into calcium hydroxyapatite, *J. Chem. Soc., Faraday Trans. 2* 94 (1998) 1501-1505.
- [51] Y. Ling, H.F. Rios, E.R. Myers, Y. Lu, J.Q. Feng, and A.L. Boskey, DMP1 Depletion Decreases Bone Mineralization In Vivo: An FTIR Imaging Analysis, *JOURNAL OF BONE AND MINERAL RESEARCH* 20 (2005) 2169-2177.
- [52] A. Hirschman, A.E. Sobel, B. Kramer, and I. Fankuchen, An X-Ray Diffraction study of high phosphate bones, *The Journal of Biological Chemistry* 171 (1947) 285-294.

- [53] B. Kawamura, J. Watanabe, and M. Hirayama, A study of bone disorders with x-ray diffraction (preliminary report). *Nippon Seikeigeka Gakkai Zasshi.* 39 (1966) 1147-1152.
- [54] P.D. Frazier, I. Zipkin, and L.F. Mills, X-ray diffraction study of human bone. Direct methods of estimating changes in line broadening., *Arch Oral Biol.* 12 (1967) 73-78.
- [55] E. D. Eanes, D.R. Lundy, and G.N. Martin, X-ray Diffraction Study of the Mineralization of Turkey Leg Tendon, *Calc. Tiss. Res.* 6 (1970) 239-248.
- [56] M.C. Dalconi, C. Meneghini, S. Nuzzo, R. Wenk, and S. Mobilio, Structure of bioapatite in human foetal bones: An X-ray diffraction study, *Nuclear Instruments and Methods in Physics Research B* 200 (2003) 406-410.
- [57] S.N. Danilchenko, A.V. Koropov, I.Y. Protsenko, B. Sulkiö-Cleff, and L.F. Sukhodub, Thermal behavior of biogenic apatite crystals in bone: An X-ray diffraction study, *Cryst. Res. Technol.* 41 (2006).
- [58] F. Peters, K. Schwarz, and M. Epple, The structure of bone studied with synchrotron X-ray diffraction, X-ray absorption spectroscopy and thermal analysis, *Thermochimica Acta* 361 (2000) 131-138.
- [59] M.H. Levitt, *Spin Dynamics: Basics of Nuclear Magnetic Resonance*, John Wiley & Sons, Ltd, Southampton, UK, 2001.
- [60] M.J. Duer, *Introduction to Solid-State NMR Spectroscopy*, Blyckwell Publishing, Ltd, Cambridge, 2004.
- [61] W. Kolodziejewski, and J. Klinowski, Kinetics of Cross-Polarization in Solid-State NMR: A Guide for Chemists, *Chemical Review* 102 (2002) 613-628.
- [62] M. Lee, and W.I. Goldberg, Nuclear-Magnetic-Resonance Line Narrowing by a Rotating rf Field, *Phys. Rev.* 140 (1965) A1261.
- [63] K.T. Mueller, T.P. Jarvie, D.J. Aurentz, and B.W. Roberts, The REDOR Transform: Direct Calculation of Internuclear Couplings from Dipolar-Dephasing NMR Data, *Chemical Physics Letters* 242 (1995) 535-542.
- [64] K.T. Mueller, Analytic solutions for the time evolution of dipolar-dephasing NMR signals, *Journal of magnetic resonance Series A* 113 (1995) 13.
- [65] R.R. Ernst, *Principles of Nuclear Magnetic Resonance in One and Two Dimensions*, The Universities Press, Belfast, 1986.
- [66] M. Ernst, *Heteronuclear Spin Decoupling in Solid-State NMR Under Magic-Angle Sample Spinning*, Departement Chemie, Eidgenössischen Technischen Hochschule Zürich, Zürich, pp. 100.
- [67] A.E. Bennett, C.M. Rienstra, M. Auger, K.V. Lakshmi, and R.G. Griffin, Heteronuclear decoupling in rotating solids, *J. Chem. Phys.* 103 (1995) 6951-6958.

- 
- [68] K. Saalwächter, R. Graf, and H.W. Spiess, Recoupled Polarization-Transfer Methods for Solid-State  $1\text{H}$ – $^{13}\text{C}$  Heteronuclear Correlation in the Limit of Fast MAS, *J. Magn. Res.* 148 (2001) 398-418.
- [69] K. Schmidt-Rohr, and H.W. Spiess, *Multidimensional Solid-State NMR and Polymers*, Academic Press, Bodmin, 1994.
- [70] L. Emsley, P. Borgnat, A. Lesage, and S. Caldarelli, Improved Sensitivity in Selective NMR Correlation Spectroscopy and Applications to the Determination of Scalar Couplings in Peptides and Proteins, *J. Am. Chem. Soc.* 118 (1996) 9320-9325.
- [71] A. Lesage, and L. Emsley, Through-Bond Heteronuclear Single-Quantum Correlation Spectroscopy in Solid-State NMR, and Comparison to Other Through-Bond and Through-Space Experiments, *J. Magn. Res.* 148 (2001) 449-454.
- [72] D. Massiot, and M. Deschamps, Three-dimensional Through-Bond Homonuclear-Heteronuclear Correlation Experiments for Quadrupolar Nuclei in Solid-State NMR applied to  $^{27}\text{Al}$ -O- $^{31}\text{P}$ -O- $^{27}\text{Al}$  networks, *J. Magn. Res.* 184 (2006) 13-19.
- [73] M. Deschamps, F. Fayon, V. Montouillout, and D. Massiot, Through-bond homonuclear correlation experiments in Solid-state NMR applied to quadrupolar nuclei in Al-O-P-O-Al chains., *Chem. Comm.* (2006) 1924-1925.
- [74] C. Jäger, T. Welzel, W. Meyer-Zaika, and M. Eppe, A solid-state NMR investigation of the structure of nanocrystalline hydroxyapatite, *Magn. Res. Chem.* 44 (2006) 573-580.
- [75] E.E. Wilson, A. Awonusi, M.D. Morris, D.H. Kohn, M.M.J. Tecklenburg, and L.W. Beck, Three Structural Roles for Water in Bone Observed by Solid-State NMR, *Biophys. J.* 90 (2006) 3722-3731.
- [76] V. Ladizhanskaya, E. Vinogradov, B.-J.v. Rossum, H.J.M.d. Groot, and S. Vegac, Multiple-spin effects in fast magic angle spinning Lee–Goldburg cross-polarization experiments in uniformly labeled compounds, *J. Chem. Phys.* 118 (2003) 5547-5557.
- [77] D. Tadic, A. Veresov, V.I. Putlayev, and M. Eppe, *In-vitro* preparation of nanocrystalline calcium phosphates as bone substitution materials in surgery, *Mat.-wiss. u. Werkstofftech.* 34 (2003) 1048-1051.
- [78] A.E. Bennett, C.M. Rienstra, M. Auger, K.V. Lakshmi, and R.G. Griffin, Heteronuclear decoupling in rotating solids, *J. Chem. Phys.* 103 (1995) 6951-6958.
- [79] E. Vinogradov, P.K. Madhu, and S. Vega, High-resolution proton solid-state NMR spectroscopy by phase-modulated Lee–Goldburg experiment, *Chem. Phys. Lett.* 314 (1999) 443-450.

- [80] E. Vinogradov, P.K. Madhu, and S. Vega, Proton spectroscopy in solid state nuclear magnetic resonance with windowed phase modulated Lee–Goldburg decoupling sequences, *Chem. Phys. Let.* 354 (2002) 193-202.
- [81] A. Veis, Mineralization in organic matrix frameworks, *Rev. Mineral. Geochem.*, Mineralogical Society of America, Washington, DC, USA, 2003, pp. 249-289.
- [82] J.E. Roberts, L.C. Bonar, R.G. Griffin, and M.J. Glimcher, Characterization of very young mineral phases of bone by solid state <sup>31</sup>Phosphorus magic angle sample spinning nuclear magnetic resonance and X-ray diffraction, *Calcif. Tissue Int.* 50 (1992) 42-48.
- [83] R.A. Santos, R.A. Wind, and C.E. Bronnimann, <sup>1</sup>H CRAMPS and <sup>1</sup>H-<sup>31</sup>P HetCor Experiments on Bone, Bone Mineral, and Model Calcium Phosphate Phases, *J. Magn. Res.* 106 B (1994) 183-187.
- [84] Y. Wu, J. L. Ackerman, H.-M. Kim, C. Rey, A. Barroug, and M.J. Glimcher, Nuclear Magnetic Resonance Spin-Spin Relaxation of the Crystals of Bone, Dental Enamel, and Synthetic Hydroxyapatites, *J. Bone Miner. Res.* 17 (2002) 472-480.
- [85] G.P. Drobny, J.R. Long, T. Karlsson, W. Shaw, J. Popham, N. Oyler, P. Bower, J. Stringer, D. Gregory, M. Mehta, and P.S. Stayton, Structural Studies of Biomaterials Using Double-Quantum Solid-State NMR Spectroscopy, *Annu. Rev. Phys. Chem.* 54 (2003) 531-571.
- [86] G. Goobes, P.S. Stayton, and G.P. Drobny, Solid State NMR Studies of molecular recognition at Protein-Mineral Interface, *Prog. Nuc. Magn. Spectr.* 50 (2007) 71-85.
- [87] W.J. Shaw, J.R. Long, J.L. Dindot, A.A. Campbell, P.S. Stayton, and G.P. Drobny, Determination of Statherin N-Terminal Peptide Conformation on Hydroxyapatite Crystals, *J. Am. Chem. Soc.* 122 (2000) 1709-1716.
- [88] C. Jäger, N.S. Groom, E.A. Bowe, A. Horner, M.E. Davies, R.C. Murray, and M.J. Duer, Investigation of the Nature of the Protein-Mineral Interface in Bone by Solid-State NMR, *Chem. Mat.* 17 (2005) 3059-3061.
- [89] E.R. Wise, S. Maltsev, M.E. Davies, M.J. Duer, C. Jäger, N. Loveridge, R.C. Murray, and D.G. Reid, The mineral-organic interface in bone is lined by polysaccharide, *Science* submitted (2007).
- [90] D. Tadic, A. Veresov, V.I. Putlayev, and M. Eppe, *In-vitro* preparation of nanocrystalline calcium phosphates as bone substitution materials in surgery, *Materialwissenschaft und Werkstofftechnik* 34 (2003) 1048-1051.
- [91] D. Tadic, F. Peters, and M. Eppe, Continuous synthesis of amorphous carbonated apatites, *Biomaterials* 23 (2002) 2553-2559.
- [92] C. Jaeger, S. Maltsev, and A. Karrasch, Progress of Structural Elucidation of Amorphous Calcium Phosphate (ACP) and Hydroxyapatite (HAp): Disorder

---

and Surfaces as Seen by Solid State NMR, *Key Engineering Materials* 309-311 (2006) 69-72.

- [93] M.A. Wilson, *NMR Techniques and Applications in Geochemistry and Soil Chemistry*, Pergamon Press, London, 1987.
- [94] S. Maltsev, M.J. Duer, R.C. Murray, and C. Jäger, A solid-state NMR comparison of the mineral structure in bone from diseased joints in the horse, *Journal of Material Science* in press (2007).
- [95] N.C. Blumenthal, F. Betts, and A.S. Posner, Effect of carbonate and biological macromolecules on formation and properties of hydroxyapatite, *Calcified Tissue Research* 18 (1975) 81-90.
- [96] M.D. Grynpas, L.C. Bonar, and M.J. Glimcher, Failure to detect an amorphous calcium-phosphate solid phase in bone mineral: a radial distribution function study, *Calcified Tissue International* 36 (1984) 291-301.
- [97] M. Grynpas, Age and disease-related changes in the mineral of bone, *Calcified Tissue International* 53 (1993) S57-S64.
- [98] H.A. Lowenstam, and S. Weiner, *On Biomineralization*, Oxford University Press New York, Oxford, 1989.
- [99] E.P. Paschalis, E. DiCarlo, F. Betts, P. Sherman, R. Mendelsohn, and A.L. Boskey, FTIR microspectroscopic analysis of human osteonal bone, *Calcified Tissue International* 59 (1996) 480-487.
- [100] E.E. Wilson, A. Awomusi, M.D. Morris, D.H. Kohn, M.M.J. Tecklenburg, and L.W. Beck, *Biophys J* 90 (2006) 3722.
- [101] G. Cho, Y. Wu, and J.L. Ackermann, *Science* 300 (2003) 613.
- [102] C. Jäger, T. Welzel, W. Meyer-Zaika, and M. Epple, *Magn Reson Chem Chem* 44 (2006) 573.
- [103] H. Saito, and M. Yokoi, A C-13 Nmr-Study on Collagens in the Solid-State - Hydration Dehydration-Induced Conformational Change of Collagen and Detection of Internal Motions, *Journal of Biochemistry* 111 (1992) 376-382.
- [104] D. Huster, J. Schiller, and K. Arnold, Comparison of collagen dynamics in articular cartilage and isolated fibrils by solid-state NMR spectroscopy, *Magn Reson Med* 48 (2002) 624-32.
- [105] C. Jaeger, N.S. Groom, E.A. Bowe, A. Horner, M.E. Davies, R.C. Murray, and M.J. Duer, Investigation of the nature of the protein-mineral interface in bone by solid-state NMR, *Chemistry of Materials* 17 (2005) 3059-3061.
- [106] A. Mucci, L. Schenetti, and N. Volpi, H-1 and C-13 nuclear magnetic resonance identification and characterization of components of chondroitin sulfates of various origin, *Carbohydrate Polymers* 41 (2000) 37-45.

- [107] S. Mann, *Biomaterialization: Principles and Concepts in Bioinorganic Materials Chemistry* Oxford University Press, Oxford, 2001.
- [108] A. Veis, *Mineralization in Organic Matrix Frameworks*. in: J.J.D.Y. Patricia M Dove, Steve Weiner, (Ed.), *Biomaterialization*, The Mineralogical Society of America, Washington DC, 2003, pp. 249-289.
- [109] G.K. Hunter, C.L. Kyle, and H.A. Goldberg, Modulation of crystal formation by bone phosphoproteins: structural specificity of the osteopontin-mediated inhibition of hydroxyapatite formation, *Biochem J* 300 ( Pt 3) (1994) 723-8.
- [110] Q.Q. Hoang, F. Sicheri, A.J. Howard, and D.S. Yang, Bone recognition mechanism of porcine osteocalcin from crystal structure, *Nature* 425 (2003) 977-80.
- [111] T.L. Dowd, J.F. Rosen, L. Li, and C.M. Gundberg, The three-dimensional structure of bovine calcium ion-bound osteocalcin using <sup>1</sup>H NMR spectroscopy, *Biochemistry* 42 (2003) 7769-79.
- [112] T.S. Xu, P. Bianco, L.W. Fisher, G. Longenecker, E. Smith, S. Goldstein, J. Bonadio, A. Boskey, A.M. Heegaard, B. Sommer, K. Satomura, P. Dominguez, C.Y. Zhao, A.B. Kulkarni, P.G. Robey, and M.F. Young, Targeted disruption of the biglycan gene leads to an osteoporosis-like phenotype in mice, *Nature Genetics* 20 (1998) 78-82.
- [113] A.L. Boskey, D. Stiner, I. Binderman, and S.B. Doty, Effects of proteoglycan modification on mineral formation in a differentiating chick limb-bud mesenchymal cell culture system, *Journal of Cellular Biochemistry* 64 (1997) 632-643.
- [114] A.L. Boskey, M. Maresca, B. Wikstrom, and A. Hjerpe, Hydroxyapatite formation in the presence of proteoglycans of reduced sulfate content: studies in the brachymorphic mouse, *Calcif Tissue Int* 49 (1991) 389-93.
- [115] A.L. Boskey, L. Spevak, S.B. Doty, and L. Rosenberg, Effects of bone CS-proteoglycans, DS-decorin, and DS-biglycan on hydroxyapatite formation in a gelatin gel, *Calcified Tissue International* 61 (1997) 298-305.
- [116] S.G. Rees, D.T. Wassell, R.P. Shellis, and G. Embery, Effect of serum albumin on glycosaminoglycan inhibition of hydroxyapatite formation, *Biomaterials* 25 (2004) 971-7.
- [117] M. Takagi, M. Maeno, T. Yamada, K. Miyashita, and K. Otsuka, Nature and distribution of chondroitin sulphate and dermatan sulphate proteoglycans in rabbit alveolar bone, *Histochemical Journal* 28 (1996) 341-351.
- [118] J.E. Scott, Proteoglycan-fibrillar collagen interactions, *Biochem J* 252 (1988) 313-23.
- [119] P.A. McEwan, P.G. Scott, P.N. Bishop, and J. Bella, Structural correlations in the family of small leucine-rich repeat proteins and proteoglycans, *Journal of Structural Biology* 155 (2006) 294-305.



- 
- [120] P.G. Scott, C.M. Dodd, E.M. Bergmann, J.K. Sheehan, and P.N. Bishop, Crystal structure of the biglycan dimer and evidence that dimerization is essential for folding and stability of class I small leucine-rich repeat proteoglycans, *Journal of Biological Chemistry* 281 (2006) 13324-13332.
- [121] A.L. Boskey, M. Maresca, A.L. Armstrong, and M.G. Ehrlich, Treatment of Proteoglycan Aggregates with Physeal Enzymes Reduces Their Ability to Inhibit Hydroxyapatite Proliferation in a Gelatin Gel, *Journal of Orthopaedic Research* 10 (1992) 313-319.
- [122] N.J. Crane, V. Popescu, M.D. Morris, P. Steenhuis, and M.A. Ignelzi, Raman spectroscopic evidence for octacalcium phosphate and other transient mineral species deposited during intramembranous mineralization, *Bone* 39 (2006) 434-442.
- [123] S. Weiner, Transient precursor strategy in mineral formation of bone, *Bone* 39 (2006) 431-433.
- [124] G. Gafni, D. Septier, and M. Goldberg, Effect of chondroitin sulfate and biglycan on the crystallization of hydroxyapatite under physiological conditions, *Journal of Crystal Growth* 205 (1999) 618-623.
- [125] O. Akkus, F. Adar, and M.B. Schaffler, Age-related changes in physicochemical properties of mineral crystals are related to impaired mechanical function of cortical bone, *Bone* 34 (2004) 443-453.
- [126] A.L. Boskey, E. DiCarlo, E. Paschalis, P. West, and R. Mendelsohn, Comparison of mineral quality and quantity in iliac crest biopsies from high- and low-turnover osteoporosis: an FT-IR microspectroscopic investigation, *Osteoporosis International* 16 (2005) 2031-2038.
- [127] J.E. Scott, F. Heatley, and B. Wood, Comparison of secondary structures in water of chondroitin-4-sulfate and dermatan sulfate: implications in the formation of tertiary structures, *Biochemistry* 34 (1995) 15467-74.
- [128] W.T. Winter, S. Arnott, D.H. Isaac, and E.D.T. Atkins, Chondroitin 4-Sulfate - Structure of a Sulfated Glycosaminoglycan, *Journal of Molecular Biology* 125 (1978) 1-19.